3-23-2017

Computational Optimization Under Uncertainty of an Active Flow Control Jet

Luke A. Welch

RELATING FILM COOLING PERFORMANCE BETWEEN AMBIENT AND NEAR ENGINE TEMPERATURES

THESIS

Christopher J. Vorgert, Second Lieutenant, USAF

AFIT-ENY-MS-17-M-298

DEPARTMENT OF THE AIR FORCE
AIR UNIVERSITY

AIR FORCE INSTITUTE OF TECHNOLOGY

Wright-Patterson Air Force Base, Ohio

AFIT-ENY-MS-17-M-298

RELATING FILM COOLING PERFORMANCE BETWEEN AMBIENT AND NEAR ENGINE TEMPERATURES

THESIS

Presented to the Faculty

Department of Aeronautics and Astronautics

Graduate School of Engineering and Management

Air Force Institute of Technology

Air University

Air Education and Training Command

in Partial Fulfillment of the Requirements for the

Degree of Master of Science in Aeronautical Engineering

Christopher J. Vorgert, BS
Second Lieutenant, USAF

March 2017

AFIT-ENY-MS-17-M-298

RELATING FILM COOLING PERFORMANCE BETWEEN AMBIENT AND NEAR ENGINE TEMPERATURES

Christopher J. Vorgert, BS

Second Lieutenant, USAF

Approved:

_____	_____
Marc D. Polanka, PhD (Chairman)	Date
_____	_____
Major James L. Rutledge, PhD (Member)	Date
_____	_____
Captain Adam L. Comer, PhD (Member)	Date

Abstract

This thesis explores multiple topics, including the relative importance of nondimensional parameters that relate film cooling performance within different temperature regimes and the effects of internal coolant flow and coolant temperature on overall film cooling effectiveness. The majority of film cooling research has been conducted at near ambient temperatures, under the assumption that the results scale to near engine temperatures. However, direct scaling is not possible due to the variation of properties with change in temperature. To investigate this topic, tests were performed at both near ambient and near engine temperatures. A Hastelloy model representative of a turbine blade was utilized for IR tests. The model consisted of a quarter cylinder leading edge, which transitions into a flat body before the slanted after-body. Near engine temperatures were produced via premixed propane and air combustion in a Well-Stirred Reactor (WSR) with air supplied as the film coolant gas. Near ambient conditions used heated air for freestream flow and carbon dioxide, argon, or air as film coolant gases to reach the desired density ratios and advective capacity ratios. These tests confirmed many known phenomena, such as the occurrence of separation at high momentum ratios. It was found that even with matched blowing ratio, density ratio, and freestream Reynolds number, the high temperature cases achieved higher overall effectiveness values. The results suggest that the temperature difference between the coolant and freestream is also an important parameter, as is the internal mass flow. Test results showed that cooling effectiveness increased with hotter coolant, which is counterintuitive. Numerous improvements to the rig were also implemented and investigated, leading to increased control of the coolant temperature and potential avenues for improving the accuracy of IR thermography measurements on the FCR.

Acknowledgements

First, I would like to thank Christian Schmiedel for his incredible assistance and comradery throughout this adventure. Thank you to Dr. Polanka for all of his patience and guidance. This would not have been possible without him and my other committee members, Major Rutledge and Captain Comer, providing invaluable instruction and encouragement both in and out of class. Thanks especially to the AFIT Model Shop team for all their hard work on the new FCR parts and repairs. Thank you also to Lieutenant Bryant and Lieutenant Wiese for collaborating to compare the FCR and LEFCT. Thanks to Steve Palluconi over at ISSI for lending me his PSP expertise. Thank you to Lieutenant Ashby for answering my deluge of questions and laying the groundwork for me. Thanks to Mike Ranft for his help with the laser spectrometry tests. Thank you, of course, to my parents for all their emotional support. Finally, thank you to my friends in the COAL Lab for all their help (and for putting up with my incessant whistling).

Nomenclature

A	=	area, constant
a	=	constant
ACR	=	advective capacity ratio
B	=	constant
b	=	constant
Bi	=	Biot number
C	=	concentration, chord fraction, constant
c_p	=	specific heat at constant pressure
D	=	leading edge diameter, mass diffusion coefficient
d	=	cooling hole diameter
D_h	=	hydraulic diameter
DR	=	density ratio
e	=	constant
H	=	freestream channel height
h	=	heat transfer coefficient
I	=	momentum flux ratio
$\mathcal{I}$	=	intensity
k	=	thermal conductivity
L	=	cooling hole length
Le	=	Lewis number
M	=	blowing ratio
m	=	constant
$\dot{m}$	=	mass flow rate
Ma	=	Mach number
MW	=	molecular weight
N	=	number
n	=	number density, constant
Nu	=	Nusselt number
P	=	pressure, pitch
Pr	=	Prandtl number
q''	=	heat flux
R	=	universal gas constant
r_c	=	recovery factor
Re	=	Reynolds number
S	=	trench depth, system response
Sc	=	Schmidt number
T	=	temperature
t	=	thickness
Tu	=	turbulence intensity

U	=	velocity
VR	=	velocity ratio
W	=	trench width, freestream channel width
X	=	variable
x	=	length scale, axial position
y	=	lateral position
Z	=	parameter

Subscripts

0	=	without film cooling, reference
air	=	with air injection
app	=	apparent
aw	=	adiabatic wall
b	=	background, backside
c	=	coolant
$calc$	=	calculated
$cond$	=	conduction
$conv$	=	convection
CP	=	constant properties
e	=	cooling hole exit
$engine$	=	engine condition
exp	=	experimental
f	=	with film cooling
fg	=	foreign gas
$film$	=	film
g	=	gas
$holes$	=	film cooling holes
i	=	cooling hole inlet, into surface, initial condition, internal
in	=	coolant fed into the test block
max	=	maximum
mix	=	with foreign gas injection
$model$	=	model condition
o	=	out of surface
O_2	=	oxygen
p	=	predicted
R	=	reference
rad	=	radiation
ref	=	reference
rms	=	root mean square
S	=	signal
s	=	surface
T	=	cooling hole throat
w	=	wall
x	=	axial position
∞	=	freestream

Superscripts

$*$	=	nondimensional variable
$\overline{(\ldots)}$	=	lateral or span average
$\overline{\overline{(\ldots)}}$	=	area average

Greek Letters

α	=	thermal diffusivity, absorptivity, coolant injection angle
β	=	cooling hole fan shape flare half angle
γ	=	ratio of specific heats, cooling hole arc position
Δ	=	change
δ	=	layback angle, uncertainty
ε	=	emissivity
η	=	adiabatic effectiveness
μ	=	dynamic viscosity
ν	=	kinematic viscosity
ρ	=	density, reflectivity
ϕ	=	overall effectiveness
χ	=	coolant warming factor

Abbreviations

AFIT	=	Air Force Institute of Technology
AFRL	=	Air Force Research Laboratory
CFD	=	Computational Fluid Dynamics
COAL	=	Combustion Optimization and Analysis Laser
CRVP	=	Counter Rotating Vortex Pair
FCR	=	Film Cooling Rig
GPM	=	Gallons per Minute
HAL	=	Heat-Transfer and Aerothermal Laboratory
IR	=	Infrared
ISSI	=	Innovative Scientific Solutions, Inc.
LEFCT	=	Leading Edge Film Cooling Tunnel
PIV	=	Particle Imaging Velocimetry
PSP	=	Pressure Sensitive Paint
SLPM	=	Standard Liters per Minute
TC	=	Thermocouple
TBC	=	Thermal Barrier Coating
TLC	=	Thermochromic Liquid Crystal
WPAFB	=	Wright Patterson Air Force Base
WSR	=	Well-Stirred Reactor

Table of Contents

Abstract ..... **v**
Acknowledgements ..... **vi**
Nomenclature ..... **vii**
Table of Contents ..... **x**
List of Figures ..... **xii**
List of Tables ..... **xvii**
1. Introduction **1**
1.1. Film Cooling Motivation 1
1.2. Overall Objectives 2
1.3. Additional Accomplishments 3
1.3.1. New Coolant Inlet Design 3
1.3.2. New Boundary Layer Bleed Design 3
1.3.3. Investigation of Window Effects 4
1.3.4. Modification to Ignition Procedures 5
2. Literature Review **6**
2.1. Film Cooling Basics 7
2.1.1. Performance Metrics 10
2.1.2. Characteristic Parameters 11
2.1.3. Additional Performance Metrics 17
2.2. Cooling Geometry Effects 19
2.2.1. Coolant Hole Spacing Effects 20
2.2.2. Coolant Injection Angle Effects 22
2.2.3. Coolant Hole Shape Effects 23
2.2.3.1. Shaped Holes 24
2.2.3.2. Trenched Holes 26
2.3. Flow Characteristic Effects 29
2.3.1. Mach Effects 30
2.3.2. Freestream Turbulence Effects 31
2.3.3. Internal Flow Effects 31
2.4. Conjugate Heat Transfer Effects 33
2.5. Experimental Techniques 36
2.5.1. Thermal Measurement Methods 36
2.5.2. Heat-Mass Transfer Analogy 41
2.5.3. Mass Transfer Measurement Methods 43
2.5.4. Comparison of IR and PSP Measurement Methods 49
3. Experimental Methods **52**
3.1. Film Cooling Rig 53

3.1.1. Well-Stirred Reactor 54
3.1.2. Test Section 61
3.1.3. Cooling Block Assembly 69
3.1.3.1. Test Block Assembly 70
3.1.3.2. Boundary Layer Bleed 77
3.1.3.3. Test Plates 81
3.2. Additional Equipment 87
3.2.1. COAL Lab Equipment 87
3.2.2. PSP Equipment 89
3.2.3. IR Camera 90
3.3. Test Setup and Data Reduction 95
3.3.1. Shared Data Acquisition Systems 96
3.3.1.1. Key Temperatures and Flow Rates 96
3.3.1.2. Characteristic Parameters and Performance Metrics 98
3.3.2. PSP Setup 100
3.3.3. IR Thermography Setup 102
3.4. Experimental Uncertainty 103
3.4.1. Measurement Uncertainty 104
3.4.2. Repeatability Measurements at Low Temperature 106

4. Results and Discussion 110

4.1. PSP and Thermal Investigation of the Test Plate Leading Edge 110
4.1.1. Facility Impact 110
4.1.2. PSP Results 112
4.1.3. Leading Edge Thermal Phenomena 116
4.2. Near Ambient and Near Engine Thermal Matching Tests 119
4.2.1. Low Temperature 119
4.2.2. High Temperature 126
4.2.3. Temperature Regime Comparison 129
4.3. Near Ambient Coolant Temperature Impact Investigation 131
4.3.1. Increased T_c Test Data 132
4.3.2. Comparison between Sets 134

5. Conclusions 138

5.1. Leading Edge Phenomena and LEFCT Comparisons 138
5.2. Matching Low and High Temperature Tests 139
5.3. Coolant Mass Flow and Temperature Impact 140
5.4. FCR Modifications and Future Improvements 141

References 145

List of Figures

FIGURE Page

Figure 2-1: Sample turbine airfoil cooling scheme diagram (image from Han et al. [4]]).....7

Figure 2-2: Turbine airfoil fluid flow diagram (from Bogard and Thole [3]) 8

Figure 2-3: Dynamics of a coolant jet (from Fric and Roshko [5]) 9

Figure 2-4: Schematic of cylindrical cooling hole geometry: (a) side view and (b) top view (image from Ashby [11]) 20

Figure 2-5: Schematic of cooling hole compound angle 23

Figure 2-6: Continuous 2D slot cooling scheme (image from Bunker [24]).....24

Figure 2-7: Common geometries for holes with shaped exits: (a) fan-shaped hole, (b) laidback hole (images from Bunker [14]) 25

Figure 2-8: Shallow surface recess flow interaction diagram (image from Bunker [28]).....27

Figure 2-9: Cratered hole test geometry, side view (top) and cutaway view through plane 10 (bottom) (images from Fric and Campbell [29]) 28

Figure 2-10: Cratered hole vs. normal holes (from Fric and Campbell [29]).....29

Figure 2-11: Dees et al. [33] test plate cutaway view.....33

Figure 2-12: Data from Williams et al. [8] 34

Figure 2-13: Contours of η for (a) I = 0.35 (b) I = 0.58 and (c) I = 1.03 and contours of ϕ for (d) I = 0.38, (e) I = 0.62 and (f) I = 1.09, dashed line denotes internal rib location (from Williams et al. [8]) 35

Figure 2-14: Comparison of single component and binary PSP (image from Wiese [18]).....46

Figure 3-1: AFIT Film Cooling Rig and Well-Stirred Reactor cross-section (image adapted from Ashby [2]).....53

Figure 3-2: AFIT Well-Stirred Reactor diagrams: (a) side view cross-section and (b) exploded view (images from Lynch [19]).....54

Figure 3-3: Inverted view of WSR transition section (figure from Ashby [2]).....56

Figure 3-4: Dislodged ceramic (left) and Ceramabond repair (right).....57

Figure 3-5: AFIT Well-Stirred Reactor: (a) lower toroid and jet ring and (b) upper toroid (figure from Ashby [2]).....58

Figure 3-6: a) TBC damage on upper toroid half b) New WSR coolant water filter 59

Figure 3-7: Location of repaired water coolant channel welds (top) Discoloration from cooling water leak (Bottom).....60

Figure 3-8: a) Heater tape and b) melted insulation 61

Figure 3-9: FCR side view (from Ashby [2]).....63

Figure 3-10: Test section cutaway view 64

Figure 3-11: Calibration curves and sample IR pictures at equivalent freestream conditions with (a, b) no window, (c, d) sapphire window, (e, f) silicon window, (g, h) tilted sapphire window..66

Figure 3-12: Sapphire window with residue (left) and sapphire window post-cleaning (right)....67

Figure 3-13: Window transmittance vs. wavelength 68

Figure 3-14: Cooling block assembly (figure from Ashby [2]).....69

Figure 3-15: Test block exploded view 71

Figure 3-16: New coolant feed prototype in position for flow distribution testing 72

Figure 3-17: Comparison of old (top) and new (middle) coolant design flow temperature distributions and the new design with the baffle plate (bottom).....73

Figure 3-18: Cooling block assembly cross-section with flow paths 74

Figure 3-19: Bucket heat exchanger for coolant exhaust.....75

Figure 3-20: a) Top view of the new boundary bleed with diagnostic thermocouples, b) Side view of the boundary layer bleed set in position with the coolant block 80

Figure 3-21: Comparison of old and new boundary layer bleed designs at 1300K freestream temperature (figure by Christian Schmiedel).....81

Figure 3-22: Side views of representative turbine airfoil leading edge test plate (from Ashby [2]) 82

Figure 3-23: FCR one-row showerhead model schematics: (a) side view and (b) coolant hole top view (from Ashby [2]) 83

Figure 3-24: Schematics of (a) shaped hole and (b) shaped hole cooling scheme (from Ashby [2]) 84

Figure 3-25: Underside of the first test plate 85

Figure 3-26: Thermocouple instrumentation scheme (modified from Ashby [2]) 86

Figure 3-27: Cross-section of thermocouple locations (modified from Ashby [2]) 86

Figure 3-28: PSP Spatial Calibration Pictures a) with grid intersections marked b) no grid with film cooling hole locations and end of leading edge marked 90

Figure 3-29: Representative IR calibration curves at low temperature (top and middle) and high temperature (bottom) 93

Figure 3-30: IR calibration intensity measurement region (from Ashby [2]).....95

Figure 3-31: PSP test setup 101

Figure 3-32: IR camera in sliding mount 103

Figure 3-33: Low temperature repeatability data.....108

Figure 3-34: Comparison of repeatability calibration curves 109

Figure 4-1: Two-dimensional CFD analysis of freestream velocity over the test plate surface for a) LEFCT area ratio b) FCR area ratio 111

Figure 4-2: LEFCT adiabatic effectiveness distributions at LEFCT points a) 1, b) 3, and c) 5 (provided by Connor Wiese).....113

Figure 4-3: Pressure profiles for a) Point 1 (Argon, I = 3), b) Point 4 (CO_2, I = 8.74), c) Point 10 (N_2, I = 2.86), d) Point 8 (CO_2, I = 54.9) 115

Figure 4-4: LEFCT overall effectiveness distributions at Point a) 1, b) 3, c) 5 (provided by Carol Bryant) 117

Figure 4-5: Leading edge test plate at ambient freestream a) T_c = 370K, M = 1, ER = 1 b) T_c = 370K, M = 1, ER = 4 118

Figure 4-6: Overall effectiveness distributions for set 1 Points a) 11 and b) 18 121

Figure 4-7: Comparison of centerline and span-averaged values 121

Figure 4-8: Low temperature points in set 1 for a) air, b) argon, c) CO_2 123

Figure 4-9: Low temperature set 1 points at total coolant mass flow a) 7.3 x 10^{-3} kg/min, b) 3.6 x 10^{-3} kg/min c) 1.8 x 10^{-3} kg/min 125

Figure 4-10: High temperature IR images at a) Point 1, b) Point 9 127

Figure 4-11: High temperature points at a) 1.66 x 10^{-2} and 8.30 x 10^{-3} kg/min, b) 4.15 x 10^{-3} and 2.08 x $^{10-3}$ kg/min 128

Figure 4-12: ϕ distributions at M = 2, ER = 3, DR = 1.7, with matched freestream Re = 4120 a) CO2 at 420K freestream b) Air at 1300K freestream 129

Figure 4-13: Comparison of high temperature air and low temperature CO_2 at M = 1 130

Figure 4-14: Low temperature Set 2 points at a) M = 2, b) M = 1, c) M = 0.5 133

Figure 4-15: Low temperature comparison with CO_2 at a total coolant flow rate of a) 7.3E-03 kg/min, b) 3.6E-03 kg/min c) 1.8E-03 kg/min.....136

Figure 4-16: Comparison of Set 1 and Set 2 calibration curves 137

List of Tables

TABLE ....Page

Table 3-1: Coolant *Re* and *h* at multiple conditions 77

Table 3-2: Mass flow controllers 98

Table 3-3: Uncertainty Analysis Representative Values 105

Table 3-4: Uncertainty in important non-dimensionalized parameters 106

Table 3-5: Repeatability comparison points 107

Table 4-1: LEFCT PSP Test Points 112

Table 4-2: PSP Data Points.....114

Table 4-3: LEFCT IR Tests Points 116

Table 4-4: Estimated leading edge IR points.....118

Table 4-5: Low Temperature Data points, Set 1.....120

Table 4-6: High Temperature Data Points.....126

Table 4-7: Low Temperature Data Points, Set 2.....131

1. Introduction

This thesis discusses film cooling as it relates to gas turbine engines. Film cooling schemes are used ubiquitously on modern turbine engines, since they allow the engine to operate beyond the melting point of turbine component materials. However, performing experiments at realistic engine temperature can be both expensive and dangerous, so many film cooling experiments are performed at near ambient conditions. Since thermophysical properties scale differently with temperature, it is difficult to scale results between near ambient and near engine conditions. This investigation sought to explore the relative importance of different parameters that are relevant to scaling film cooling results.

1.1. Film Cooling Motivation

To understand the motivation to investigate film cooling, one must consider the development of gas turbine engines for aviation. Gas turbine engines revolutionized aviation, as they outperformed the reciprocating engine in many key aspects, such as power to weight ratio, efficiency at high altitude, and reliability on long flights [1].

Of course, once gas turbine engines became common, attention was immediately turned to improving their performance, especially their power to weight ratio and efficiency. The power to weight ratio can be boosted by increasing the turbine inlet temperature (i.e. reaching higher combustion temperatures). Meanwhile, the efficiency can the improved by increasing the pressure ratio of the engine. Following the laws of thermodynamics, increasing overall pressure ratio also increases the turbine inlet temperature. Therefore, any improvement to engine performance will tend to increase the turbine inlet temperature.

Eventually, the engineers found that they ran into a barrier to ever-increasing engine performance: the melting point of the turbine component materials. To circumvent this performance limit, cooling schemes were introduced. Most cooling schemes consist of both internal cooling, which removes heat from the turbine blade, and film cooling, which reduces the heat transferred to the blade by forming a thin film of cooler gas over the blade surface. Note that the coolant must be at a higher pressure than the freestream to be successfully ejected and form the external film. Since the hottest parts of a turbine tend to also have the highest pressures, coolant is often drawn from the highest pressure stages of the compressor, which will decrease the mass flow through the combustor [1]. The loss incurred by the bleed of the coolant air must be balanced against the performance gains from higher turbine inlet temperatures to deduce the optimal amount of coolant to bleed in a given application.

A sizable body of research has been conducted on film cooling. Many of these studies were performed using near ambient temperatures, since high temperature models would be both expensive and challenging. Unfortunately, this practice leads to issues relating results to true engine conditions, because the flow physics dictate that not all of the nondimensional parameters relevant to film cooling can be matched simultaneously. Therefore, one must select which nondimensional parameters to match and which ones to neglect when performing near ambient tests. Determining the relative importance of different parameters in scaling film cooling performance would be a great boon for any researchers facing such decisions in future experimental endeavors.

1.2. **Overall Objectives**

The original objectives focused on the impact of different nondimensional parameters on the scaling of film cooling effectiveness, including the impact of scaling film cooling effectiveness

measurements between two test setups of varying size. However, during the course of this investigation, the role of the internal coolant became evident. Therefore, as part of this thesis, the relationships between internal coolant mass flow, coolant temperature, and film cooling effectiveness became specific parameters of interest to this investigation.

1.3. Additional Accomplishments

A variety of additional modifications to the Film Cooling Rig (FCR) and operating procedures were evaluated in the course of meeting the overall objectives of this project. Some of these modifications were relatively simple, while others involved replacing whole portions of the rig. These improvements included: a new coolant inlet design, a new boundary layer bleed, an investigation of window effects on IR data, and modifications to ignition procedures.

1.3.1. New Coolant Inlet Design

The tests in this project employed a new coolant inlet design, developed by Christian Schmiedel, a visiting researcher. Previous FCR tests by Ashby [2] noted an issue with nonuniformity in the coolant flow. A rudimentary investigation found that the coolant simply was not able to expand from the narrow inlet tube to the desired rectangular plenum in the required distance, so instead the coolant exited as a jet, attached to one side of the inlet area. The new design split the coolant flow into two tubes of equal length, with the goal of decreasing the jet length and allowing full dispersal of the coolant throughout the inlet plenum. The new design proved to be a significant improvement over the previous design.

1.3.2. New Boundary Layer Bleed Design

The second improvement was a new boundary layer bleed design, also developed by Christian Schmiedel. In previous investigations by Ashby [2], it was observed that the coolant

temperature increased dramatically in the short distance from entering the FCR to the film cooling holes. The heat was hypothesized to come from the hot freestream gas passing through the boundary layer bleed, which effectively formed an accidental counterflow heat exchanger. The new boundary layer bleed design featured an air gap between the bulk of the boundary layer bleed and the main test block containing the coolant flow passage, to help reduce thermal conduction. Comparison with data from Ashby [2] showed that the new boundary layer bleed design helped reduce the coolant temperature by as much as 50K at 1300K freestream conditions.

1.3.3. Investigation of Window Effects

The third improvement concerned the infrared window used for data collection. During testing, it was observed that the sapphire window used for optical access to the test section produced a "dark spot" that shifted based on the angle of the window. It was hypothesized that this spot was a reflection of the IR camera. To address the problem, the window was rotated slightly until the dark spot was no longer observed in the test area. This solution did produce a slight asymmetry in the flow pathway, but the difference was deemed small enough to be negligible. To further investigate the reflection issue, multiple window options were evaluated and compared. As part of that investigation, a set of IR windows with a coating designed to minimize reflection were acquired. Notably, the non-reflective coating is only available on silicon windows, which have a lower melting point than the sapphire windows typically used on the FCR. The sapphire and coated silicon windows exhibited similar performance. Using no window at all eliminated the reflection issue, but flow leaked out of the open hole, changing the flow field of the test section. Tilting the sapphire window down by about two degrees reduced the reflection, but allowed a small amount of flow to leak out of the test section.

Also, during high temperature tests, combustion products typically build up on the inside of the IR window. An investigation of this buildup via laser spectrometry suggests that it has a small impact on the IR transmissivity of the window. A simple method for cleaning off this buildup was tested, with good results, should it be desirous to do so.

1.3.4. Modification to Ignition Procedures

Lastly, an improvement to the startup procedure for the rig was developed. Previous protocol for igniting the FCR called for the propane fuel to be introduced to the toroidal reactor before the igniter was triggered. This method consistently produced a loud concussion, which threatened to damage the fragile ceramic insulating components of the FCR. It was suggested that we instead start the igniter before slowly increasing the propane feed. This method produces a much smoother transition to stable combustion.

2. Literature Review

In the 1960's, internal cooling schemes were developed that allowed turbines to operate beyond the temperature limits of their component materials. Soon after, experimentation began on film cooling, which is now used ubiquitously in turbine engines. Effective cooling can greatly improve the lifetime performance of a turbine. In fact, the operational life of a part can be doubled by reducing the temperature of the component by as little as 25K [3]. The downside to cooling is that the coolant must be compressed (which requires work output from the turbine) and cannot be used for combustion, if the usefulness of the coolant is to be maximized. Therefore, the work required to run the cooling scheme must be outweighed by the performance gained via the increased turbine inlet temperatures that the cooling scheme allows.

A vast array of film cooling schemes have been studied via many different methods and under a wide variety of different conditions. However, due to the expense, danger, and difficulty of testing at engine conditions, the bulk of this research has been conducted at near ambient conditions. Due to thermophysical property variation with temperature, scaling results between ambient and engine conditions proves quite difficult. Most recent work investigating the scaling problem is computational. Using the FCR, this thesis intends to approach the scaling of film cooling performance from an experimental angle.

Several film cooling topics are discussed in the following sections, such as film cooling fundamentals, geometric effects on film cooling, the effects of various flow characteristics, the impact of conjugate heat transfer, and different experimental techniques used to measure film cooling performance. Section 2.1 discusses the phenomena in a film cooling flow field and how to quantify film cooling performance. Section 2.2 discusses the impact of cooling hole spacing, injection angle, and coolant hole shape on film cooling performance. Section 2.3 discusses

important flow characteristics, including the Mach number, freestream turbulence, and internal coolant flow. Section 2.4 discusses conjugate heat transfer. Lastly, Section 2.5 discusses thermal and mass transfer experimental techniques and the heat-mass transfer analogy.

2.1. **Film Cooling Basics**

Film cooling helps cool a turbine component by producing a thin layer of relatively cool fluid over the surface of the component to protect it from the hot air from the combustor. Turbine blades are one component of particular interest, as they are thin and impinged upon directly by the hot core flow. Typically, air is bled from a high pressure stage in the compressor and ejected from holes in the turbine blades. Film cooling holes are often concentrated in three regions: the leading edge (sometimes called the showerhead region); the pressure side; and the suction side, as illustrated in Figure 2-1 from Han et al. [4]. The goal of a cooling scheme is to reduce the convective heat flux, q'', and the wall temperature, T_w, of the turbine blade.

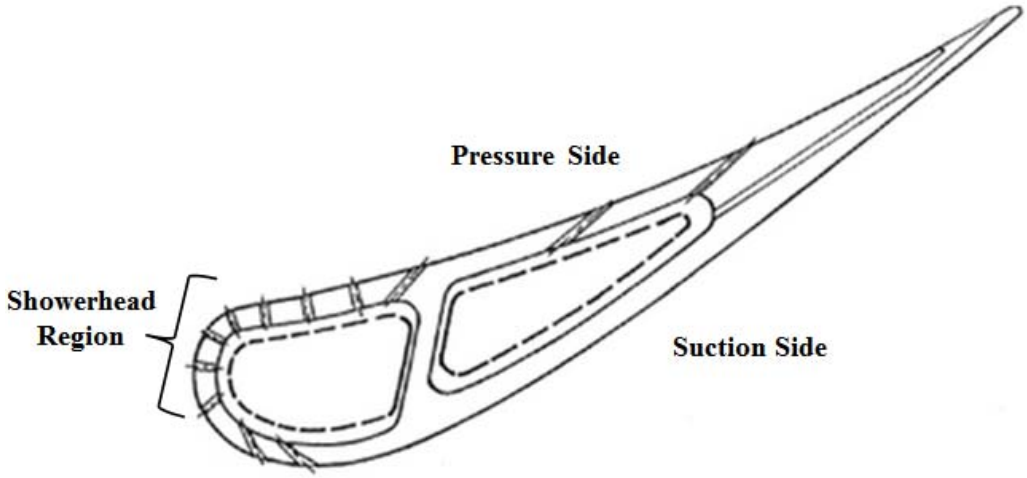

Figure 2-1: Sample turbine airfoil cooling scheme diagram (image from Han et al. [4]])

Heat flows from the hot combustion products to the turbine blade via convective heat transfer, frequently modeled by Newton's Law of Cooling [3].

$$q'' = h(T_{ref} - T_w) \tag{2-1}$$

where q'' is the heat flux to the turbine blade, h is the convective heat transfer coefficient, and T_{ref} is an appropriate reference temperature. As noted by Bogard and Thole [3], this law can be hard to use, as the selection of T_{ref} and measurement of h and T_{ref} can be challenging, amongst other difficulties. Figure 2-2 from Bogard and Thole illustrates the three temperatures relevant to the gas turbine heat transfer problem: the freestream gas temperature (T_g), the coolant temperature (T_c), and the temperature of the turbine blade surface (T_w).

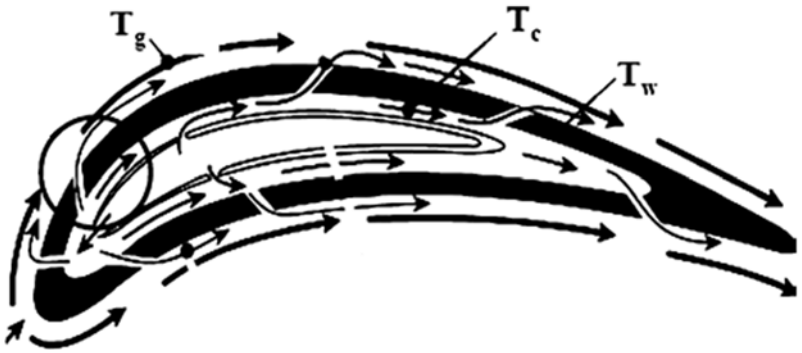

Figure 2-2: Turbine airfoil fluid flow diagram (from Bogard and Thole [3])

In Equation (2-1), T_{ref} must be the temperature of the fluid immediately above the blade surface [3]. When film cooling is present, this temperature is referred to as T_{film}. If the wall is assumed to be adiabatic, as can be approximated in low-temperature film cooling experiments, we can set T_{film} equal to the adiabatic wall temperature, T_{aw}, and rewrite Eq. (2-1) [3]

$$q''_f = h_f(T_{aw} - T_w) \tag{2-2}$$

where q''_f is the heat flux to the turbine blade and h_f is the heat transfer coefficient with film cooling present.

It is important to note that h_f is often different from the heat transfer coefficient without film cooling. This change is caused by the dynamics of the coolant jet. Fric and Roshko [5] used hot-

wire anemometry and smoke-seeded flow visualization to investigate the various vortex structures that are formed when a coolant jet enters the freestream, as shown in Figure 2-3.

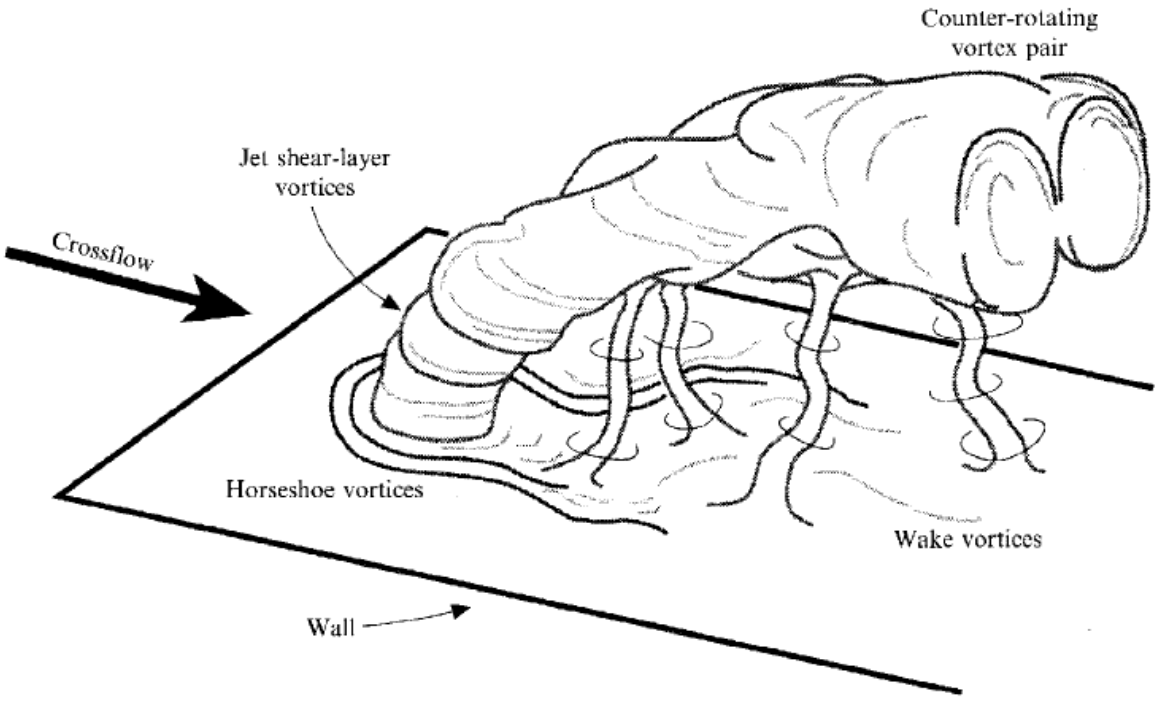

Figure 2-3: Dynamics of a coolant jet (from Fric and Roshko [5])

The jet shear-layer vortices are most prominent at the initial portion of the jet. They form due to a phenomenon known as the Kelvin-Helmholtz instability in the shear layer. The horseshoe vortices that form around the jet are similar to the ones that would be formed by a solid cylinder or other bluff body in the flow. Fric and Roshko argue that the wake vortices must appear due to an adverse pressure gradient that cause some separation effects near the wall. Although all of these structures are interesting to note, the counter-rotating vortex pair (CRVP) is often given the most attention, because it begins to form at the very start of the jet and eventually becomes the dominant flow structure downstream of the coolant hole [5].

Lawson et al. [6] note that since these vortices induce turbulence at the component surface, h_f will actually be higher than the convection coefficient without film cooling. An increase in h

would actually tend to increase the heat flux to the surface, which is counterproductive. It is clear that for a film cooling scheme to successfully cool a component, it must reduce T_{film} enough to outweigh the effect of the increased heat transfer coefficient.

2.1.1. Performance Metrics

Film cooling performance is often quantified using one of two different nondimensionalized values. The adiabatic film cooling effectiveness (η) uses the freestream, adiabatic wall, and coolant temperatures [3]

$$\eta = \frac{T_\infty - T_{aw}}{T_\infty - T_{c,e}} \tag{2-3}$$

where $T_{c,e}$ is the coolant temperature at the film cooling hole exit, specifically. The advantage of η is that it isolates the effect of the coolant film from the internal cooling effects, allowing for better comparison between different coolant hole schemes.

However, in real applications, the turbine blade is not adiabatic, making measurement of η difficult. Therefore, for real, metallic airfoils, the overall film cooling effectiveness ϕ is utilized. The overall film cooling effectiveness accounts for the internal cooling effects present with a conductive plate [3]. Note that ϕ uses the wall temperature, T_w, in place of T_{aw}, since the wall is no longer assumed to be adiabatic. Additionally, the coolant temperature at the inlet of the internal cooling plenum ($T_{c,i}$) is used instead of the coolant exit temperature, since the coolant can now pick up heat from the wall as it passes through the hole.

$$\phi = \frac{T_\infty - T_w}{T_\infty - T_{c,i}} \tag{2-4}$$

Values of ϕ and η range from 0 to 1 with better cooling at higher values. Many of the works referenced throughout this chapter use one or both of these parameters to evaluate different cooling hole schemes and conditions. For example, Eberly et al. [7] used η to evaluate the effect of coolant

density, Williams et al. [8] used ϕ to investigate the effect of internal cooling and other variables, and Albert et al. [9] used both parameters to investigate their test piece. These papers and many others will be addressed in further detail in the following sections, to illuminate the specific topics to which they pertain. Typically, values for η and ϕ within the literature will land within a range of 0.4-0.8, depending on the details of the experimental setup and conditions.

2.1.2. Characteristic Parameters

Like most fluid dynamics applications, film cooling is governed by nondimensional parameters. Matching these parameters should match the flow physics between experiments. Many of these parameters are recognizable from other fluid dynamics and heat transfer studies, such as the Reynolds number (Re), and Prandtl number (Pr):

$$Re = \frac{\rho U x}{\mu} = \frac{U x}{\nu} \tag{2-5}$$

$$Pr = \frac{\mu c_p}{k_{gas}} = \frac{\nu}{\alpha} \tag{2-6}$$

Where ρ is the fluid density, x is an appropriate length scale, μ is the dynamic viscosity of the fluid, c_p is the specific heat of the fluid, k_{gas} is the thermal conductivity of the fluid, ν is the kinematic viscosity of the fluid, and α is the thermal diffusivity of the fluid. Note that the freestream and coolant flows will each have their own Reynolds and Prandtl numbers, respectively. The Reynolds number describes the relative importance of inertia and viscosity for momentum transport within a flow, while the Prandtl number describes the relative importance of viscous and thermal diffusion for the energy transport within a flow. In heat transfer applications, it is found that these two parameters can be empirically correlated to the Nusselt number (Nu), which describes the relative impact of convection and conduction in a fluid [10]

$$Nu = \frac{hx}{k_{gas}} \tag{2-7}$$

Where h is the convection coefficient, x is the characteristic length and k_{gas} is the thermal conductivity of the fluid. The correlations greatly depend on the flow application, and so are mostly useful in specific applications that use common shapes, like circular tubes or flat plates [10].

The Biot number (Bi) is another very important parameter for film cooling. It relates the convection to the wall to the conduction through the wall

$$Bi = \frac{ht}{k_m} \tag{2-8}$$

where k_m is the conductivity of the wall and t is the wall thickness. One could define Bi based on the external, internal, or coolant hole convection coefficient. Martiny et al. [11] used a mathematical effusion plate model of a single cooling hole to perform a parameter study on the three different Biot numbers and various other parameters. Because it was a mathematical model, they were able to vary the Biot numbers independently of all other parameters. They found that although the overall film cooling effectiveness was affected by all three, the Biot number based on the freestream convection coefficient, h_e, had a larger impact than the other two. For an external Biot number increase from .005 to .025, ϕ dropped from 0.87 to 0.67. In contrast, ϕ only rose from 0.67 to 0.73 over the same interval for the internal Biot number, and 0.61 to 0.7 for the coolant hole Biot number. The Biot numbers used in the parameter study were so small due to the dimensions and properties of the experimental test piece that Martiny et al. used to compare with the predictions of their mathematical model. Martiny et al. reasoned that the external Biot number had a larger impact on ϕ because it governed the heat input, whereas the other two mechanisms govern heat absorption by the coolant; if one absorption Biot number is low, the other can compensate, but the same is not true for the external Biot number. Therefore, the external Biot

number based on the external is almost exclusively considered. The term "Biot number" is typically used in literature to exclusively address the external Biot number. This convention will be followed in the remainder of this document. Typical external Biot numbers in actual gas turbine engine applications range from 0.3 to 0.6 [6].

Albert et al. [9] found that matching Bi is quite important for comparing near ambient and near engine temperature cases. They used a foam test piece (Bi = 40) and an alumina test piece (Bi = 1.2) of identical dimensions. They found that lower Biot numbers indicate a greater level of conduction as compared to convection, which will result in a more uniform surface temperature and a larger impact from internal cooling [9]. In a turbine engine, a uniform temperature helps reduce the thermal stresses in turbine components, so lower Biot numbers are desirable. For experimental work, using an engine-representative Bi realistically models the impact of internal cooling and provides a realistic view of the ϕ distribution across the component surface.

The freestream Bi can be used with the ratio of the external and internal convection coefficients (h_e and h_i) and the coolant warming factor (χ) to relate ϕ to η [12]. The coolant warming factor is necessary to account for the change in coolant temperature as it picks up heat within the coolant holes, since ϕ uses the internal coolant temperature, but η uses the external coolant temperature. For high coolant mass flows, χ is sometimes be assumed to be one, as in the case of experiments by Dees et al. [13]. However, experiments by Williams et al. [8] had a χ of 0.7-0.8 depending on the test point. Mathematical analysis by Esgar [14] suggests that typical engine values of χ lie in the 0.7-0.8 range. When χ cannot be measured directly, it is typically due to difficulty accurately measuring T_{ce}. In these cases, T_{ce} can be calculated from the test piece temperature, the coolant hole dimensions, and the convection heat transfer coefficient within the

coolant hole. Judging from Equation 2-10, it is clear that lower χ values will result in lower ϕ values, so higher χ values are beneficial.

$$\chi = \frac{T_\infty - T_{ce}}{T_\infty - T_{ci}} \tag{2-9}$$

$$\phi = \frac{\chi\eta\left(Bi + \frac{h_e}{h_i}\right) + 1}{Bi + \frac{h_e}{h_i} + 1} \tag{2-10}$$

Other widely used parameters are specific to film cooling, such as the density ratio (DR), velocity ratio (VR), blowing ratio or mass flux ratio (M), and momentum flux ratio (I) [3].

$$DR = \frac{\rho_c}{\rho_\infty} \tag{2-11}$$

$$VR = \frac{U_c}{U_\infty} \tag{2-12}$$

$$M = \frac{\rho_c U_c}{\rho_\infty U_\infty} = DR \times VR \tag{2-13}$$

$$I = \frac{\rho_c U_c^2}{\rho_\infty U_\infty^2} = M \times VR = DR \times VR^2 = \frac{M^2}{DR} \tag{2-14}$$

where the subscripts c and ∞ refer to the coolant and freestream fluids, respectively. Many experiments match M, since it is easily varied by controlling the coolant mass flow. The importance of I has also been investigated, since it scales the ability of the coolant jet to enter the freestream [3]. If I is too high, the coolant jet can separate from the surface, and blow uselessly into the freestream. Eberly and Thole [7] performed particle image velocimetry (PIV) tests that illustrate this phenomena on a flat plate with coolant holes angled at 30 degrees to the surface. For M = 0.6, the coolant flow did not separate at either $DR = 1.2$ or $DR = 1.6$. At an M of 1.0, which corresponded to an I of 0.64 and 0.87 for the high and low DRs respectively, the jet began to show

signs of separation. The jets were fully separated at the next set of data points at M = 2, which corresponded to an I = 3.3 and I = 2.5 for the low and high DR cases, respectively. This is consistent with the conventional wisdom that separation will tend to occur at I values above one for the commonly employed coolant scheme utilized by Eberly and Thole. The separation was more apparent at lower DR, which corresponds to a higher I. Eberly and Thole were able to conclude from their data that a lower I helps prevent separation, and a higher DR tends to increase adiabatic film cooling effectiveness when M is held constant. The impact of DR was also observed by Narzary et al. [15] using very different test conditions and methods, but with the same basic conclusion: increasing DR tends to increase adiabatic film cooling effectiveness. Since matching DR and just one other of these four flow parameters forces all of them to be matched, DR stands out as a useful parameter to match.

A computational study by Greiner et al. [16] explored a variety of combinations of different parameters mentioned above to scale η from near ambient to near engine temperatures for a laidback, fan-shaped coolant hole in an adiabatic surface. They found that matching M and Re_∞ with an unmatched DR of unity led to an underprediction of η. Likewise, matching M and DR but not Re_∞ led to higher mass flows and an overprediction of η. The best scaling was observed when M, DR, and Re_∞ were all matched simultaneously. However, even this case did not provide a perfect prediction. Due to thermophysical property variations, it is impossible to match both the freestream Reynolds number (Re_∞) and the coolant Reynolds number (Re_c) simultaneously when M is held constant [16]. Greiner et al. found that matching M, DR, and Re_∞ gave slightly better overall results than matching M, DR, and Re_c, but averaging the results of the two cases produced a very close match everywhere except the region near the hole.

Rutledge et al. [17] suggested another film cooling parameter, the Advective Capacity Ratio (ACR), which describes how much heat the coolant can absorb from the freestream flow.

$$ACR = \frac{\rho_c u_c c_{p,c}}{\rho_\infty u_\infty c_{p,\infty}} \tag{2-15}$$

The ACR is commonly neglected in film cooling studies, but analytical work by Rutledge et al. suggests it may play an important role in scaling film cooling effectiveness [17]. Using Computational Flow Dynamics (CFD), a single cooling hole was modeled and the coolant properties varied to examine their effects. These simulations used a symmetric airfoil with a single coolant hole in an open-loop wind tunnel. Adiabatic effectiveness was assessed using both IR techniques and Pressure Sensitive Paint, discussed in Section 2.5. The results showed that for typical near-ambient test conditions, using an *ACR* that is higher than the engine condition ACR would over-predict η even when *M* and *I* were matched. Experiments by Wiese et al. [18] found that ACR scaled the magnitude of η more accurately than I, while *I* scaled the shape and location of the η distribution more accurately. These experiments used a symmetric airfoil with a single coolant hole in an open-loop wind tunnel. Adiabatic effectiveness was assessed using both IR techniques and Pressure Sensitive Paint, discussed in Section 2.5. Altogether, the results of these investigations could suggest that while *I* better predicts the momentum (and therefore the shape and location) of the coolant jet, *ACR* better represents the thermal transfer effects that are occurring.

For overall film cooling effectiveness investigations, it is important to take the internal cooling flow into account. For the purposes of this investigation, the term "extra rows of cooling", or *ER,* was defined, based on procedures by Lynch [19] and Ashby [2]. This variable nondimensionalizes the excess coolant flowing through the coolant channel by the coolant exiting the film cooling holes. The excess coolant flow is the flow through the coolant channel that does

not exit the film cooling holes, as described in Section 3.1.3. Equation 2-16 shows the calculation for *ER*, where $\dot{m}_{c,in}$ is the total coolant mass flow and $\dot{m}_{film}$ is the coolant mass flow that exits through the film cooling holes.

$$\mathrm{ER} = \frac{\dot{m}_{c,in} - \dot{m}_{film}}{\dot{m}_{film}} \tag{2-16}$$

2.1.3. Additional Performance Metrics

As discussed previously, the addition of film cooling can actually cause turbulence near a component surface, increasing the heat transfer coefficient. On the other hand, the flow of coolant reduces T_{film}, which is a key temperature driving the heat transfer to the component. It would be helpful, then, to define a parameter that describes whether the heat flux to the component has actually increased or decreased once film cooling has been added. The net heat flux reduction (Δq_r) does exactly that. It is often used to quantify the performance of film cooling schemes [6]

$$\Delta q_r = 1 - \frac{q_f''}{q_0''} = 1 - \frac{h_f(T_{aw} - T_w)}{h_0(T_\infty - T_w)} = 1 - \frac{h_f}{h_0}\left(\frac{1-\eta}{\phi}\right) \tag{2-17}$$

where the subscript 0 represents conditions without film cooling. The adiabatic wall can be approximated in low temperature experiments by using models with very low thermal conductivities or mass-transfer methods, as discussed in Section 2.5. Many studies exclusively measure η and $\frac{h_f}{h_0}$, while simply assuming a constant ϕ value. Note that if the freestream and coolant temperatures are constant, then T_w must be constant for the constant ϕ assumption to be true. Positive values of Δq_r indicate decreased heat flux to the turbine blade, so larger values of Δq_r are desired. Increasing the overall or adiabatic film cooling effectiveness indicates that the

cooling scheme is more effective, increasing Δq_r. Likewise, a lower h_f means less heat is convected to the surface, so Δq_r will increase.

Ghorab [20] provides an example of how Δq_r can be applied. He used an adiabatic model and an aluminum plate at low temperature conditions to find the adiabatic effectiveness and h_f/h_0 ratios for a standard scheme, a hybrid scheme, and a Louver scheme. The hybrid and Louver schemes utilize shaped holes to induce greater lateral spreading of coolant and reduce the turbulence generated by the jet at the surface. The topic of shaped holes is discussed further in Section 2.2.3. Ghorab found that h_f/h_0 was higher for both hole patterns than for published data on standard cylindrical holes, since the standard holes generate more turbulence at the surface of the plate. Also, h_f/h_0 increased with blowing ratio for the standard holes, but held relatively steady for the two hole schemes Ghorab tested. Ghorab assumed a value of $0.\overline{66}$ for the overall effectiveness, noting that this is a reasonable assumption because ϕ typically ranges from 0.5-0.7 in actual engines. Using the calculated η and h_f/h_0 ratios and the assumed ϕ value, Ghorab was then able to calculate Δq_r for the two cooling schemes. Both schemes showed Δq_r values of about 1.5 near the hole, decreasing steadily to roughly 0.75 at x/d of 12 downstream of the holes. Both schemes produced lower Δq_r values at lower blowing ratios, but the Louver scheme displayed a much more pronounced influence than the hybrid scheme.

Rutledge et al. [12] expound upon several issues with Δq_r. Essentially, the goal of film cooling is to reduce T_w, not the heat flux, so Δq_r may not be as useful of a metric as ϕ. Also, any reduction in heat flux that Δq_r predicts would decrease T_w, which ends up violating the initial assumption that T_w is constant. Additionally, careful inspection of Eq. (2-17) reveals that Δq_r is maximized when q_f'' is zero, which can be achieved when the turbine blade reaches thermal equilibrium with the freestream flow. The entire point of film cooling is to keep the turbine blade

below the temperature of the freestream flow. To replace Δq_r, Rutledge et al. proposed the $\Delta\phi$ method, where $\Delta\phi$ is the change in ϕ produced by adding film cooling to an internal cooling scheme.

$$\Delta\phi = \phi - \phi_0 = \frac{T_{w0} - T_w}{T_\infty - T_c} \tag{2-18}$$

Where ϕ_0 and T_{w0} refer to the overall effectiveness and surface temperature for a case with only internal cooling.

Since ϕ provides direct knowledge of the turbine surface temperature, the $\Delta\phi$ method provides a much more quantifiable measure of the impact of a cooling scheme. It can also be used to compare two different cooling schemes or find the maximum allowable freestream temperature for a given cooling scheme [12]. Williams et al. [8] evaluated the impact of internal cooling using a method similar to the $\Delta\phi$ method. After acquiring ϕ measurements on their test piece, they blocked two of the 14 coolant holes in their single-row scheme and retook ϕ measurements in that region to represent ϕ_0. Williams et al. note that their method relies on the assumption that plugging the coolant holes does not affect the internal flow patterns within the test piece. Although they did not report $\Delta\phi$ as such, they measured ϕ of 0.32 and ϕ_0 of 0.28 using the stated method, leading to a $\Delta\phi$ of 0.04. This result shows that the film cooling scheme is technically an improvement over purely internal cooling for this case, but the improvement is quite small.

2.2. Cooling Geometry Effects

The geometry of the film cooling holes can have quite an impact on the effectiveness of a film cooling scheme. Figure 2-4 from Ashby [2] illustrates some basic coolant hole dimensions. The pitch (P), is the distance between the coolant holes, while L is the length of the hole. Both of these dimensions are often nondimensionalized by the coolant hole diameter (d). The coolant

injection angle (α) is usually around 30 degrees [3]. Shallow angles help prevent coolant jet separation, but are more difficult to machine. The shape of the actual hole can also impact film cooling effectiveness, as discussed in the following sections.

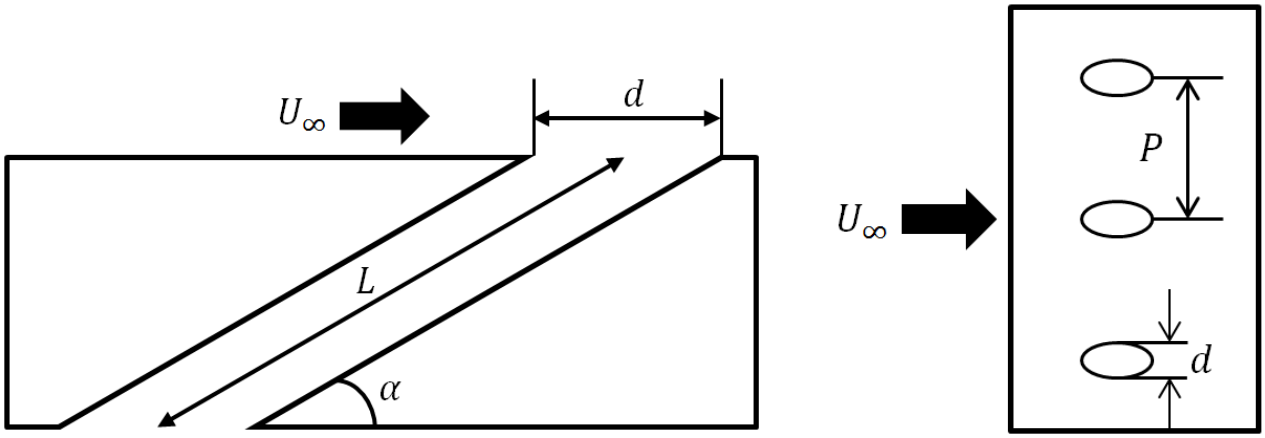

Figure 2-4: Schematic of cylindrical cooling hole geometry: (a) side view and (b) top view (image from Ashby [11])

2.2.1. Coolant Hole Spacing Effects

The coolant hole spacing influences how much of the surface the coolant film will cover. At a large pitch spacing, the coolant jets tend to act independently. Baldauf et al. [21] found that for $DR = 1.8$, α = 30 degrees, a single row of 5 coolant holes acted as independent jets for P/d values of 3 and 5. However, at P/d of 2, the jets began to interact, as shown by the improved laterally averaged adiabatic effectiveness ($\overline{\eta}$) trends at higher blowing ratios. If the pitch spacing is large enough that the jets do not interact, the effectiveness of a row of holes can be predicted from the performance of a single hole [3].

Multiple rows of cooling holes are often used to ensure full coverage of the surface [3]. This method is commonly used in the combustor of turbine engines. Once a cooling scheme

achieves full coverage, the film cooling effectiveness holds fairly constant, even upon the addition of more rows.

Harrington et al. [22] provide an example of film cooling with multiple rows over a flat plate with normal coolant injection ($\alpha = 0$ degrees). Ten rows of nine holes each were staggered so that each row was not directly lined up with the preceding row. Depending on the blowing ratio, it took between four and eight rows before reaching the full coverage condition, where additional rows did not improve the measured adiabatic effectiveness. If the rows of holes did not interact with each other, axial superposition could predict the effectiveness from the performance of a single row, but simply overlaying the effectiveness distribution of a single hole over itself at the appropriate distance downstream. For Harrington et al., an axial superposition method was able to accurately predict the effectiveness out to the third row, but beyond that point it became unreliable, because the rows began to interact and generate a uniform layer of coolant. Once full coverage was reached, the difference between predicted and measured $\overline{\eta}$ was approximately 15%.

Sasaki et al. [23] also investigated the effect of multiple rows of cooling. They used a total of six models, divided into two sets of three. The first set had P/d of 5, whereas the second set had P/d of 10. Each set had three models with one, four, and seven staggered rows of holes respectively. They found that axial superposition predicted the laterally averaged adiabatic film cooling effectiveness of the P/d = 10 multi-row cases quite well out to at least the third row of holes for blowing ratios between 0.15 and 0.5. For P/d = 5, axial superposition also worked well at the lowest blowing ratio of 0.15, but overestimated $\overline{\eta}$ at higher blowing ratios. These results illustrate that superposition is useful for predicting the performance of multi-row cooling schemes only so long as the coolant jets have not interacted to form a uniform coolant layer.

2.2.2. Coolant Injection Angle Effects

The coolant injection angle, illustrated previously in Figure 2-4, has a significant impact on the film cooling effectiveness, especially regarding separation of the coolant jet. As α increases, separation becomes more likely. Baldauf et al. [21] investigated cases for α = 30, 60, and 90 degrees with DR = 1.8 and P/d = 3 with holes oriented parallel to the freestream (also called streamwise). At low blowing ratios, the peak $\overline{\eta}$ dropped 30% as α increased from 30 to 90 degrees. Interestingly, peak $\overline{\eta}$ values actually increased with increasing α when M was greater than 1.2, but the actual performance of the scheme was notably worse than the lower blowing ratio cases.

If the coolant is not injected parallel to the freestream flow, it is said to have a compound injection angle, as illustrated in Figure 2-5. Compound angles are often used on steeply curved regions of a turbine blade, such as near the leading edge, where the coolant holes would otherwise have to suffer a large α to be realistically machinable [24]. As previously discussed, smaller values of α are more desirable, so compound angles are employed to work around the predicament. Because compound angles also present a larger jet profile to the freestream, the coolant is more spread out, increasing the surface coverage [3]. Unfortunately, this same aspect increases the turbulent mixing of the jet with the hot freestream gas, which can offset the benefits of the increased coverage.

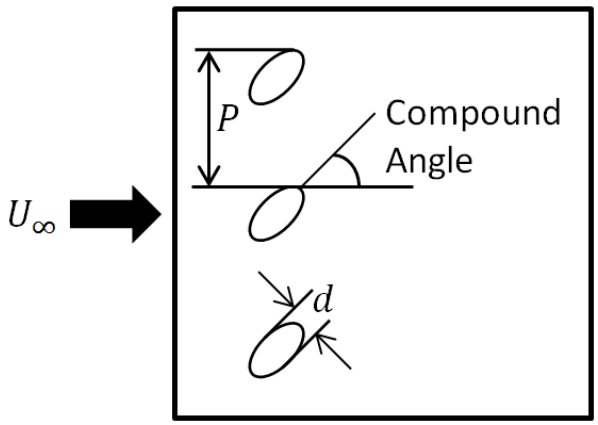

Figure 2-5: Schematic of cooling hole compound angle

One examination of compound injection angles by Dittmar et al. [25] showed that the compound angle did in fact produce more uniform coolant spread over a gently curved surface than a comparable streamwise case, based on the measured η contours at blowing ratios 0.5, 1, 1.5, and 3.0. However, the streamwise case generated higher peak η values immediately downstream of the holes. In the end, laterally averaged η values for both cases were nearly identical. This experiment also made use of fan-shaped holes, which leads us to the effects of the coolant hole shape.

2.2.3. Coolant Hole Shape Effects

In a perfect film cooling world, coolant would flow parallel to the surface out of a thin slot, producing a uniform film as shown in Figure 2-6. Unfortunately, in the real world this slot would compromise the structural integrity of a turbine blade and prove difficult to manufacture [24].

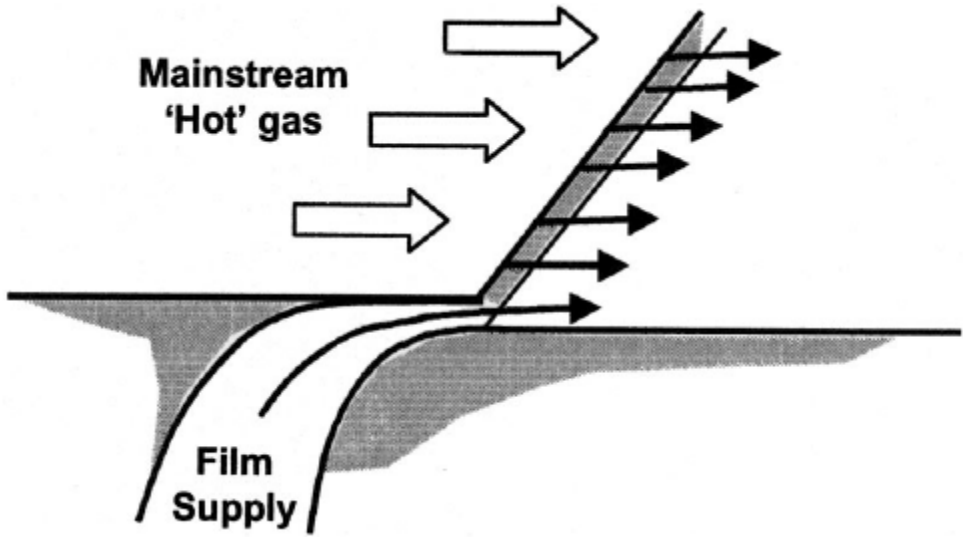

Figure 2-6: Continuous 2D slot cooling scheme (image from Bunker [24])

Cylindrical coolant holes are commonly used due to their simplicity and machinability. Clearly, these holes do not mimic the idealized slot case very well. Two different methods of modifying the traditional cylindrical hole have been developed to help film cooling schemes achieve better lateral coverage and resistance to jet separation. The first, called shaped holes, alter the exit of the coolant hole. The second places the coolant hole into a recess, or trench, in the surface.

2.2.3.1. Shaped Holes

Shaped holes essentially expand the hole exit to encourage diffusion [24]. The diffusion reduces the momentum of the coolant jet, which reduces mixing losses and enhances lateral coolant spreading. The two most common shaped hole modifications are layback and fan-shaping. These shaped hole geometries are illustrated in Figure 2-7 where L represents the hole length, α represents the hole angle relative to the surface, β represents the flare angle of the fan shape, and δ represents the layback angle of the hole. When discussing shaped holes, the cylindrical part of the hole prior to the shaped exit is referred to as the hole throat. In Figure 2-7, D represents the

cooling hole throat diameter (referred to as d in the rest of this document) and L_T represents the length of the hole throat. High values of β and δ risk flow separation within the hole, so shaped hole designs normally keep these two angles within 10-15 degrees [24].

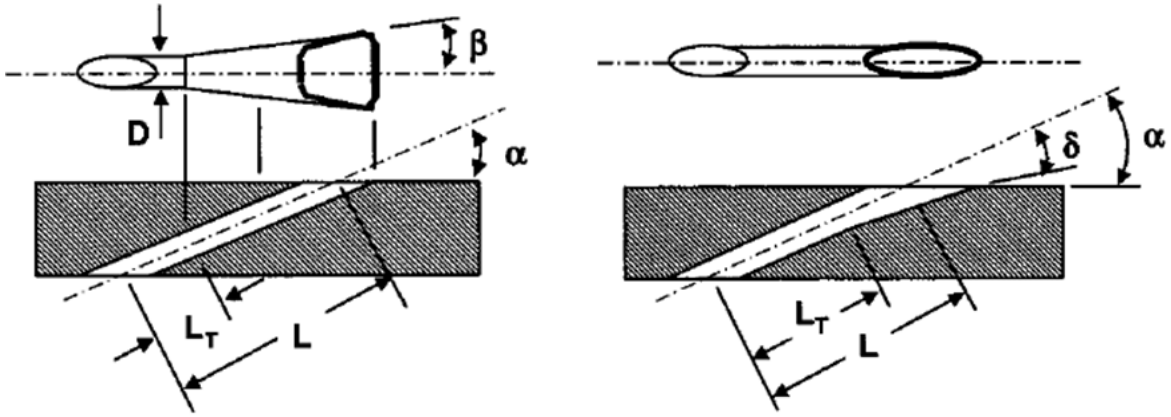

(a) **(b)**

Figure 2-7: Common geometries for holes with shaped exits: (a) fan-shaped hole, (b) laidback hole (images from Bunker [14])

To compare the performance of cylindrical and shaped holes, Saumweber et al. [26] investigated three cooling hole shapes: cylindrical, fan-shaped with β = 14 degrees, and laidback fan-shaped with β = 14 degrees and δ = 15 degrees. All sets of holes were oriented streamwise on a flat plate, with P/d = 4, DR = 1.7, and α = 30 degrees at blowing ratios ranging from M = 0.5 to 2.5. The coolant jets from the shaped holes remained attached to the surface at all blowing ratios and displayed enough coolant spreading that they produced a relatively uniform coolant film. At M = 0.5 the shaped holes achieved a 40% greater laterally averaged adiabatic effectiveness than the cylindrical holes. The performance of the two types of shaped holes was nearly identical, which suggests that adding a layback to an already fan-shaped hole does not have much of an impact.

Reiss and Bölcs [27] experimented with mutli-row cooling schemes in a showerhead configuration using cylindrical, fan-shaped, and laidback holes. For two different freestream Reynolds numbers, they found that the laidback holes achieved the best performance, with peak

adiabatic effectiveness values as high as 0.5. Although the fan-shaped holes outperformed the cylindrical holes at high blowing ratios, they did not perform as well as the laidback holes under most conditions. The exception was for blowing ratios of 1.3 and above at the higher Re_∞ case. Under these conditions, the fan-shaped hole showed much higher effectiveness near the hole, before eventually leveling out with the other hole shapes further downstream. Reiss and Bölcs suggest that the boundary layer was thin enough at the high Re_∞ case that the laidback holes separated at the higher blowing ratios, while the fan-shaped holes did not. The equivalent effectiveness downstream suggests the jets were eventually pushed back to the surface by the high-momentum freestream, reattaching them.

2.2.3.2. Trenched Holes

Trenched holes are standard cylindrical holes placed within a shallow recess, as shown in Figure 2-8 from Bunker et al. [28] where S is the depth of the trench and W is the axial width. This concept was suggested due to its relative ease of manufacture, since it does not require the kind of precision machining necessitated by shaped holes. For applications where the component is to be coated with a Thermal Barrier Coating (TBC) or something similar, the trench could be created by simply masking the desired trench region and applying the surface coating around it, forming the trench. For typical streamwise injection angles, the wall of the recess will deflect coolant flow, forcing the coolant to fill the recess before seeping out into the freestream. This method increases lateral coolant spreading and reduces the risk of separation

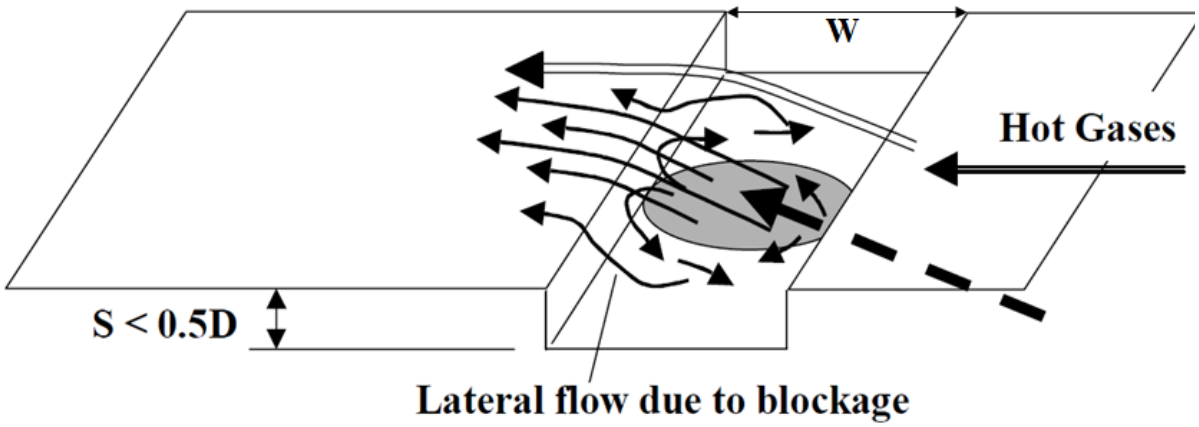

Figure 2-8: Shallow surface recess flow interaction diagram (image from Bunker [28])

.

Experiments by Bunker [28] utilized a long trench that held an entire row of holes. First, two trenched schemes were tested with spanwise-oriented holes (perpendicular to the freestream flow). The trenches had trench depths S/d = 3 and trench widths of W/d = 1.13 and 1.5 respectively. The trenched schemes were also compared to a scheme with the same hole shapes, orientations, and sizes, but without a trench. All cooling schemes had α = 30 degrees, P/d = 4, and DR = 1.8 over the range M = 0.75 to 4.

For all testing conditions, the narrow trenches proved superior to the wider trenches. The trench schemes displayed buildup of coolant on the side the coolant was flowing towards, leading to a lopsided effectiveness distribution. Additional tests were performed using a shallower trench with streamwise oriented holes that had a depth S/d = 0.43 and a width of W/d = 2. The new design alleviated the distribution issues experiences with the other trenches, and displayed a 50-75% greater η compared to similar cylindrical holes within x/d < 40, which rivals the performance of shaped holes.

Fric and Campbell [29] designed the cratered hole based on the trenched hole idea. This sort of hole can be produced by plugging the cylindrical hole prior to the application of Thermal

Barrier Coatings (TBCs) or surface treatments designed to prolong turbine life. The cratered hole concept was compared to normal holes using a pair of stainless steel test pieces, each with a row of five cooling holes, spaced at an *x/d* of 6.5. The hole geometry for the cratered holes was produced by simply adding a plate on top of the test piece with holes that overlapped the coolant hole exits, creating a cratered hole as shown in Figure 2-9.

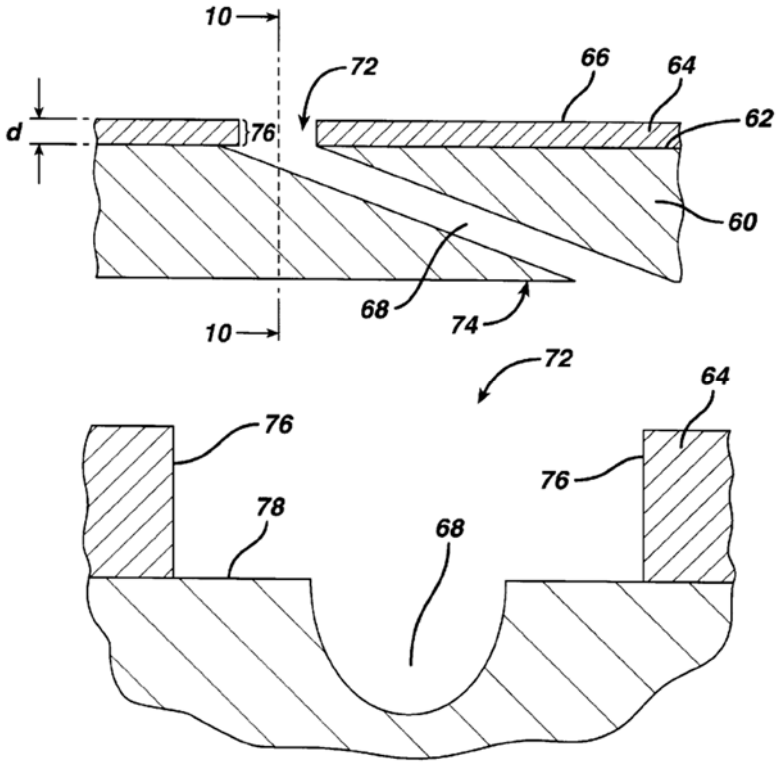

Figure 2-9: Cratered hole test geometry, side view (top) and cutaway view through plane 10 (bottom) (images from Fric and Campbell [29])

The hole diameter was 0.1 inch, angled at 20 degrees relative to the surface. The crater was 0.235 inches in diameter and 0.075 inches deep. The cratered holes achieved much greater η values than the regular cylindrical holes, as shown in Figure 2-10. The increase in η for the cratered holes is especially noticeable in the near-hole region. It is unusual that η is displayed as a percentage, but it is equivalent to previous discussion of η (e.g. η = 45% is equivalent to η = 0.45). All tests were performed with air coolant at a *DR* of 1.9. The freestream had a Reynolds number of 10,000

and was at 589K. One interesting trend is that η keeps increasing with M for the cratered holes, whereas it actually drops with M for the cylindrical holes. This result suggests that the cratered hole is helping to prevent separation.

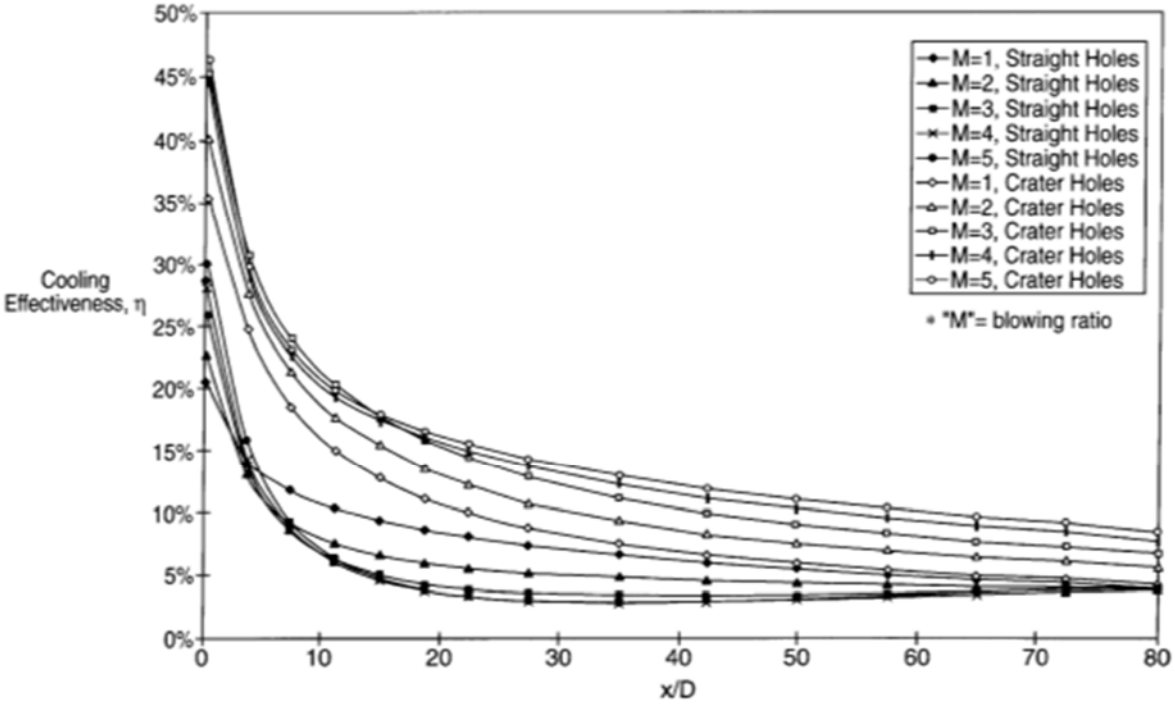

Figure 2-10: Cratered hole vs. normal holes (from Fric and Campbell [29])

2.3. Flow Characteristic Effects

Flow characteristics such as freestream Mach number (Ma_∞) and freestream turbulence intensity (Tu) could potentially impact the effectiveness of a film cooling scheme. Additionally, the overall effectiveness could potentially be affected by the nature of the internal flow of the coolant, as different coolant feeding methods and velocities produce different flow fields along the inner surface of the test piece.

2.3.1. Mach Effects

Within the sonic regime, freestream Mach number can have noteworthy impact on a film cooling scheme. Gritsch et al. [30] tested three holes with distinct geometries on a flat plate at blowing ratios ranging from M = 0.25 to 2.0 and freestream Mach numbers of Ma_∞ = 0.3, 0.6, and 1.2 with a density ratio of DR = 1.85. The hole geometries consisted of a cylindrical hole, a fan-shaped hole with a flare angle of β = 14 degrees, and a laidback fan-shaped hole with β = 14 degrees and layback angle δ = 15 degrees. Each hole had an injection angle of α = 30 degrees. The cylindrical holes experienced a much different effect from supersonic freestream flow than did the shaped hole geometries, but all of the holes experienced an increase in $\overline{\eta}$ at supersonic speeds.

For a subsonic freestream (Ma_∞ = 0.3 and 0.6), the laterally averaged film cooling effectiveness was mostly unaffected by the freestream Mach number [30]. At a supersonic freestream, the coolant jet obstructs the freestream flow, producing a bow shock upstream of the hole. The resulting pressure gradient and downstream shocks force the coolant jet back towards the surface, which increases the film cooling effectiveness. This phenomena was observed for all three geometries, although it was less pronounced for the shaped holes due to the lower jet momentum.

Anderson et al. [31] studied much lower freestream Mach numbers, ranging from 0.029 to 0.154. They used shaped holes on a flat plate at a DR of 1.8 to assess the impact of Mach number on adiabatic film cooling effectiveness. At blowing ratios of 1, 2, and 3, η was found to be rather insensitive to Mach number, which agrees with the previously discussed findings.

2.3.2. Freestream Turbulence Effects

Freestream turbulence tends to increase the mixing of the coolant with the hot freestream flow. Baldauf et al. [21] investigated the impact of freestream turbulence on cylindrical holes inclined at α = 30 degrees by varying Tu from 1.5% to 4% at blowing ratios of M = 0.4, 0.83, and 1.7. While the peak $\overline{\eta}$ values near the hole location stayed steady, $\overline{\eta}$ tended to decrease downstream of the holes as Tu increased.

In parallel with their aforementioned study on shaped holes, Saumweber et al. [26] investigated the effect of freestream turbulence intensity on adiabatic cooling effectiveness by varying Tu from 3.6% to 11%. Increased mixing at higher Tu values reduced η for all blowing ratios and hole shapes, as long as the jet did not separate. The drop in η could reach as high as 30% for the shaped holes and 40% for the cylindrical holes. Interestingly, at high blowing ratios, when the cylindrical holes separated from the surface, higher values of Tu actually increased the laterally averaged η, because the turbulence brought the coolant back down to the surface.

2.3.3. Internal Flow Effects

A plenum coolant feed is commonly used for film cooling experiments. Although convenient, a plenum does not usually represent the actual conditions found in turbine engine hardware. To study the effect of coolant feed flow Mach number, Thole et al. [32] employed a large cylindrical cooling hole with α = 30 degrees on a flat plate at a freestream Mach number of Ma_∞ = 0.25. The coolant was fed parallel to the freestream flow and the coolant Mach number (Ma_c) was varied between Ma_c = 0 and 0.5 at the hole entrance. Laser Doppler Velocimetry (LDV) was used to find flowfield velocities and turbulence intensities. The results of these tests suggest that the turbulence intensity at the hole is minimized by matching the coolant Mach number to the freestream Mach number. When Ma_c is lower than Ma_∞, the coolant will tend to

separate from the downstream edge of the hole entrance, whereas when Ma_c is higher than Ma_∞, the coolant will separate from the upstream edge of the hole entrance. Both cases result in skewed coolant jets, more turbulence, and lower film cooling effectiveness values.

Alongside their previously mentioned studies of freestream Mach number, Gritsch et al. [30] investigated the effect of coolant Mach number at Ma_c of 0 and 0.6 with two different coolant flow orientations, one parallel and one perpendicular to the freestream flow. Both the coolant Mach number and the orientation demonstrated an impact on the laterally averaged adiabatic film cooling effectiveness. The impact was most noticeable for the cylindrical hole at high blowing ratios and least noticeable for the laidback fan-shaped hole, which only displayed dependence on the coolant Mach number when the blowing ratio was 1.5. As long as the blowing ratio was high enough, all three hole shapes displayed higher film cooling effectiveness at the higher coolant Mach number. However, the cylindrical hole experienced less separation and higher η with perpendicular coolant crossflow, while the shaped holes displayed the opposite trend, because the flow near the hole exit is heavily disturbed, reducing the performance of the diffuser.

Dees et al. [33] investigated the effect of internal coolant Reynolds number on the overall film cooling effectiveness by using an airfoil test piece with two internal cooling channels and no film cooling holes. Typically, increasing the Reynolds number will increase the convection heat transfer coefficient. The test piece was formed out of a castable epoxy resin with a Biot number of 0.6-1.4 at test conditions, which is reasonably well matched to typical engine Biot numbers. The cooling channel near the leading edge was a U-bend design, separated from the second cooling channel, a simple radial design, by a thin wall, as shown in Figure 2-11.

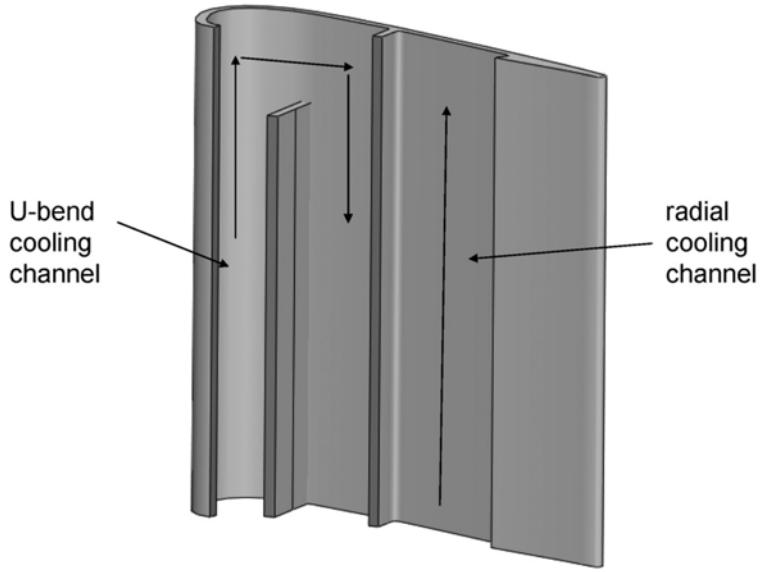

Figure 2-11: Dees et al. [33] test plate cutaway view

The tests were run at ambient conditions, with a freestream temperature of 300K and a coolant temperature of 250K. Tests were run with Reynolds numbers of 10,000 and 20,000 in both internal channels. For these tests, Dees et al. found that ϕ increased by roughly 50% when the Reynolds number was doubled, from a peak value of 0.2 to 0.3. A test was then run with the U-bend Reynolds number at 40,000 and the radial channel Reynolds number at 20,000. In this test, the local ϕ over the U-bend increased as expected, but ϕ over the radial channel remained at about the same value as before. Dees et al. conclude that ϕ is dependent the local internal cooling scheme because of its effect on the local internal heat transfer coefficient.

2.4. **Conjugate Heat Transfer Effects**

As previously mentioned, ϕ is more useful than η for real-world applications, because it takes into account both the external and internal cooling effects present in a film cooling scheme. The internal cooling can have a large impact on the effectiveness of a scheme, as shown in the

previous section. The internal cooling scheme remains important even when film cooling is introduced into the equation, as will be discussed in this section.

Williams et al. [8] used two geometrically identical models, replicating the suction side of a turbine blade, to investigate the impact of internal cooling on ϕ. One model was constructed of low conductivity foam, which allowed the measurement of η, while the other model was constructed of Corian (a material created by DuPont) to measure ϕ at a Bi similar to that of a real engine. These models had the same internal cooling scheme, which consisted of a series of impingement jets. Film cooling is provided by a row of 14 cylindrical holes on the suction side of the turbine blade. Upon performing tests at multiple flow rates, $\overline{\eta}$ values performed as expected, dropping lower as I increased and the jets began to separate. In contrast, $\overline{\phi}$ values held steady and then actually increased as I rose to 1.69, at which point $\overline{\phi}$ plateaued. Figure 2-12 shows the results that display these trends in $\overline{\phi}$.

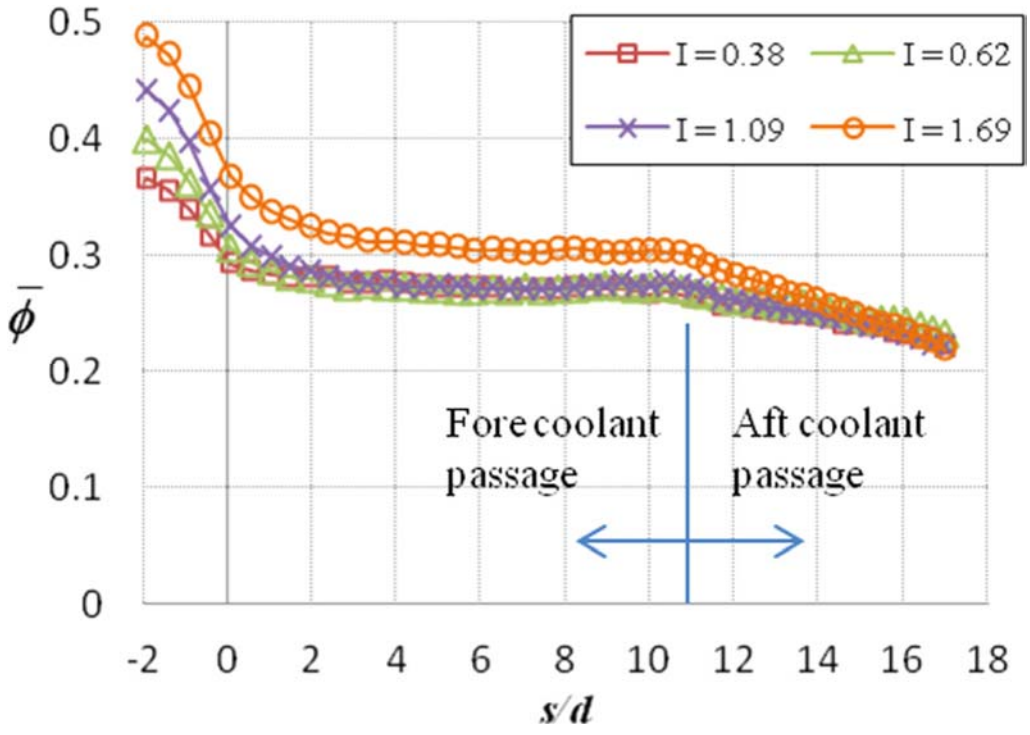

Figure 2-12: Data from Williams et al. [8]

While η and ϕ contours both indicated jet separation immediately downstream of the coolant holes as I increased, that same increase in I improved the cooling between the holes in the ϕ contours, indicating improved internal cooling. In general, the ϕ values were somewhat higher than the η values at high flow rates. Figure 2-13 shows η and ϕ contours for some selected momentum ratios.

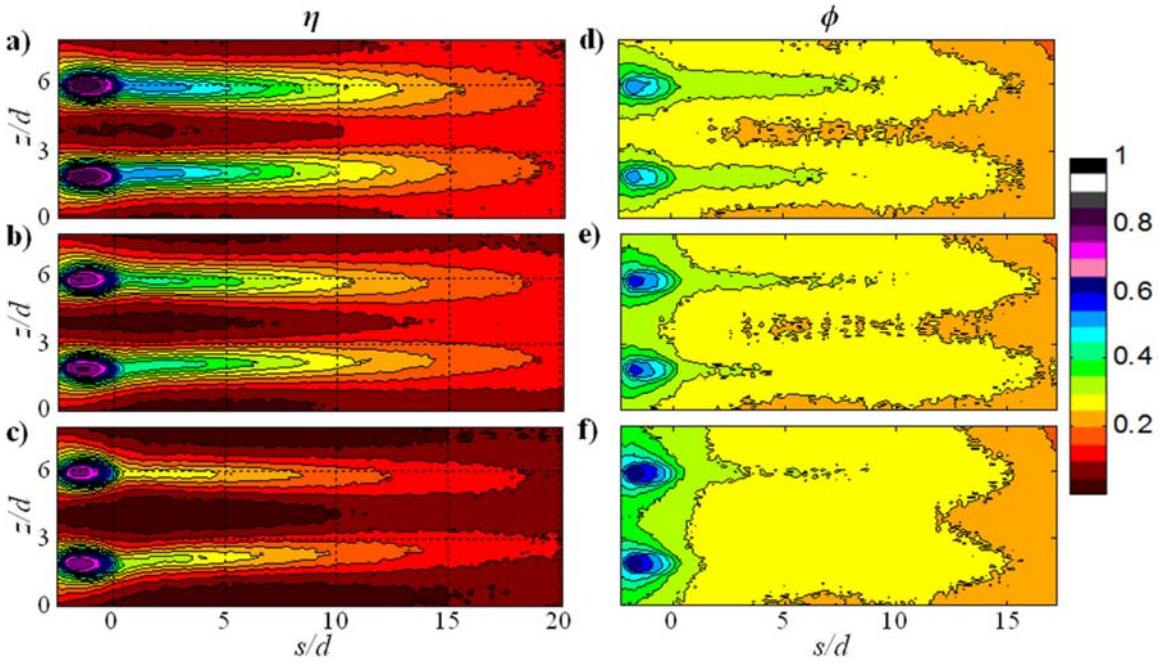

Figure 2-13: Contours of η for (a) I = 0.35 (b) I = 0.58 and (c) I = 1.03 and contours of ϕ for (d) I = 0.38, (e) I = 0.62 and (f) I = 1.09, dashed line denotes internal rib location (from Williams et al. [8])

Williams et al. [8] pointed out the notable spanwise variation in ϕ at the lowest flow rate, where I = 0.38, which would create correspondingly notable thermal gradients. Thermal gradients generally induce thermal stress, which can drastically reduce the lifetime of a turbine component. Williams et al. note that although the maximum spanwise variation was only 0.05, a variation of 0.02 can correspond to a temperature difference of up to 30K at real engine conditions, which can halve the operational life of a turbine component according to Bogard and Thole [4]. However, η

actually achieves its highest values at that same low flor rate, with $I = 0.35$. If η had been used as the sole metric to evaluate this scheme, it would have resulted in a scenario that severely reduced the operational life of the part.

Williams et al. [8] estimated the contribution of the internal cooling for their scheme by blocking two of the fourteen cooling holes on the model, which allowed an estimate of the overall cooling effectiveness without film cooling (ϕ_0) in that region. Spanwise variation was minimal, so the span-averaged overall effectiveness ($\overline{\phi_0}$) was used in further calculations. At the coolant flow rates that would have corresponded to $I = 0.38$ to $I = 1.11$, $\overline{\phi_0}$ held steady, but eventually rose from $\overline{\phi_0} = 0.22$ to 0.28 as the flow rate increased beyond the $I = 1.11$ level. A quick comparison of the peak value of $\overline{\phi_0}$ to the peak value of $\overline{\phi}$ (0.32) reveals that the impingement jets on the interior of the airfoil provide the majority of the cooling. Of course, this fact is most likely dependent on the internal cooling scheme and so may not be as pronounced in other applications.

2.5. Experimental Techniques

The measurement method used in film cooling experiments generally fall into one of two categories: thermal measurement methods and mass transfer measurement methods. Different methods have different advantages and disadvantages, depending on the desired parameter, spatial resolution, and flow conditions for the measurement. Mass transfer measurements rely on an analogy between heat and mass transfer. Some literature has questioned the accuracy of mass transfer methods, but they have been widely used nonetheless.

2.5.1. Thermal Measurement Methods

Thermal measurement methods have been used to find h, η, ϕ, Δq_r, and $\Delta\phi$. A large variety of thermal methods have been developed and employed, including thermocouples [34],

thermochromic liquid crystals (TLCs) [35], and infrared thermography [36]. In addition, both steady [37] and transient [36] infrared thermography techniques have been used. Alongside these methods, researchers have also used two different types of models: low-conductivity models and conductive models.

Low-conductivity models are used to approximate an adiabatic wall. With a few small assumptions, these models enable the measurement of T_{aw}, and thus η, using thermal methods. The most vital assumption for these applications is that any conduction through the model is purely one-dimensional [3]. This assumption allows for an easy correction to account for the small amount of conduction through the model. It is important to note that this assumption breaks down at the region near the hole, due lateral conduction in this region due to the coolant flow. Low-conductivity models are usually tested at near ambient conditions, because most of them are constructed from plastic [30] or foam [34], which melt at relatively low temperatures.

Conductive models are normally used to measure ϕ, since they readily conduct heat. These models can be used to represent engine conditions, since real engine surfaces experience substantial conduction. Albert and Bogard [9] is one example of such an application. They note that matching the Biot number is an important step in this process, as discussed in Section 2.1.2.

Thermal measurement methods may further be described based on the technique used to acquire thermal data. The earliest film cooling studies used thermocouples to measure the temperature, as demonstrated by Sinha et al. [34]. Although thermocouples are a sturdy option, they only provide temperature measurements at discrete points. To circumvent that difficulty, Sinha et al. employed thin ribbon thermocouples with several junctions at multiple locations, producing 60 data points. Even with so many measurements, they still could not reliably report the surface temperature at locations between the thermocouple junctions.

Ekkad et al. [35] painted their test piece with TLCs to get better spatial resolution for their experiments. TLCs shift in color depending on the temperature, so a CCD-RGB camera can be calibrated to determine the temperature based on the color of the applied paint. TLCs coat the entire surface, providing much better spatial resolution than thermocouples. Unfortunately, TLCs have a maximum operating temperature of only 100 degrees Celsius, which limits their applications [38]. Additionally, TLCs are sensitive to the lighting and camera angle, and the test plate must be painted black before the application of the TLCs, although a simple in situ calibration can account for these shortcomings.

The next development in thermal measurement methods, infrared (IR) thermography, relies on the radiative heat transfer of the test piece. IR measurements provide many advantages over TLCs, including a much greater operating range, less surface preparation, and a more direct measurement of the surface temperatures [36]. This investigation utilized IR thermography in its experiments, so this method will be expounded upon further in this section.

Although the spatial resolution of TLCs and IR thermography are useful, they require a clear line of sight to the test surface. Thermocouples simply need the space in the test piece to exist. TLCs require a window that is transparent in the visual range, but IR thermography requires a window of a material that will transmit infrared radiation, such as quartz [6], sapphire [25], sodium chloride [22], or zinc selenide [39].

Further difficulties with IR cameras may arise due to the highly complex nature of radiative heat transfer. For example, the net radiative heat flux emitted from a body depends on the emissive power of the body, reflected irradiation, absorbed irradiation, and, depending on the transparency of the body, transmitted radiation [10]. Thankfully, net radiative heat flux can be found as the difference in the radiation emitted from the surface ($q''_{rad,o}$) and incident on the surface, ($q''_{rad,i}$),

according to Greiner et al. [40]. It can be difficult to estimate $q''_{rad,i}$, because it depends on a wide variety of variables, such as geometry, emissivity, and temperature of surrounding surfaces. Greiner et al. discuss in detail a method to account for $q''_{rad,i}$ using empirical measurements of a given test rig.

Most surfaces have an emissivity (ε) that lies between 0 and 1 and reflect a fraction of the incident radiation according to $1 - \varepsilon_w$, if the surface is opaque and optically gray.

$$q''_{rad} = q''_{rad,o} - q''_{rad,i} = \varepsilon_w(\sigma T_w^4 - q''_{rad,i}) \tag{2-193}$$

This radiative process can apply to gases as well, not just solid objects [40]. In reactive film cooling cases, where flames and combustion are present, it becomes especially important to account for gases in the participating media. Since gases will emit light at specific wavelengths, radiation from participating media can be removed with optical filters. For example, this investigation used a 3900 nm bandpass filter to view a wavelength range that is free from the emission spectra of any potential participating gaseous media. However, these filters necessarily reduce the overall intensity of radiation that reaches the IR camera. In situ calibration methods, such as the one used in this investigation and described in Section 3.2.3, can empirically account for incident radiation and the dimming effect of optical filters.

IR thermography can be applied to a variety of tests cases, using different operating methods. Steady methods a commonly used to find η or ϕ by allowing the test surface to reach a stable temperature before IR data is recorded. Measuring the freestream and coolant temperatures in conjunction with the IR recording allows the calculation of the appropriate effectiveness metric. Albert and Bogard [9], Baldauf et al. [21], and Dittmar et al. [25] all measured η via IR thermography. Williams et al. [8], Lawson et al. [6] and Sweeney and Rhodes [39] all provide examples of steady state ϕ measurements.

Transient IR methods have been employed to measure heat transfer coefficient distributions. Ekkad et al. [36] simultaneously measured both η the heat transfer coefficient by starting with the model at a uniform surface temperature before rapidly increasing the freestream temperature. The test surface was modeled as a semi-infinite solid with transient conduction, with realistic film cooling boundary conditions to simplify the governing equation to:

$$\frac{T_w(t) - T_i}{T_f(t) - T_i} = 1 - \exp\left(\frac{h_f^2 \alpha t}{k^2}\right) \operatorname{erfc}\left(\frac{h_f \sqrt{\alpha t}}{k}\right) \tag{2-20}$$

where t represents time, the subscript i indicates the initial condition, and erfc is the error function [36]. Surface temperature measurements at two points in time can be used to create a system of equations that can be solved to find h and η everywhere on the test surface. The only downside of this very useful method is the need to quickly switch the freestream temperature between two steady states.

Lawson et al. [6] developed an infrared thermography method to account for radiation reflected off the test article and surroundings via an in situ calibration and post-test calibration with a blackbody radiation source. This method uses a modified form of the Stefan-Boltzmann Law, to calculate temperatures based on measured radiation intensity:

$$T = m\mathcal{I}^e + b \tag{2-21}$$

where $\mathcal{I}$ is measured radiation intensity from the test article and m, e, and b are constants calculated from the blackbody calibration. A specialized chamber enabled the measurement of the test piece reflectivity. The emissivity of the test piece was then calculated by subtracting the reflectivity from unity.

The radiosity observed by the camera, expressed in Eq. (2-22) [6], includes both radiation emitted by the test plate and incident radiation from the surroundings reflected by the test plate.

$$\mathcal{J}_{cam} = \varepsilon \mathcal{J}_w + \rho \mathcal{J}_{sur} \tag{2-22}$$

where ρ is the reflectivity of the test specimen and the subscripts cam and sur refer to the radiation observed by the camera and incident from the surroundings. Once the incident radiation was determined using special reflective markers and the radiosity measured by the camera, Eq. (2-22) could be solved for the radiation emitted by the test plate, $\mathcal{J}_w$. Finally, this value can be used with the measured constants and Eq. (2-21) to calculate the surface temperatures. Although more accurate than traditional calibration methods, this method requires a substantial amount of specialized equipment and time.

2.5.2. Heat-Mass Transfer Analogy

Before any discussion of mass transfer measurement methods, it is important to understand the heat-mass transfer analogy upon which those methods are based. The governing equations for heat and mass transfer share the same form. For comparison, Equations (2-43) and (2-54) show the heat transfer governing equation and appropriate film cooling boundary conditions, while Equations (2-65) and (2-76) show the mass transfer governing equation and the appropriate film cooling boundary conditions [10]. These equations assume non-reacting flow.

$$u^* \frac{\partial T^*}{\partial x^*} + v^* \frac{\partial T^*}{\partial y^*} = \frac{1}{Re_L Pr} \frac{\partial^2 T^*}{\partial y^{*2}} \tag{2-43}$$

$$T^*(x^*, 0) = 0, T^*(x^*, \infty) = 1 \tag{2-54}$$

$$u^* \frac{\partial C_A^*}{\partial x^*} + v^* \frac{\partial C_A^*}{\partial y^*} = \frac{1}{Re_L Sc} \frac{\partial^2 C_A^*}{\partial y^{*2}} \tag{2-65}$$

$$C_A^*(x^*, 0) = 0, C_A^*(x^*, \infty) = 1 \tag{2-76}$$

where Sc is the Schmidt number ($\mu/\rho D_A$), D_A is a mass diffusion coefficient for species A, C represents species concentration, the subscript A represents a given species, and the superscript asterisks ($*$) indicate that the variables are nondimensional. If the nondimensional parameters and

boundary conditions are matched, the results of both equations should be identical, since their forms are identical. This concept is widely employed in fluid dynamics to account for differences in physical geometry or flow conditions, but in this case it allows different testing methods.

This analogy is particularly useful for studies that seek to quantify the adiabatic effectiveness for a given film cooling scheme. As discussed previously, no material is truly adiabatic, so thermal methods will always have to apply a correction for the conduction through the wall. However, mass will not diffuse through the solid wall, so a mass transfer measurement that uses the heat-mass transfer analogy can eliminate any conduction error, potentially allowing for more accurate assessment of the adiabatic film cooling effectiveness.

On the other hand, mass transfer methods ignore thermophysical properties such as c_p and k. Mass transfer properties, such as the mass diffusion coefficient (D_A) replace the thermophysical properties. This substitution could introduce new problems. Goldstein and Cho [41] point out the governing equations for heat and mass transfer should only be considered equivalent as long as the sum of the Lewis number is unity. The Lewis number describes the relationship between energy and mass diffusion and can be calculated:

$$Le = \frac{Pr}{Sc} \tag{2-87}$$

If the Lewis number is unity, heat and mass both diffuse identically. Amongst the numerous studies that rely on these assumptions, very few have examined them. Nicoll and Whitelaw [42] noted that existing work at the time supported the assumption of a unity Lewis number for many cases. Section 2.5.4 explores this topic a bit further by comparing heat and mass transfer measurements.

2.5.3. Mass Transfer Measurement Methods

Mass transfer measurements have been heavily employed to measure h and η. Examples of mass transfer methods include gas chromatography [42], naphthalene sublimation [41], and Pressure Sensitive Paint (PSP) [15]

Nicoll and Whitelaw [42] used a gas chromatography method in the early days of film cooling research to measure impervious wall effectiveness, which is equivalent to adiabatic effectiveness if the heat-mass transfer analogy from Section 2.5.2 can be taken as true. Coolant containing 1% helium by volume as a tracer was injected through a single slot parallel to the test surface. Samples of the flow at the test surface were captured downstream of the injection slot and stored for analysis via gas chromatography. The impervious wall effectiveness was then calculated at the sampling points by comparing the concentration of helium there to the concentration at a downstream location. Since this technique requires discrete sampling ports, it suffers from the same lack of spatial resolution as thermocouples, as well as disturbing the flow.

The naphthalene sublimation method produced better spatial resolution. When a test piece is coated in naphthalene and exposed to the freestream flow, the layer of naphthalene on the surface sublimates into the freestream [41]. Mass transfer coefficients can be calculated from the amount of naphthalene sublimation. Using the heat-mass transfer analogy, the equivalent to heat transfer coefficients can be found from the mass transfer coefficients. Precisely measuring the change in naphthalene thickness any given point can provide local mass transfer coefficient. Although this method can produce accurate measurements of the mass transfer coefficient distributions and provide good control of the boundary conditions, it has a variety of limitations. These include the involved process of using a mold to coat the surface in a uniform thickness of naphthalene, run times of up to two hours, and the basic change in shape that the test piece experiences as the

naphthalene sublimates [41]. Additionally, the slow sublimation of the naphthalene precludes any kind of transient testing, and the potential for erosion of the naphthalene coating prohibits any flowfields with high velocity or shear.

The PSP method avoids the limitations of naphthalene sublimation while still providing high spatial resolution, as detailed by Crafton et al. [43]. PSP can be used for both steady state and transient applications, with a measurement response of up to 100 kHz. Unlike naphthalene, the PSP paint is applied to the surface once and stays there, so the test piece does not change shape over time. The pitfalls of the PSP method are its temperature dependence, sensitivity to illumination uniformity and stray light, paint photo-degradation, poor signal-to-noise ratios in low velocity flows, excessive camera shot noise, and model displacement or deformation. Luckily, many strategies to overcome these issues have been generated by the extensive amount of research performed with PSP.

PSP consists of luminescent molecules (luminophores) suspended within an oxygen permeable polymer. These luminophores can be excited by a specific wavelength of light (405 nm is commonly used) [43]. When the luminophores return to their unexcited state, they emit photons of different wavelength than the excitation light. The key is that these luminophores can also return to their relaxed state without emitting a photon, if oxygen is present. This process is known as oxygen quenching. Essentially, at higher partial pressure of oxygen, more luminophores experience oxygen quenching, reducing the overall output of light. Therefore, the PSP displays the distribution of oxygen over the surface, with more oxygen at darker points. A coolant gas with little or no O_2 in it will therefore cause darker regions where it prevents the relatively oxygen-rich freestream from reaching the surface. Of course, other factors can influence the luminescent intensity, such as the illumination intensity, paint thickness, and luminophore concentration. By

comparing the luminescent intensity at an unknown condition to intensity at a known reference condition, these other factors can be accounted for. This approach, called the radiometric PSP method, relies on a modified form of the Stern-Volmer equation [43]

$$\frac{\mathcal{I}_0}{\mathcal{I}} = A(T) + B(T)\frac{P}{P_0} \tag{2-28}$$

where $\mathcal{I}$ is emitted light intensity, A and B are constants, and the subscript 0 refers to a reference condition. Using this equation, the paint's dependence on temperature and pressure can be determined, and the PSP calibrated.

Binary PSP attempts to account for the temperature dependence of luminophores by using two different types of luminophores excited by the same wavelength of light. One of these types is sensitive to both temperature and pressure, while the other is only sensitive to temperature [43]. The pressure and temperature sensitive luminophore is called the signal probe, and the temperature sensitive, pressure insensitive luminophore is called the reference probe. The two luminophore types emit different wavelengths of light, so two separate images can be collected at any given test condition. Figure 2-14 from Wiese et al. [18] illustrates the difference between a single component and binary PSP. In Figure 2-14, the signal probe emission is referred to as sensitive.

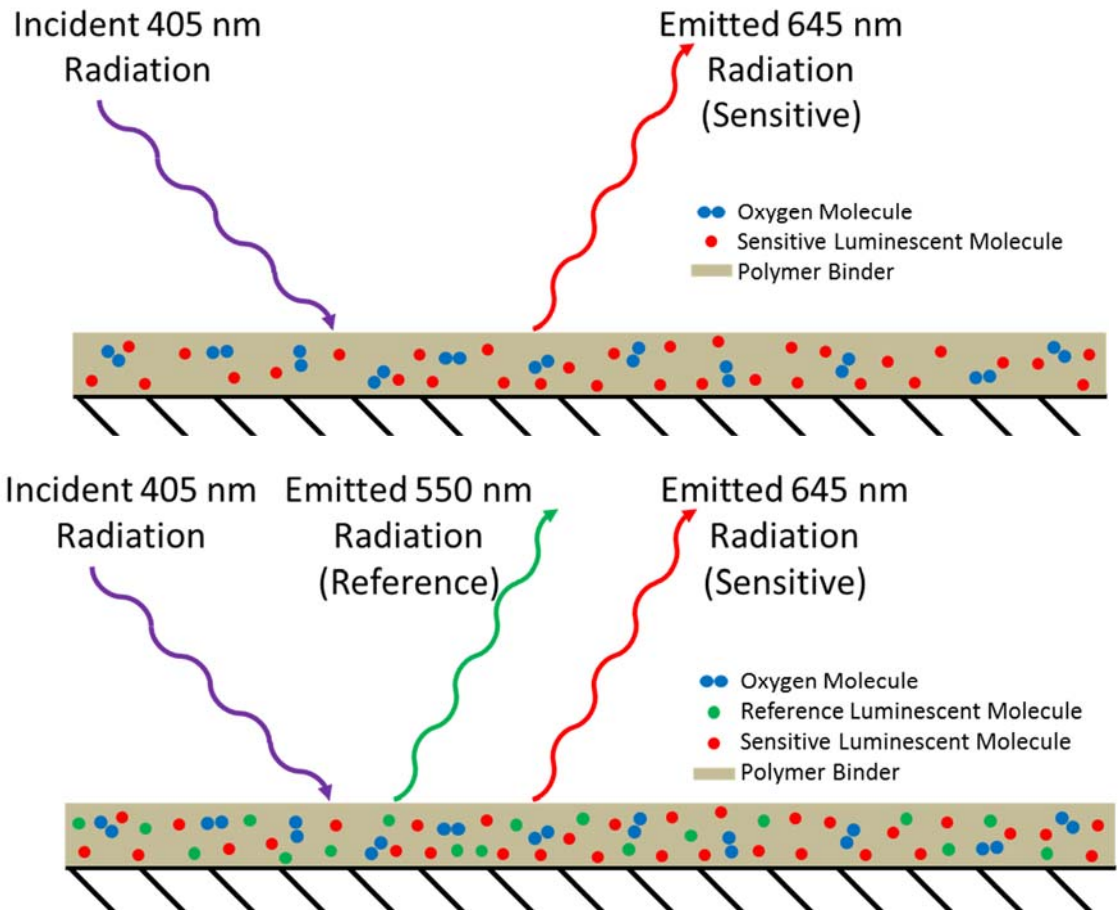

Figure 2-14: Comparison of single component and binary PSP (image from Wiese [18])

Illumination intensity effects can be removed using a ratio of the responses of the reference and signal readings [43]

$$R(P,T,n_S,n_R) = \frac{F_S(P,T)n_S\mathcal{I}}{F_R(P,T)n_R\mathcal{I}} = \frac{F_S(P,T)n_S}{F_R(P,T)n_R} \tag{2-29}$$

where R is the signal to reference ratio, F is the individual luminophore response, n is the number density for the luminophores, $\mathcal{I}$ is local illumination intensity, and the subscripts S and R refer to the signal and reference probes. Additionally, the luminophore density effects can be removed with a ratio of the signal to reference ratios between an unknown condition and a known condition [43]. Equation 2-30 provides the relevant terms.

$$S(P,T) = \frac{R_0(P_0,T_0)\frac{n_S}{n_R}}{R(P,T)\frac{n_S}{n_R}} = \frac{R_0(P_0,T_0)}{R(P,T)} \tag{2-30}$$

where S is the system response and the 0 subscript denotes the known condition. In addition to allowing the removal of illumination intensity effects, the reference probe helps minimize temperature dependence. Since the two types of luminophores emit different wavelengths, the temperature effects at a given pressure can be accounted for within the calibration. By performing multiple calibrations at different temperatures, a master calibration can be created to account for temperature effects [43]. Innovative Scientific Solutions, Inc. produces a binary PSP that has a temperature sensitivity of less than ~50 Pa/K over temperature and pressure ranges spanning from 283K to 313K and from 10kPa to 160kPa respectively. Temperature variation in the paint can potentially be mitigated by various means, such as a highly conductive model [43]. Once the pained model is calibrated and in place, the CCD camera that is used for testing can be easily calibrated by recording the intensity at a known pressure and correcting via the known paint properties. In practical applications with ISSI equipment, the camera correction takes place automatically during post-processing.

Although binary PSP method eliminates illumination issues and reduces temperature sensitivity, it doubles the impact of camera shot noise thanks to the four images needed in Eq. (2-30), as opposed to the two images required for single component PSP [43]. PSP also degrades with exposure to light of the excitation wavelength. Exposure to light must be limited via dark storage and limited duration testing. A sturdy, stationary model can help reduce model displacement and deformation effect, but if the model does shift or deform, it can prove troublesome to correct in post-processing.

Thanks to the heat-mass transfer analogy, η can be represented as the concentration of oxygen for PSP when the freestream is normal air [15]

$$\eta = \frac{T_\infty - T_{aw}}{T_\infty - T_c} \approx \frac{C_\infty - C_w}{C_\infty - C_c} = 1 - \frac{C_{O_2,mix}}{C_{O_2,air}} \tag{2-91}$$

where the O_2 subscript indicates oxygen and the subscripts mix and air represent cases where the coolant is either foreign gas (devoid of oxygen) or air, respectively. To clarify, you would run two separate tests at the same conditions, once with air as the coolant and once with the foreign gas as the coolant. Eq. (2-91) allows you to find the adiabatic effectiveness by comparing the O_2 concentration at a given point for both cases. That equation can also be rewritten by relating the concentration of oxygen to the partial pressure of oxygen through mole fractions and molecular weights, producing [15]

$$\eta = 1 - \frac{1}{\left(\frac{P_{O_2,air}}{P_{O_2,mix}} - 1\right)\frac{MW_{fg}}{MW_{air}} + 1} \tag{2-102}$$

where P_{O_2} represents the partial pressure of oxygen, MW represents molecular weight, and the subscripts fg and air represent a foreign gas and air, respectively. The oxygen-free foreign gas prevents the oxygen quenching reaction by displacing oxygen near the test surface, thus increasing the observed light intensity from the PSP.

A sequence of images is collected for both the foreign gas and air injection cases to generate a pressure field [15]. A reference image, called the "wind off" case, is collected with excitation illumination, no freestream flow, and no coolant flow. The "wind on" image, or experimental condition, is collected with excitation illumination, freestream flow, and coolant flow. To use Eq. (2-102), a wind on image must be collected for both air and foreign gas injection. A dark image, or background image, is captured with no flow and no illumination. Subtracting the background

image from the wind on images accounts for any stray ambient light in the test setup, as displayed in Eq. (2-113).

$$\frac{\mathcal{I}_0 - \mathcal{I}_b}{\mathcal{I} - \mathcal{I}_b} = f\left(\frac{P_{O_2}}{P_{O_2,0}}\right) \tag{2-113}$$

where the subscript b refers to the background image. In concert with the calibration process discussed above, this method enables the accurate calculation of the oxygen partial pressure distribution across the surface.

2.5.4. Comparison of IR and PSP Measurement Methods

In general, PSP methods demonstrate the same experimental trends as thermal methods. Han and Rallabandi [44] conducted a thorough PSP gas turbine literature. PSP methods confirm many of the trends discussed in preceding sections, such as jet separation with increases coolant flow, reduced separation with shaped holes, the negative impact of freestream turbulence, etc. However, direct comparison of measured η values reveals some discrepancies between IR thermography and PSP methods.

Wright et al. [38] directly compared IR thermography and PSP by using both methods to evaluate the adiabatic effectiveness of a specific cooling scheme. The scheme had seven cylindrical cooling holes with diameter d = 4 mm, pitch spacing P/d = 3, and α = 30 degrees with a 45 degree compound angle in a flat plexi-glass test specimen. The IR measurements used air heated to 43.3 °C for coolant (DR = 0.93), while the PSP measurements used nitrogen gas at room temperature (DR = 0.97). The measured $\bar{\eta}$ values for both methods were then compared at M = 0.6 and 1.2. The IR method showed higher values of $\bar{\eta}$ than the PSP method when M = 0.6, but both methods were in reasonably good agreement at the higher blowing ratio, except near the hole. The PSP data suggests that the jet detached from the surface near the hole at both blowing ratios and

then reattached further downstream. This phenomena occurred even at the lower blowing ratio, which corresponds to I = 0.58 and would not be expected to experience separation. The IR data does not show any evidence of separation.

Wiese et al. [18] performed a similar experiment, but observed quite different trends. Their model consisted of a semi-cylinder followed by a flat afterbody. A single row of cooling holes with a diameter of d = 5.08 mm, a coolant injection angle of α = 20 degrees, and a compound angle of 90 degrees were positioned partway up on the cylindrical leading edge at an angle of γ = 21.5 degrees from the centerline. Nitrogen, argon, and carbon dioxide were used as coolant gases for both IR and PSP tests at identical temperature conditions (T_c = 295 K, T_∞ = 315 K). Tests were controlled via the momentum flux ratio, set to I = 0.5 and 1.0. Measured η values collected spanwise at x/d = 5 via both methods were then compared. In this study, the PSP method produced consistently higher η values than the IR method. However, the PSP method still suggested flow phenomena that were not observed in the IR thermography results, such as bifurcated coolant jets. Wiese et al. suggest that low turbulence levels might have resulted in a non-unity total Lewis number, which could have allowed energy diffusion to be greater than mass diffusion, invalidating the heat-mass transfer analogy. The nature of PSP as an oxygen sensor was also cited as a potential cause for these elevated effectiveness values, as energy may have diffused through the flow via molecular collisions to warm the surface while the physical mass (oxygen) may not have diffused to the surface. This would cause elevated intensity for the PSP tests and produce inflated η values.

It is difficult to compare results between the studies of Wright et al. [38] and Wiese et al. [18], as they have different experimental setups and present their results differently. Therefore, no clear conclusions can necessarily be drawn regarding the relative accuracy of the two methods. It

is important to keep in mind the advantages and limitations of both methods when determining which method best suits a given test setup.

3. Experimental Methods

This investigation utilized the Film Cooling Rig (FCR) in the Combustion Optimization and Analysis Laser Laboratory (COAL Lab) located at the Air Force Institute of Technology (AFIT). The AFIT FCR was designed by Shewhart [45] and Lynch [19], then constructed and tested by Lynch, who provides a detailed description of the rig in his thesis [19]. Since those first experiments, additional testing methods have been explored by Ashby [2] to tackle film cooling investigations in both high and low temperature regimes, via both IR and PSP test methods. As mentioned in Section 1.2.1, multiple modifications were made to the FCR to attempt to address issues that were encountered during previous investigations.

Section 3.1 discusses the FCR itself, with subsections on the Well-Stirred Reactor (WSR), the test section, and the cooling block assembly. Section 3.2 discusses the variety of other equipment required to support the FCR, including various temperature and mass control devices, PSP testing equipment, and IR camera equipment. Section 3.3 provides an overview of the data acquisition tools used for this investigation, as well as the PSP and IR thermography setups that were employed. Finally, Section 3.4 discusses the uncertainty of the data collected for this investigation.

To function as an experimental apparatus, the FCR relies on a variety of other laboratory equipment, such as mass flow controllers, IR and PSP measurement hardware, and user interface software, amongst other things. Additionally, the gathered data must be processed and analyzed using appropriate methods. All of these topics will be discussed in the following sections.

3.1. Film Cooling Rig

A brief outline of the AFIT FCR will be presented in this section. The key components of the FCR are the Well-Stirred Reactor (WSR), the transition section, the test section, and the airfoil test plate, all of which are shown in Figure 3-1.

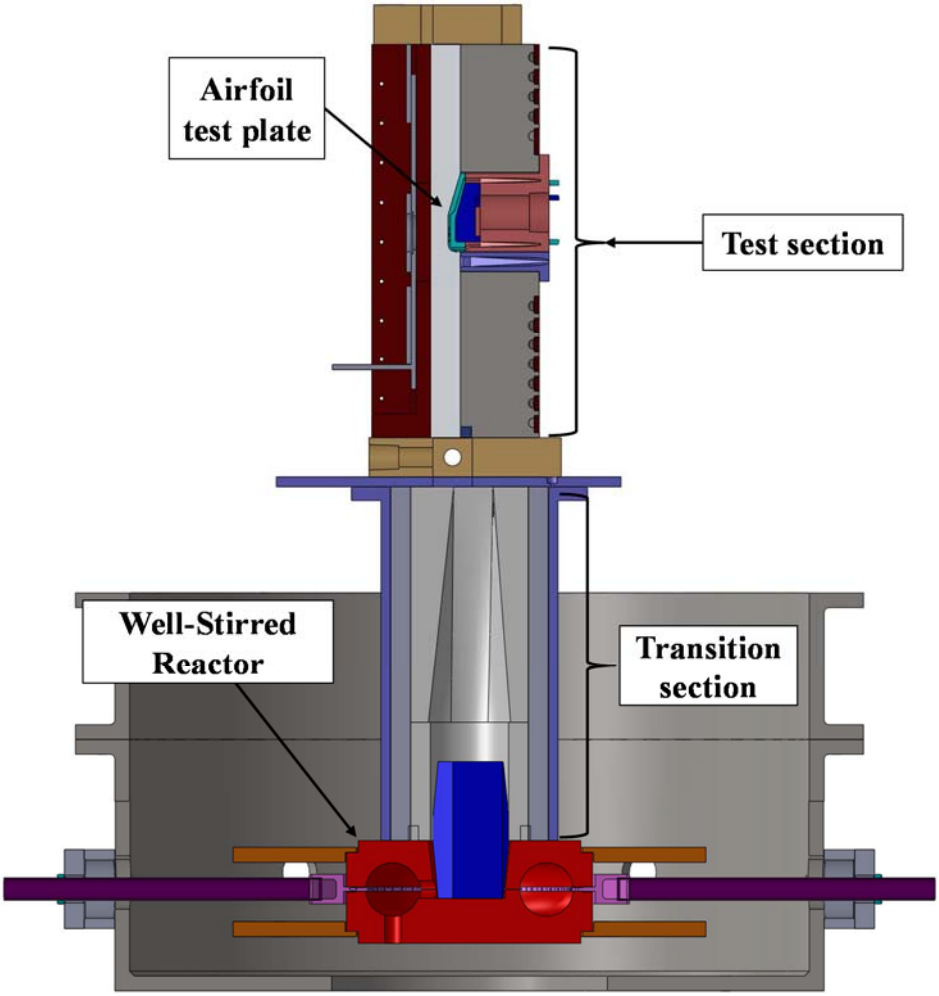

Figure 3-1: AFIT Film Cooling Rig and Well-Stirred Reactor cross-section (image adapted from Ashby [2])

The FCR design enables the testing of different film cooling schemes at a wide variety of conditions. Burning within the WSR enables the freestream to reach near engine temperatures,

while near ambient tests can be performed without burning in the WSR using other COAL Lab equipment to control the gas temperature. The transition section straightens the flow and adjusts it to the rectangular cross-section of the test area, which has multiple interchangeable test plates and optical access options.

3.1.1. Well-Stirred Reactor

The Well-Stirred Reactor (WSR) supplied the FCR with high-temperature combustion products to more accurately simulate the conditions within a turbine engine. The WSR was based on the design of Nenniger et al. [46] with modifications by Stouffer et al. [47]. Figure 3-2 shows both a conceptual and exploded view of the WSR assembly. The WSR was a toroidal reactor, with a jet ring manifold sandwiched between the two toroid halves made from Inconel 625 alloy. Two large steel plates served as a clamp, held by bolts that used springs to force the plates together without causing large thermal stresses when the WSR expands at high temperature.

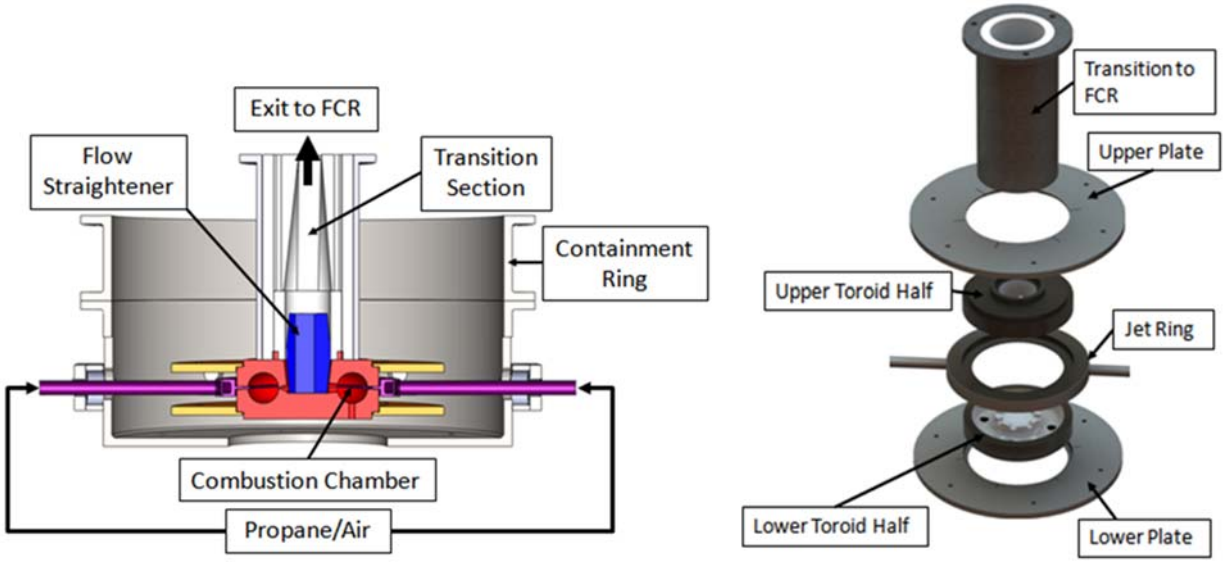

(a) **(b)**

Figure 3-2: AFIT Well-Stirred Reactor diagrams: (a) side view cross-section and (b) exploded view (images from Lynch [19])

The 250 mL toroidal combustion chamber was fed with premixed air and propane at a controlled equivalence ratio through the jet ring. Propane was fed from four 120 gallon compressed liquid propane tanks stored in the tank farm, alongside the alternative coolant gases. Two Zimmer propane vaporizers ensured the propane was gaseous before it entered the WSR. A cylinder of ethylene in the tank farm fed the ethylene-air spark ignitor used in the WSR.

Once the air-fuel mixture combusted, the combustion products exited the combustion chamber through eight holes around the inner edge of the toroid. A flow straightener removed swirl from the flow as it made its way to the ceramic transition section. The transition section gradually sloped from the 20.27 cm^2 circular WSR exit area to the 12.90 mm^2 rectangular FCR entrance area.

As shown in Figure 3-3, the transition section had multiple ceramic parts housed within a steel chimney. The change in cross section is done by six 2.54 cm (1.0 inch) thick ceramic discs machined to gradually shift from the circular WSR exit to the rectangular FCR inlet. The seventh piece, a 7.62 cm (3.0 inch) long ceramic cylinder, provided space for the flow straightener at the bottom of the transition section. In addition to housing the ceramics, the steel chimney supported the weight of the test section, which mounted to the transition plate atop the chimney.

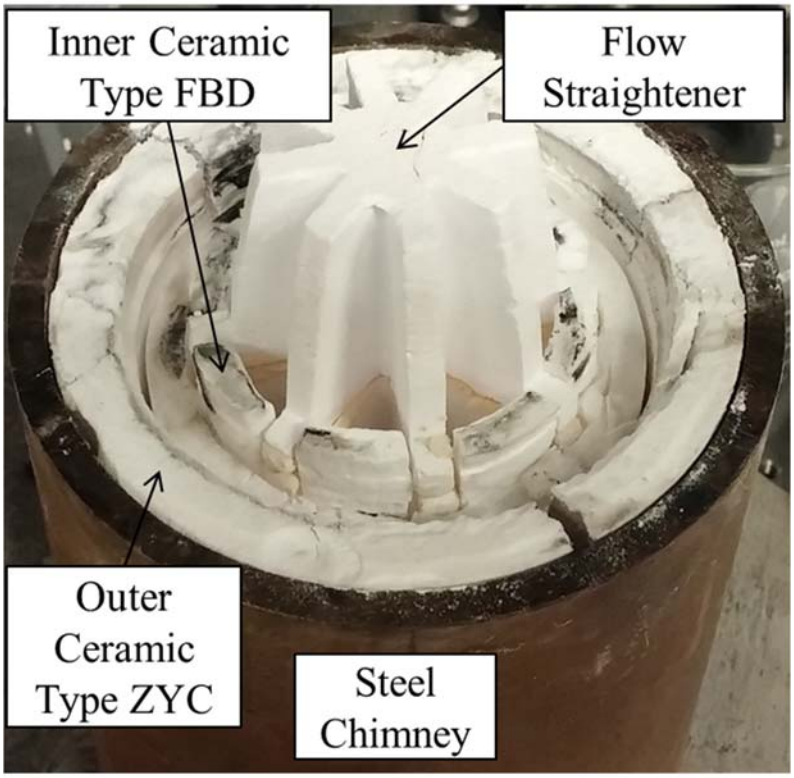

Figure 3-3: Inverted view of WSR transition section (figure from Ashby [2])

The inner wall was formed from seven Type FBD zirconia ceramics, chosen for its relative resistance to mechanical erosion from the flow. Unfortunately, this type of ceramic is relatively brittle, and thus experiences cracking under thermal stresses and shocks. To mitigate this downside, the ceramics were surrounded by an outer layer of Type ZYC zirconia ceramic, which is softer. Since the outer layer was not exposed to flow, it was not vulnerable to erosion. This layering method helped ensure total protection of the steel chimney from excessive temperatures. Both of the zirconia ceramic used for these parts were supplied by Zircar Zirconia, Inc. The flow straightener was molded out of alumina ceramic by technicians at AFRL/RQTC.

Figure 3-4 shows an example of the kind of failure that can occur, due to the fragility of the ceramics. This set of ceramics had been used for many tests prior to the test of this investigation. Two chunks of the ceramic broke off from the wall and came to rest on top of the flow straightener, partially blocking the freestream flow. Since disassembling the rig to replace the

ceramics would have been extremely time-consuming, an interim solution was devised using Ceramabond (a high-temperature ceramic paste) to patch a portion of the ceramics. This quick fix held through multiple subsequent ignition cycles and low-temperature tests, suggesting that it could be used in the future to prolong the operational life of these expensive ceramic components.

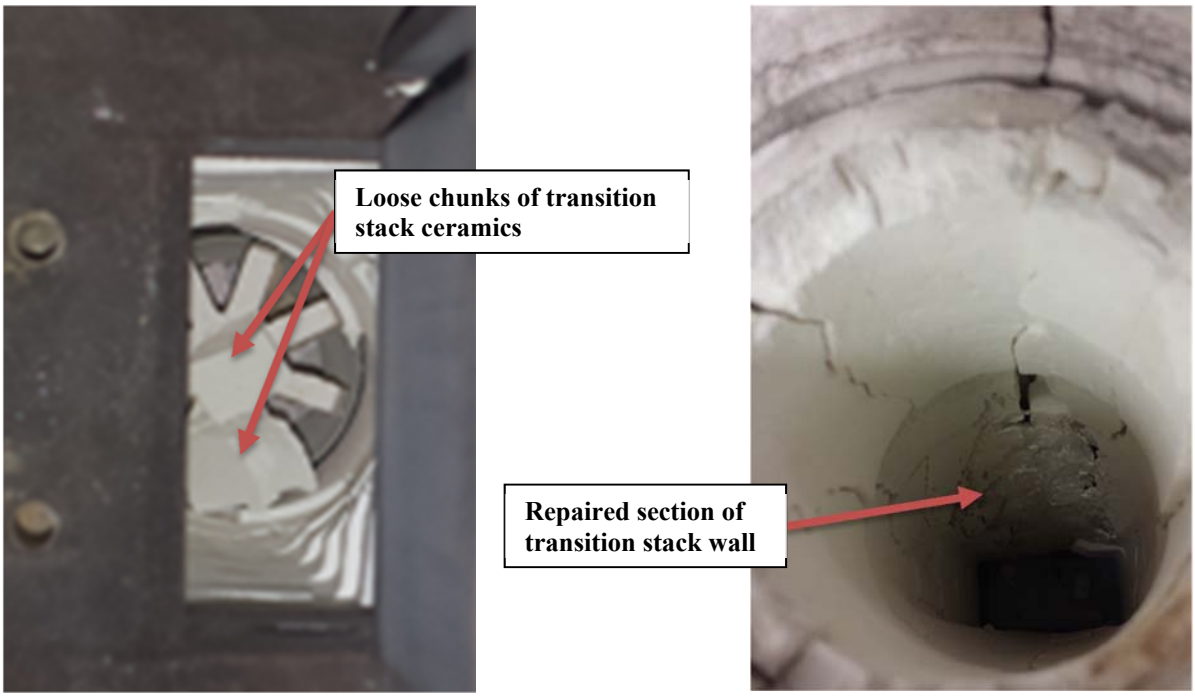

Figure 3-4: Dislodged ceramic (left) and Ceramabond repair (right)

The WSR has many other features focused on instrumentation and managing the high temperatures of combustion. Figure 3-5 shows the interior of the upper and lower toroid halves and jet ring that form the combustion chamber. Two of the four ports on the lower toroid were used. The first fit the igniter, which used a sparkplug to initiate an air-ethylene ignition flame. The second fit a B-type thermocouple, which provided measurements of the temperature in the combustion chamber. Mica gaskets ensured a good seal between the jet ring and both toroid halves. A Thermal Barrier Coating (TBC) of yttria-stabilized zirconia ceramic protected the interior

surface of the toroid halves from the extreme heat. Coolant water channels were machined into the toroid halves to cool the WSR.

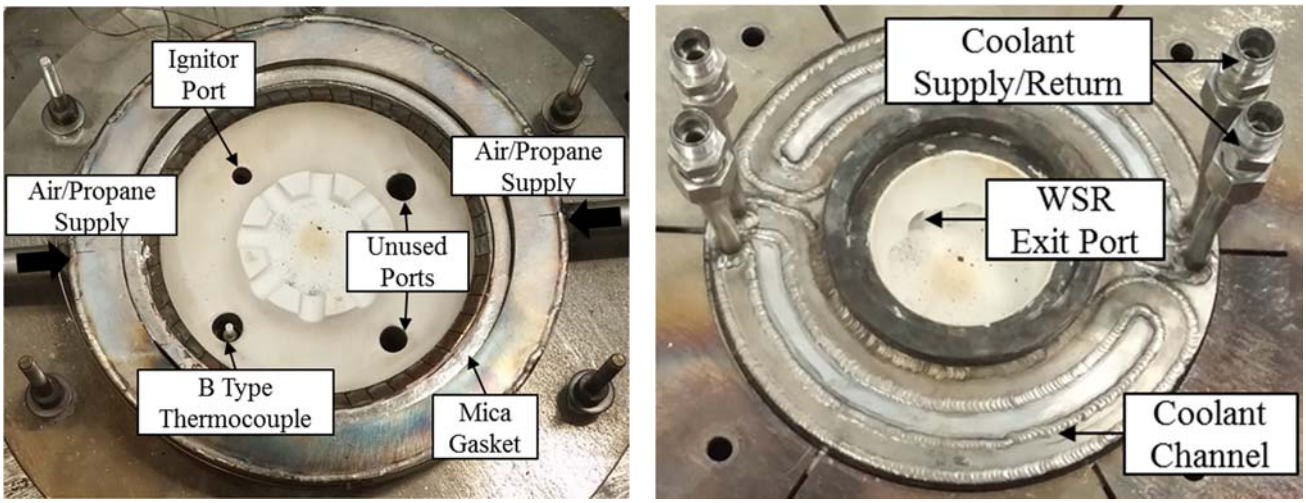

Figure 3-5: AFIT Well-Stirred Reactor: (a) lower toroid and jet ring and (b) upper toroid (figure from Ashby [2])

One of the first adjustments that had to be made to the FCR was a repair to some damage sustained by the TBC during previous testing by Ashby [2]. One of the water coolant lines in the WSR became blocked by debris that is suspected to have come from the chilled water lines that feed them. This blockage occurred during high temperature testing, so the WSR overheated, causing excessive thermal expansion that damaged the TBC, as shown in Figure 3-6. Luckily, the damage occurred to the upper toroid half, which is more easily removed and transported via full disassembly of the rig. Ellison Surface Technologies, Inc. applied the new ceramic coating, which was the same yttria-stabilized zirconia as had been used previously. To prevent this sort of setback from reoccurring, a filter, also shown in Figure 3-6, was installed on the coolant water supply line, courtesy of the AFIT lab techs.

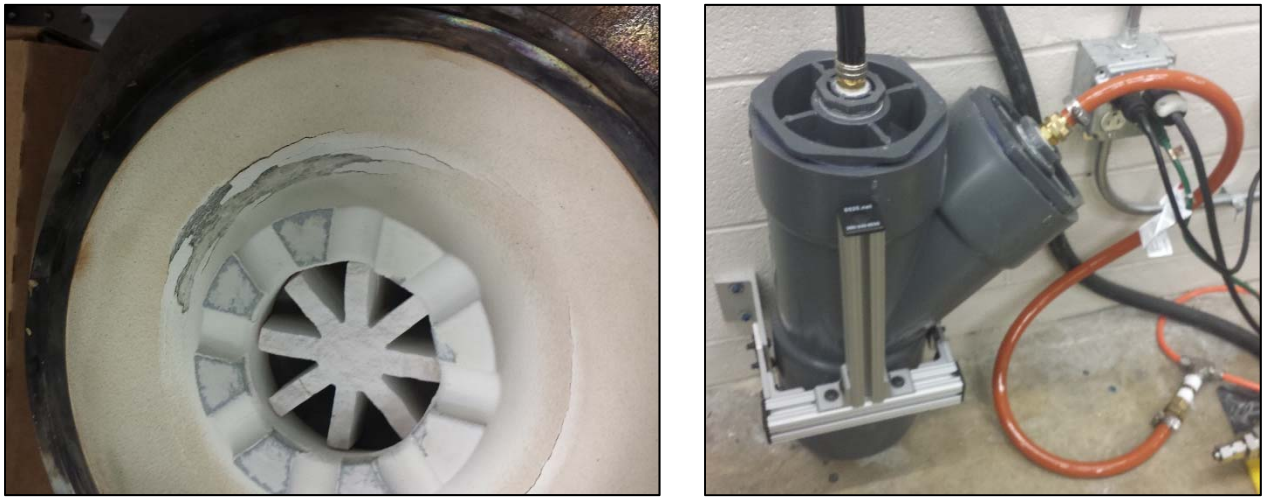

a) b)

Figure 3-6: a) TBC damage on upper toroid half b) New WSR coolant water filter

Unfortunately, the same thermal expansion that damaged the TBC also weakened the welds on the coolant water supply channels in the upper toroid. After cycling through multiple WSR ignitions and high temperature tests, the welds finally gave way, leaking coolant water into the transition section and toroid. Once the rig was disassembled, the welds were repaired by the AFIT Model Shop. Figure 3-7 shows the repaired welds. That figure also shows discolorations that appeared on the inner surface of the toroid. It is hypothesized that these marks arose from the combustion of propylene glycol antifreeze in the coolant water that leaked into the toroid.

Figure 3-7: Location of repaired water coolant channel welds (top) Discoloration from cooling water leak (Bottom)

The WSR possesses a wide operating range. It has been successfully operated for various investigations at equivalence ratios of 0.68 – 1.3. The toroid has withstood operating temperatures as high as 1800K, resulting in a maximum test section temperatures in excess of 1600K. The bulk of tests have been performed in the 1500K-1600K operating range [2] [19], but the tests for this investigation successfully operated at 1300 K. All of these freestream temperatures were recorded at freestream flow rates of 600-650 SLPM. Flow rates above 700 SLPM have caused blowout issues in prior studies, where the combustion reaction migrates from the toroid into the test section because of the high mass flow. In other cases, combustion ceased altogether. It was observed

during this investigation that low flow rates (~400 SLPM) would allow lower freestream temperatures (~1100K). In addition to this range, low temperature tests can be performed without burning in the WSR to reach freestream temperatures from ambient (~298K) to 420K, using a Gaumer Process 12.5 kW electric heater. The heater was limited to an exit temperature of around 600K due to safety considerations, but the freestream temperature was lower due to thermal losses between the heat and the test section.

During this investigation, a heater tape was tested in an attempt to increase the reliability and upper limit for freestream temperature without burning in the WSR. The model was an OMEGALUX STH051-080 model 627 W ultra-high temperature heater tape. It was applied by wrapping it around the air feed lines, as shown in Figure 3-8. It was then surrounded with fiberglass insulation. Unfortunately, the tape did not have a control device and exceeded expected temperatures, melting some of the insulation. Although technically successful, different insulation would be required to employ these devices in the future.

Figure 3-8: a) Heater tape and b) melted insulation

3.1.2. Test Section

The FCR is oriented vertically, with the test section supported by the steel housing of the transition section that sits on the WSR. The FCR is stabilized by four threaded rods, which prevent

toppling. A total of four bolts affix the front and back plates of the test section to the base plate, while the side plates simply slide into place between them. In the front block, the bolts sit in slots instead of holes, so the distance between the blocks can be adjusted, if desired. To maintain a seal between the main block and baseplate, the bolts between those parts actually pass upwards through countersunk holes in the baseplate. The upper bracket helps keep the front, back, and side plates in place and consistently spaced. Figure 3-9 show these parts, with one of the side plates replaced by a clear window to provide a view of the test plate.

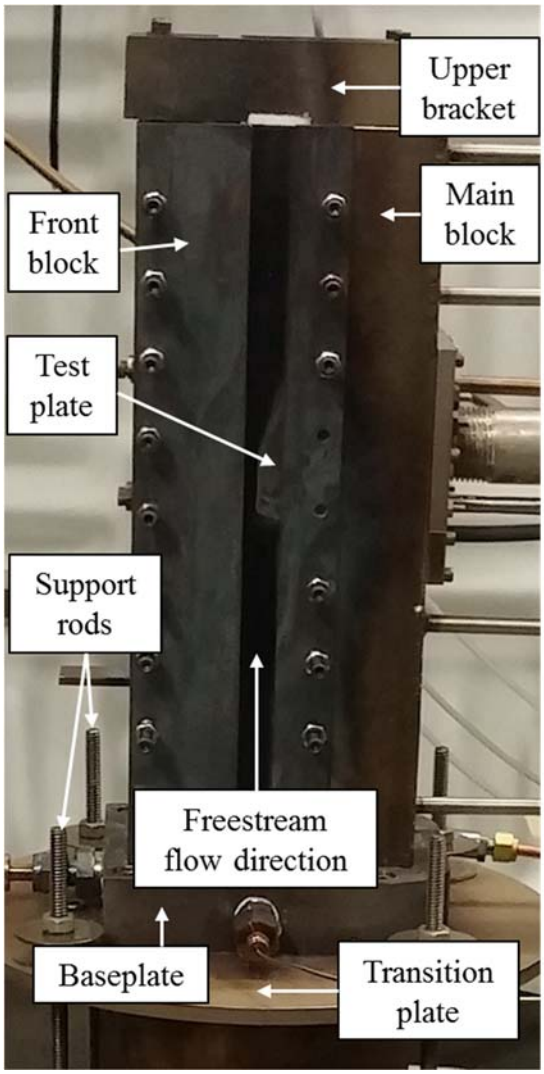

Figure 3-9: FCR side view (from Ashby [2])

The test section was supported by the steel chimney of the transition section and housed the cooling block assembly, which will be discussed in detail in the next section. The notable features of the test section are outlined in Figure 3-10. The figure is a cutaway view of the test section from the same angle as Figure 3-9, just rotated 90 degrees so that freestream flow is from left to right. For high temperature tests, a MOKON unit fed cooling oil at 422K through channels in the back block, preventing excessive thermal expansion. A boundary layer trip at the entrance of the test section ensured a consistent turbulent flow regime.

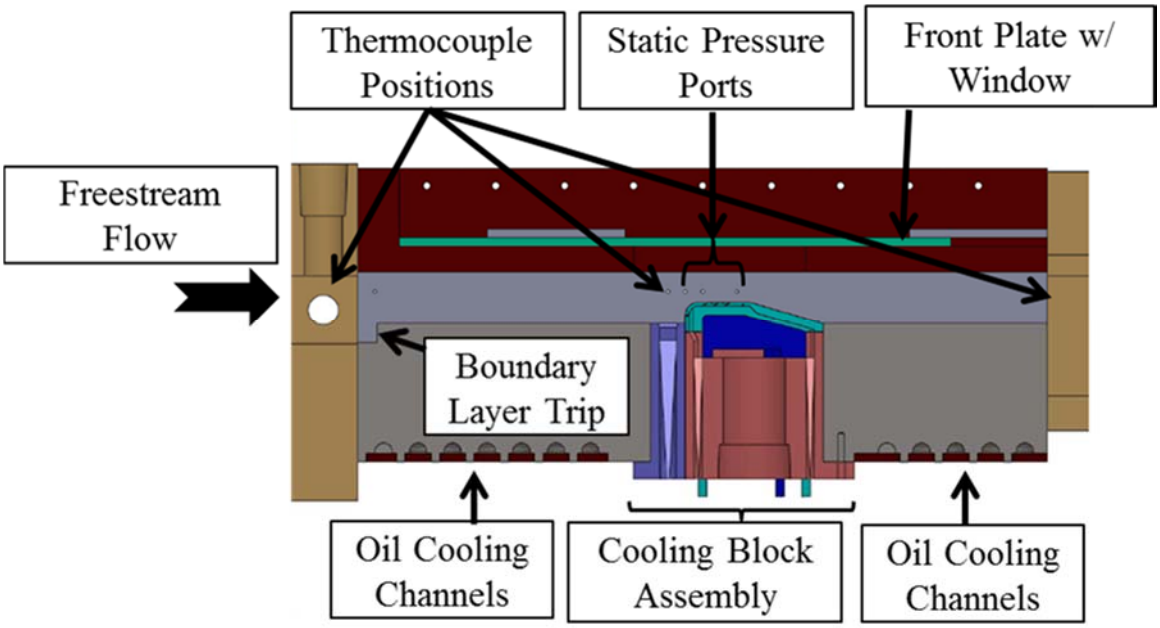

Figure 3-10: Test section cutaway view

The front plate of the test section was interchangeable, to allow for both optical and IR access options. A quartz window was used for optical access during PSP tests. The bulk of the IR data in this investigation was taken using a sapphire window. Over the course of testing, it was noticed that there was an IR "shadow" that appeared on the window. The shadow was hypothesized to be a reflection of the IR camera. For the bulk of testing, the front plate of the rig was shifted very slightly to angle the reflection away from the camera.

To investigate other methods of mitigating the reflection, Christian Schmiedel ran a series of tests on various other IR window options, including angling the window itself (instead of the whole front plate), using an anti-reflection coated silicon window, and simply leaving the window hole open. The results of these tests are shown in Figure 3-11. A calibration curve (discussed in Section 3.2.3) was taken over the same range of freestream temperatures for each window. Note that TC5 and TC6 read lower than the rest, so they were not included in the curve fit. The data suggest that the windowless and tilted-window options did help mitigate some effects near the window edge. Note that on both the silicon and normal sapphire window IR pictures, there are greenish-yellow regions near the left and right sides of the circular window, and the intensity fades to yellow as it approaches the top of the window. Both of these effects are reduced in the tilted sapphire and windowless cases. However, the tilted sapphire and windowless methods allowed flow to leak through the window mount, so further testing would be required to determine if these methods can be adopted without disrupting the freestream conditions. As an additional note, both the normal and tilted sapphire window cases have lower total counts at the same surface temperature as compared to the windowless and silicon window cases. In fact, the silicon window appeared to have a rather high transmittance, as it recorded almost the same maximum counts as the windowless case.

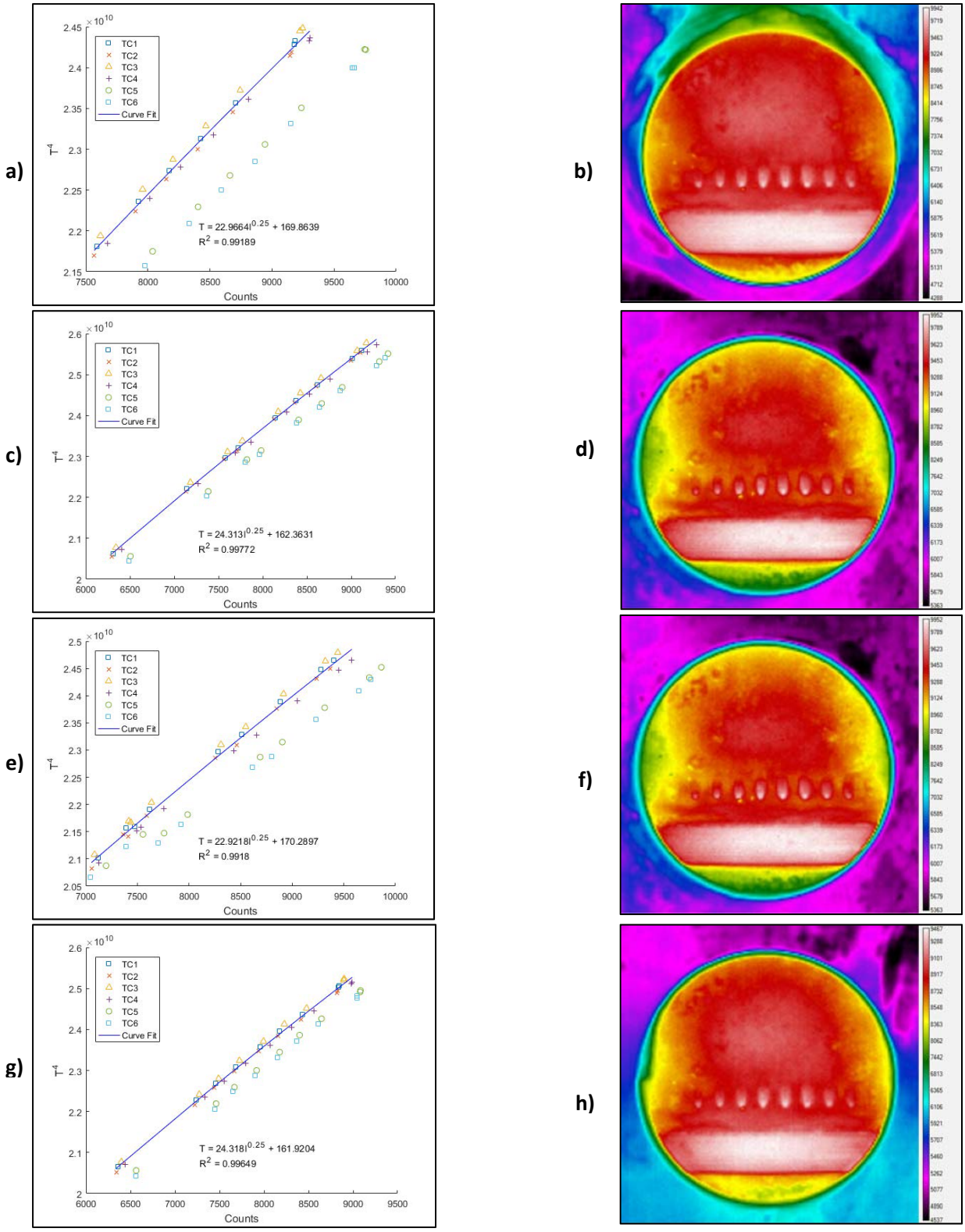

Figure 3-11: Calibration curves and sample IR pictures at equivalent freestream conditions with (a, b) no window, (c, d) sapphire window, (e, f) silicon window, (g, h) tilted sapphire window

During high temperature tests, combustion residue was observed to build up on the inside of the window. A simple method of cleaning off the windows was devised, using a polishing compound and felt Dremel heads. Figure 3-12 shows a sapphire window coated in residue and after being cleaned via this method. Mr. John Welty at the Spartan Felt Company (the manufacturer of the Dremel polishing kit) suggested that a cerium oxide based polishing compound would be the best option for this application.

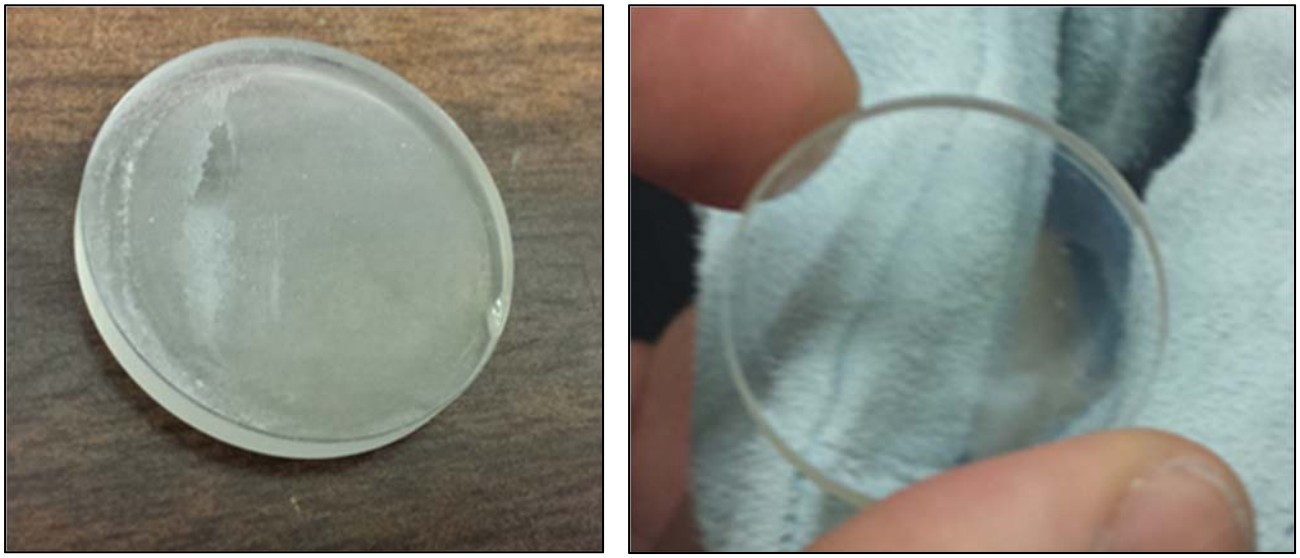

Figure 3-12: Sapphire window with residue (left) and sapphire window post-cleaning (right)

Laser spectroscopy tests were conducted to determine whether the residue had a significant impact on the transmissivity of the window. These tests were performed by Mr. Mike Ranft, using an ABB FTLA2000-157 laboratory FT-IR spectrometer with GRAMS/AI spectroscopy data processing software. The transmittance (percentage of incoming light transmitted through the window) was measured at a wide selection of wavelengths spanning the IR spectrum. Figure 3-13 shows the transmission curves for a dirty window and a window cleaned via the aforementioned

cleaning method. These results show that the residue, although optically visible, has relatively little impact on the transmissivity of the window. The sharp dip at a wavelength of 4.3 μm is due to absorption from CO_2 in the atmosphere, and not from any property of the window.

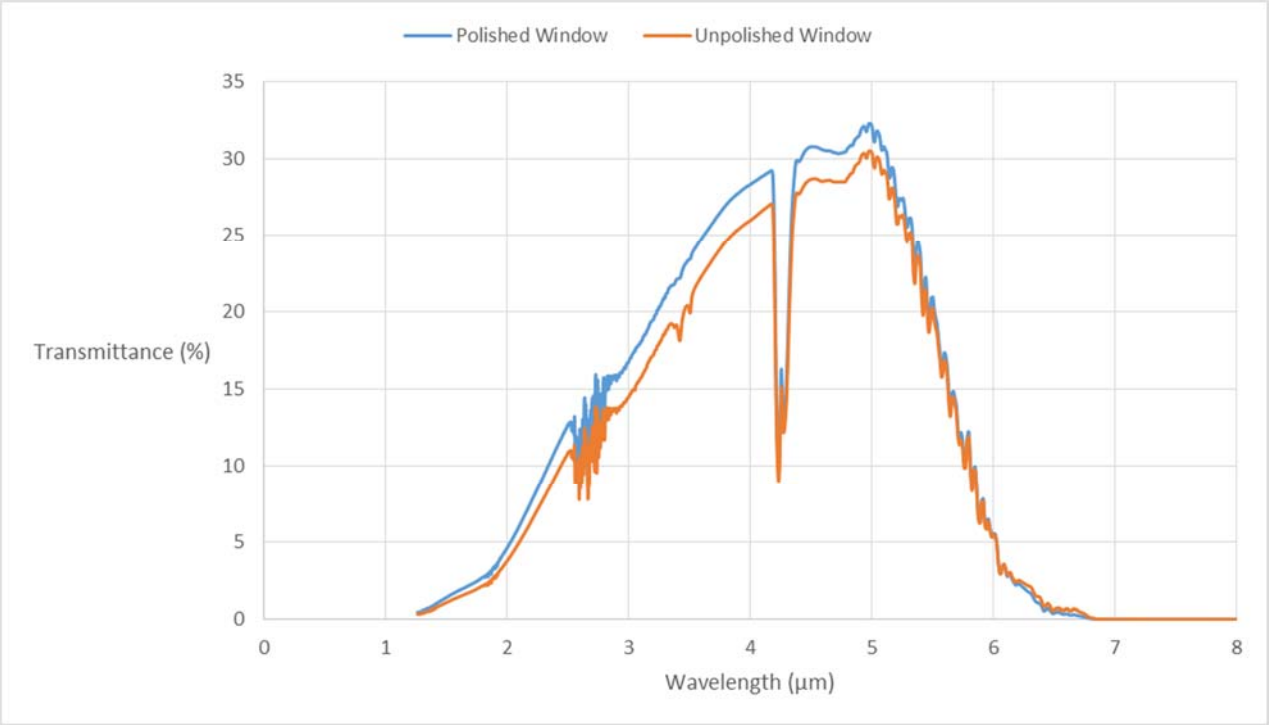

Figure 3-13: Window transmittance vs. wavelength

A series of static pressure ports, shown in Figure 3-10, allowed easy confirmation that the test section was within 0.02 psi of ambient pressure. Running tests at ambient pressures allowed easier calculation of the densities and other pressure-sensitive properties for freestream and coolant gases. A thermocouple immediately ahead of the test plate recorded the freestream temperature, while additional thermocouples provided the freestream temperature further upstream and downstream of the test plate.

3.1.3. Cooling Block Assembly

The cooling block assembly was made to allow a variety of test plates and cooling schemes. Figure 3-14 illustrates the relative position of parts in the fully assembled cooling block. All of the parts were made of a nickel-based superalloy under the proprietary name Hastelloy X. The cooling block assembly fit into a large rectangular hole in the back block of the FCR. Thermocouples were also placed within the cooling block assembly to allow temperature measurements of the coolant gas and the test plate surface and backside wall. The cooling block assembly is made up of multiple components: the test block assembly, the boundary layer bleed slot, and the airfoil test plate.

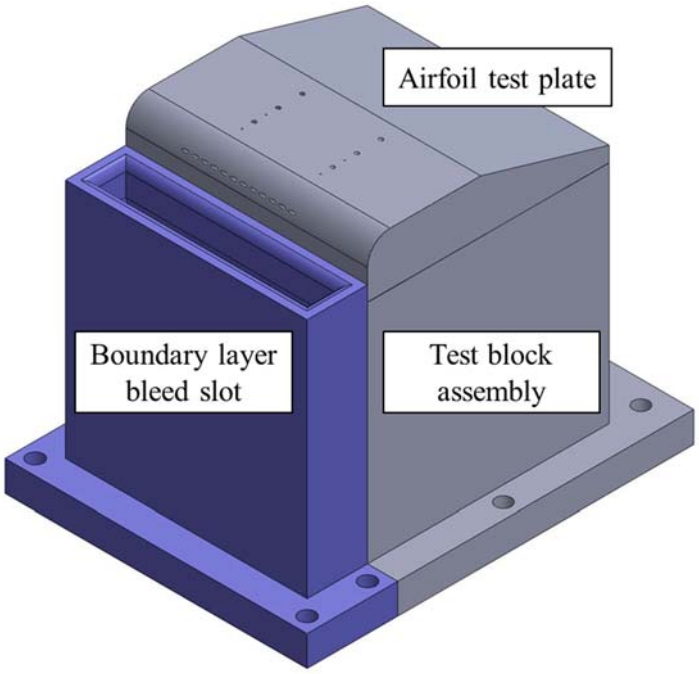

Figure 3-14: Cooling block assembly (figure from Ashby [2])

During testing, a 1200 W OMEGALUX AHPF-121 electric heater and a 400W version of the same heater were used to heat the coolant flow during near ambient tests. A Cole-Parmer 1C6 cooling/heating circulating bath was used to chill the coolant flow for near ambient tests. The bath could reach temperatures as low as 253K and as high was 373K to match different parameters,

such as DR or Re_c. In addition to air, a number of other gases can be used as coolant, such as nitrogen, argon, and carbon dioxide. Compressed bottles of these gases are stored in the tank farm near the propane tanks.

3.1.3.1. Test Block Assembly

The test block assembly contained multiple parts, shown via exploded view in Figure 3-15. The test plate had four legs that fit through holes in the main block and were fastened with small nuts on the exterior. The cooling insert sat between the airfoil test plate and the cooling block to form an internal cooling channel with a constant thickness of 2.21 mm and a width of 3.81 cm. Ashby [2] added the baffle plate to help mitigate coolant distribution issues he encountered. The coolant, introduced through a single pipe, could not spread out into the even channel distribution of the test plate in the limited space available. As a result, the coolant jet would follow one of the walls of the plenum, resulting in very high coolant mass flow on one side of the channel, and almost none on the other. The baffle plate consists of 31 holes with diameters of 0.508 mm.

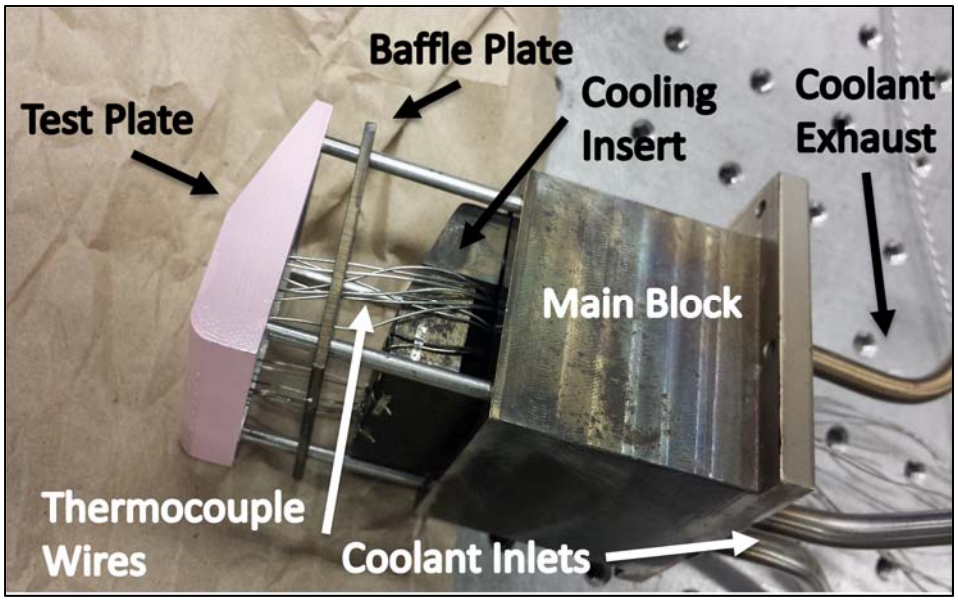

Figure 3-15: Test block exploded view

A new coolant feed, designed by Christian Schmiedel and machined by the AFIT Machine Shop, fed the test block for this investigation. This new design sought to alleviate the aforementioned coolant distribution problems by feeding the coolant through a pair of 6.35 mm (¼ inch) diameter tubes, rather than just the single ¼ inch tube of the previous design. Splitting the coolant in this way effectively doubled the inlet area, shrinking the length of the coolant jets and decreasing the lateral distance that the coolant needed to spread. Christian Schmiedel executed a series of tests on both the old coolant plenum and a comparably-sized prototype of the new design to quantify the difference. An array of thermocouples at the exit of the plenum recorded the temperature as heated air was fed through the piece. Figure 3-16 shows the prototype of the new coolant feed in this test setup. The temperature recorded by the thermocouples was correlated to the mass flow near that thermocouple. Since the prototype was fed with heated air, if a thermocouple was reading near ambient temperature, it implied that less of the air was flowing past that thermocouple. Likewise, a thermocouple with a higher temperature reading was probably had larger mass flow of the heated air blowing past it.

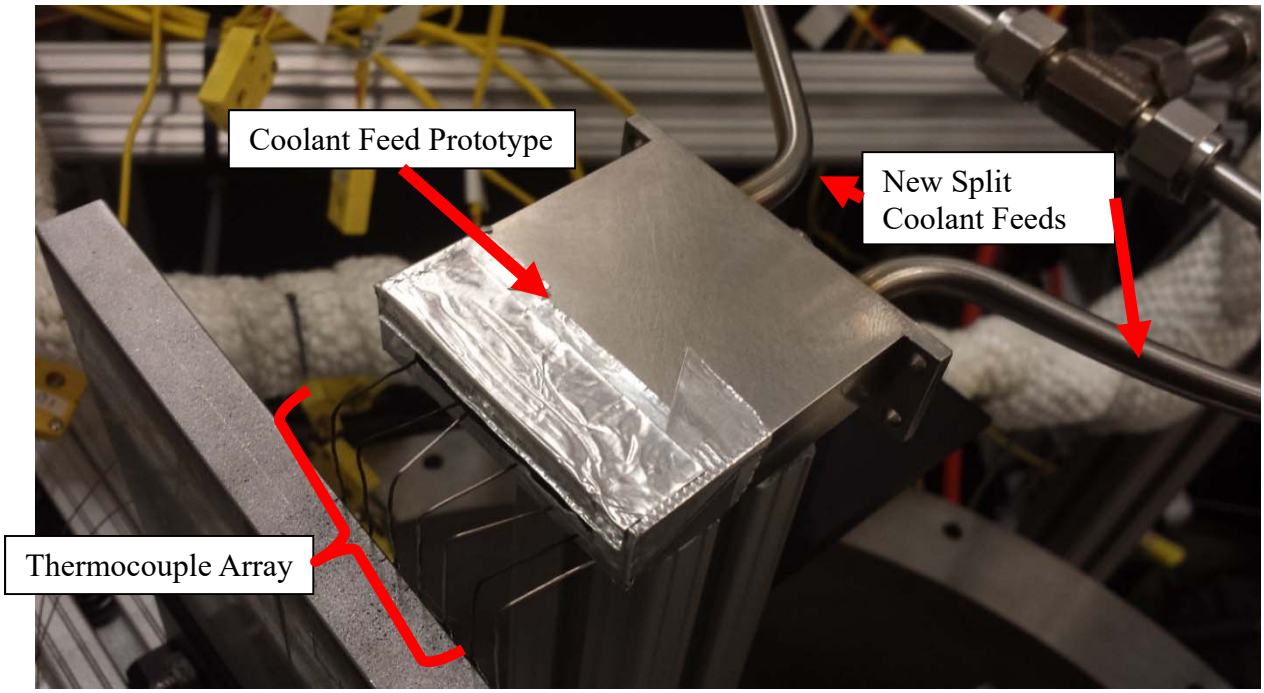

Figure 3-16: New coolant feed prototype in position for flow distribution testing

This simple setup provided an invaluable (although purely qualitative) view of where the majority of the flow was directed by each design. As shown in Figure 3-17, the old design produced a jet that stuck to one side of the plenum, rather than spreading out. By contrast, the new design is quite uniform at low flow rates. At higher flow rates, the new design did produce a pair of jets, but each jet stuck to its own wall, producing a flow distribution that was at least symmetrical, if not uniform. In combination with the baffle plate, this new coolant inlet design displayed a reasonably even flow distribution that was certainly an improvement over the previous coolant feed design. Recall that these conclusions are purely qualitative, as temperature was used as a surrogate for mass flow in these investigations.

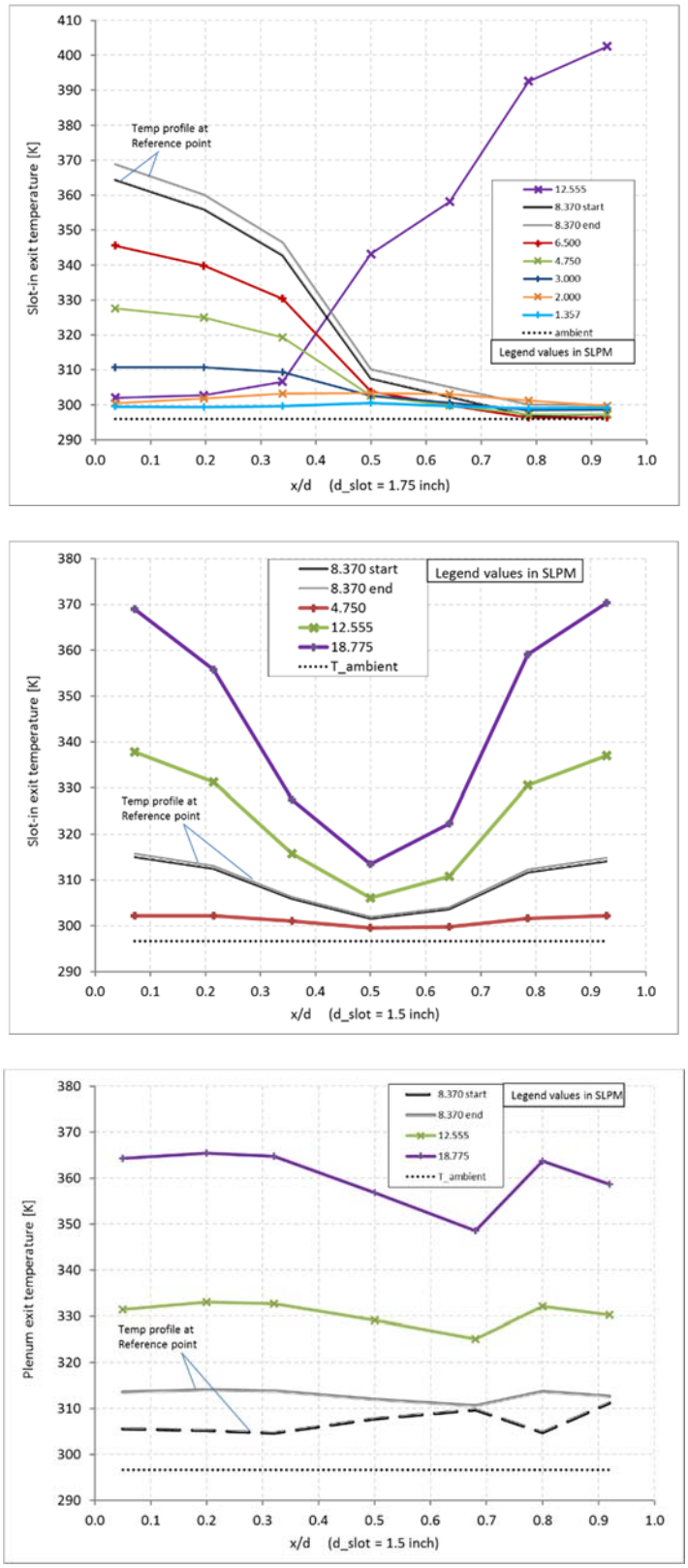

Figure 3-17: Comparison of old (top) and new (middle) coolant design flow temperature distributions and the new design with the baffle plate (bottom)

Once the coolant is introduced to the cooling channel, it can either flow out the film cooling holes in the test plate or exit the channel via the coolant exhaust. A vacuum pump was employed to draw coolant out through the coolant exhaust, since the majority of the coolant would normally exit the channel through the cooling holes rather than traveling through the relatively long exhaust passage. Two MKS Alta 1480A mass flow controllers were used to control the coolant inlet and exhaust flow rates, thus allowing the film coolant flow rate to be controlled as the difference between the inlet and exhaust flow rates. Recesses cut along the sides and bottom of the cooling insert allowed thermocouples to pass around the insert and into the passage in the main cooling block. Figure 3-18 highlights some of these features.

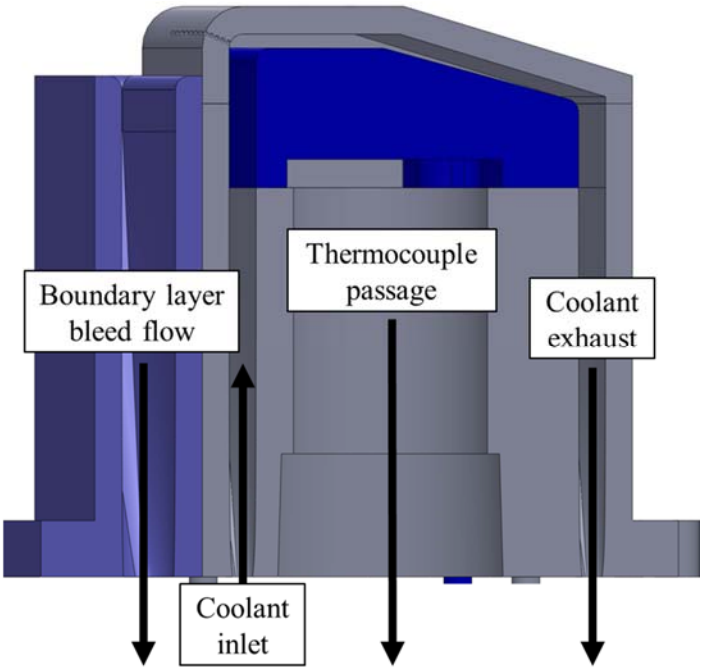

Figure 3-18: Cooling block assembly cross-section with flow paths

During high temperature tests, the coolant exhaust reaches temperatures that are well above the safe operating temperatures of the mass flow controller on that end. To avoid damaging the equipment, the coolant exhaust flowed through a looped copper tube immersed in a bucket of

water, which acted as a simple (but effective) heat exchanger, as shown in Figure 3-19. During actual testing, the bucket would be filled to completely submerge the loops. The inner flow path through the block is discussed in greater detail in Section 3.1.3.3.

Figure 3-19: Bucket heat exchanger for coolant exhaust

The internal coolant flow field is difficult to characterize, due to the interaction of the coolant plenum, the baffle plate, the 90 degree bend at the leading edge, and the channel flow. Table 3-1 shows two Reynolds numbers for the flow, the first based on the jets formed by the baffle plate ($Re_{c,jet}$) and the second based on the coolant channel under the flat portion of the test plate ($Re_{c,D}$). These two Reynolds numbers were calculated for two of the total coolant mass flows used during the IR tests in Section 4.2, using the gas properties of air. The Reynolds numbers for the jets were high enough to indicate turbulent flow at every case. At the lower coolant mass flow rates, the Reynolds numbers for the flat portion were low enough that it could be laminar. However, there is not enough information to say definitively whether the flow became laminar or

remained turbulent. The convection coefficient, h, can be found for some cases by employing an empirical correlation between the Nusselt, Reynolds, and Prandtl numbers of a flow. However, because our coolant flow path is unique, it does not fit any commonly used correlations. The range of likely h values can be estimated by considering the cases of pure impingement from the baffle plate holes and fully developed channel flow, because the coolant has been observed to impinge upon the inside surface of the test plate, and the flow should eventually reach fully developed channel flow as it travels beneath the test plate. For the lower mass flow rates, the channel flow was assumed to be laminar, so $Nu = 7.54$ based on tabulated values for fully developed laminar flow in non-circular tubes, according to Incropera et al. [10]. The Nusselt number correlation used for the turbulent channel flow at the higher mass flow rates accounted for property variation due to temperature within the coolant [10]:

$$Nu_D = 0.023 Re_D^{\frac{4}{5}} Pr^{\frac{1}{3}} \left(\frac{\mu}{\mu_s}\right)^{0.14} \tag{3-1}$$

where μ is the dynamic viscosity at the metal temperature, and μ_s is the dynamic viscosity at the coolant temperature. The Nusselt and Reynolds numbers Nu_D and Re_D are based on the hydraulic diameter D_h, which can be calculated for a rectangular channel from the channel height (a) and the channel width (b) [10]:

$$D_h = \frac{4ab}{2(a+b)} \tag{3-2}$$

The Nusselt number correlation used for the impingement jets was more complicated, as it relied on more parameters, including the diameter of the jet orifice (D), the distance from the jet orifice to the impingement surface (H), and the spacing of the jets in the staggered array (S) [10]:

$$\frac{\overline{\overline{Nu}}}{Pr^{0.42}} = 0.5\left(1+\left(\frac{\frac{H}{D}}{\frac{0.6}{\left(\frac{\pi D^2}{4S^2}\right)^{\frac{1}{2}}}}\right)^6\right)^{-0.05}\left(2\left(\frac{\pi D^2}{4S^2}\right)^{\frac{1}{2}}\frac{1-2.2\left(\frac{\pi D^2}{4S^2}\right)^{\frac{1}{2}}}{1+0.2\left(\frac{H}{D}-6\right)\left(\frac{\pi D^2}{4S^2}\right)^{\frac{1}{2}}}\right)Re^{2/3} \quad (3\text{-}3)$$

The convection coefficient was then calculated from these Nusselt numbers using the appropriate linear dimension and thermal conductivity. The estimated *h* value ranges are presented in Table 3-1, alongside the Reynolds numbers. Note that *h* increases for higher temperatures and total coolant mass flows.

Table 3-1: Coolant *Re* and *h* at multiple conditions

	Low Temperature (380K)		High Temperature (850K)	
Parameter	**ṁ = 1.8 x 10^-3 kg/min**	**ṁ = 7.3 x 10^-3 kg/min**	**ṁ = 4.15 x 10^-3 kg/min**	**ṁ = 1.6 x 10^-2 kg/min**
$Re_{c,jet}$	6583	26700	8873	34211
$Re_{c,D}$	1010	4096	1361	5248
h_{jet} (W/m^2*K)	2594	6598	6900	16966
$h_{channel}$ (W/m^2*K)	234	491	507	1283

3.1.3.2. Boundary Layer Bleed

Since the boundary layer bleed pulls air from the freestream, it required a heat exchanger similar to the coolant exhaust at high temperatures. The bled gas traveled through a 1.2 m long concentric tube, counter-flow heat exchanger cooled by water from the cooling water lines for the lower half of the WSR toroid. Since combustion products contain water vapor, the heat exchanger included a water trap, to prevent excessive moisture from reaching the boundary layer bleed mass flow controller.

The purpose of the boundary layer bleed was to adjust the position of the stagnation point at the leading edge of the test plate by bleeding off the boundary layer flow that develops along the test section wall. This adjustment helped the flow around the test plate more closely

approximate the flow around a full airfoil. Gas was drawn through the boundary layer bleed by a vacuum pump, while a 200 SLPM MKS mass flow controller controlled the amount of gas removed. In practice, the boundary layer bleed flow was limited to about 23 SLPM during low temperature testing. This limitation could be solved with a larger, more powerful vacuum pump, but that particular modification was not made during this investigation, as it may not be necessary. No in-depth analysis of the location of the stagnation point has been performed yet, so the impact of the boundary layer bleed cannot be accurately gauged at this juncture. During low temperature testing, the boundary layer bleed pulled away a larger proportion of the pre-bleed freestream flow than during high-temperature testing.

Speaking approximately, the boundary layer bleed removed 23 SLPM of the 320 SLPM freestream during low temperature testing, versus 20 SLPM of the 620 SLPM freestream during high temperature testing. It is hypothesized that the boundary layer bleed pulled less flow at high temperatures due to the reduced density of the freestream. The height of the turbulent boundary layer can be estimated using the freestream Reynolds number over that flat region (Re_x) and the distance from the boundary layer trip to the boundary layer bleed (x). By approximating the boundary layer growth as similar to that for turbulent flow over a flat plate, we can use the empirical equation [48]

$$\delta \approx \frac{0.37x}{Re_x^{\frac{1}{5}}} \tag{3-4}$$

where δ is the boundary layer thickness. Using 10.16 centimeters for x and 27510 for Re_x (a representative value at test flow conditions) the estimated boundary layer thickness is 0.488 centimeters. A conservative estimate of the height of flow removed by the boundary layer bleed can be made by assuming evenly distributed mass flow throughout the channel. At low temperature, the bleed is estimated to remove about 0.137 centimeters of the flow, while at high

temperature the value is estimated at 0.056 centimeters. Based on this conservative analysis, the boundary layer bleed pump might not be strong enough to completely remove the boundary layer of the flow. A more in-depth investigation of the flow field within the test section would help determine whether these values are truly sufficient to remove the boundary layer and whether the difference in the removed height of flow has a notable impact.

The coolant in the FCR tended to pick up significant amounts of heat between our temperature control devices (the chiller and heater) and the actual film cooling holes on the test plate. Much of the heat was hypothesized to come from the boundary layer bleed flow. The relative positioning of the coolant feed and boundary layer bleed effectively formed a cross-flow heat exchanger, wherein the hot boundary layer bleed flow transferred heat through the conductive Hastelloy X block to the coolant. Because of this heat addition, increasing the coolant mass flow also decreases the coolant temperature, making it difficult to examine the effects of these two control inputs separately. To eliminate the unwanted coolant heating, a new boundary layer bleed design, developed by Christian Schmiedel, was implemented. The new design, shown in Figure 3-20, created a small air gap between the boundary layer bleed and the test block, with the goal of limiting the conduction to the coolant. A series of thermocouples were placed at various points within this gap to record the temperatures of the walls and air at various points to assess the effectiveness of the design.

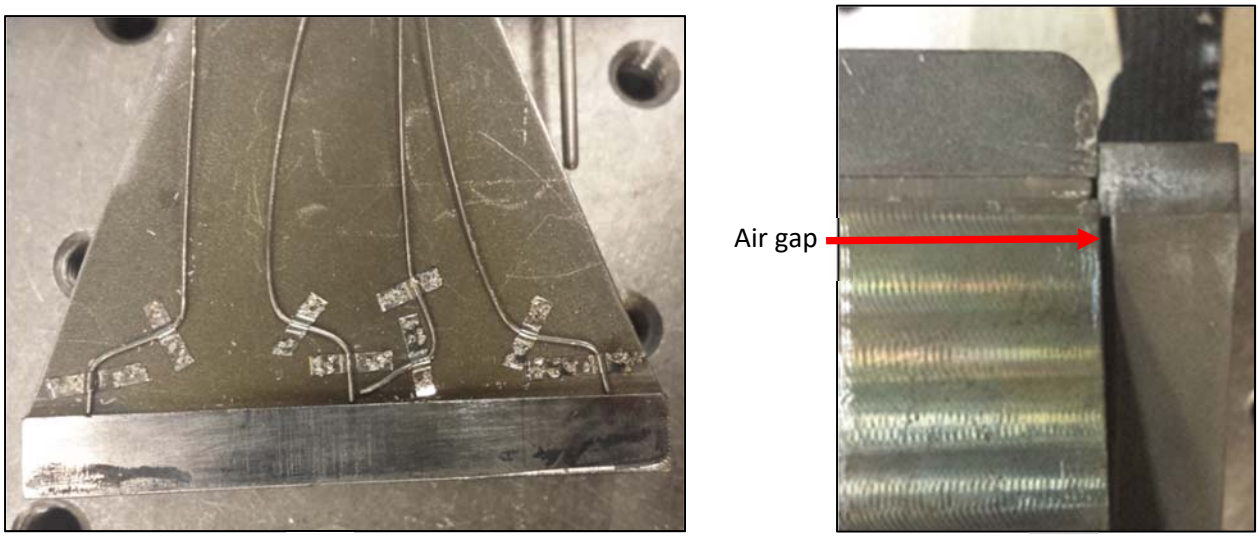

Figure 3-20: a) Top view of the new boundary bleed with diagnostic thermocouples, b) Side view of the boundary layer bleed set in position with the coolant block

After analyzing data collected both during this investigation and by Ashby [2], Christian Schmiedel found that for a freestream temperature of 1300K, the new boundary layer bleed design provided coolant flow temperatures about 50K-100K lower than the old design at similar coolant mass flow rates. Figure 3-21 provides a comparison of the data. This decrease in coolant heating represents a notable improvement over the old design.

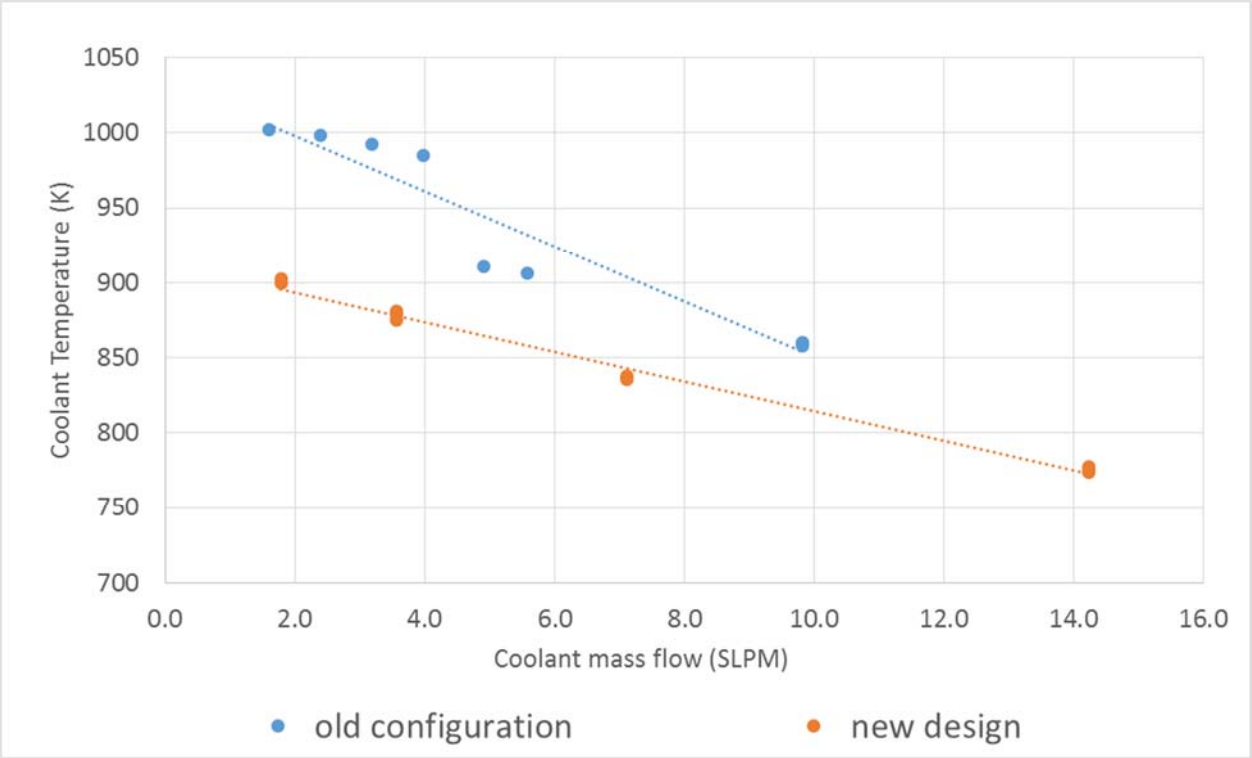

Figure 3-21: Comparison of old and new boundary layer bleed designs at 1300K freestream temperature (figure by Christian Schmiedel)

3.1.3.3. Test Plates

The two test plates used in this investigation are the same test plates used by Ashby [2]. The test plates had identical geometries, as shown in Figure 3-22, but were equipped with different film cooling hole schemes. The shape of the plate consisted of a quarter cylinder leading edge, a flat section, and a sloped afterbody. This shape was based on the scaled-up model used by Ekkad et al. [36], but without being placed in the middle of the test section. The test plates were more closely matched to real engine dimensions at one-tenth the size of those models, with a leading edge diameter of D = 9.50mm (0.374 inches). The thickness of the test plate on the leading edge and flat were designed to allow the inclusion of film cooling holes with dimensions akin to those on real turbine blades, but the downstream portion was made thicker to help reduce uncertainty in conductive heat flux calculations in previous instrumentation schemes [2].

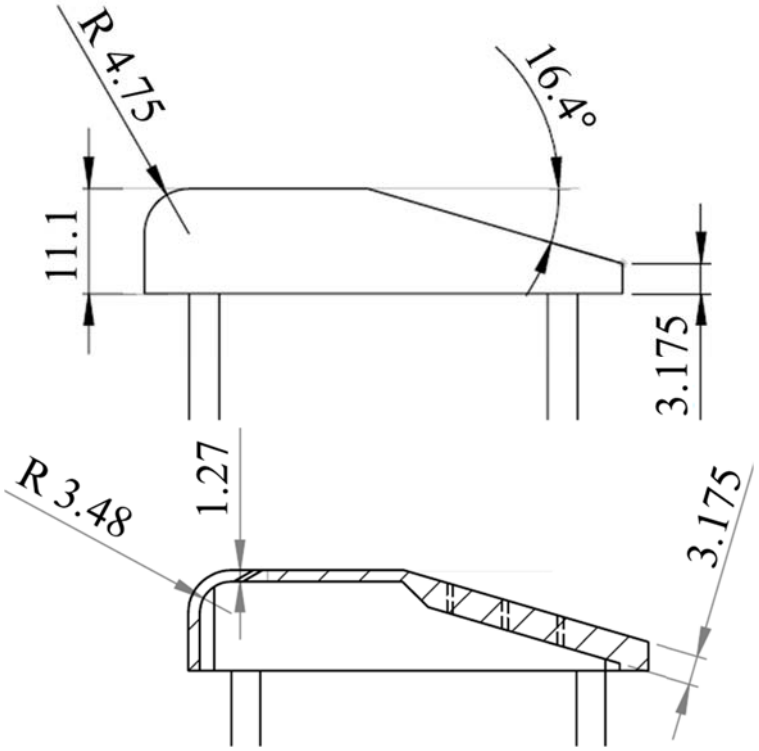

Figure 3-22: Side views of representative turbine airfoil leading edge test plate (from Ashby [2])

The first test plate was equipped with a film cooling hole scheme designed to match a model used in the Leading Edge Film Cooling Tunnel (LEFCT), operated by the Air Force Research Lab (AFRL). Their model, as described by Wiese et al. [18], used a single film cooling hole on a model identical to that used by Ekkad et al. [35]. For the FCR test plate, the scheme consisted of 8 holes located 21.5 degrees along the quarter cylinder leading edge, with dimensions d = 0.51mm (0.02 inches), α = 20 degrees with respect to the surface, and a compound angle of 90 degrees. The ratio of hole length to diameter was L/d = 7.31. Figure 3-23 illustrates the cooling hole dimensions and placement.

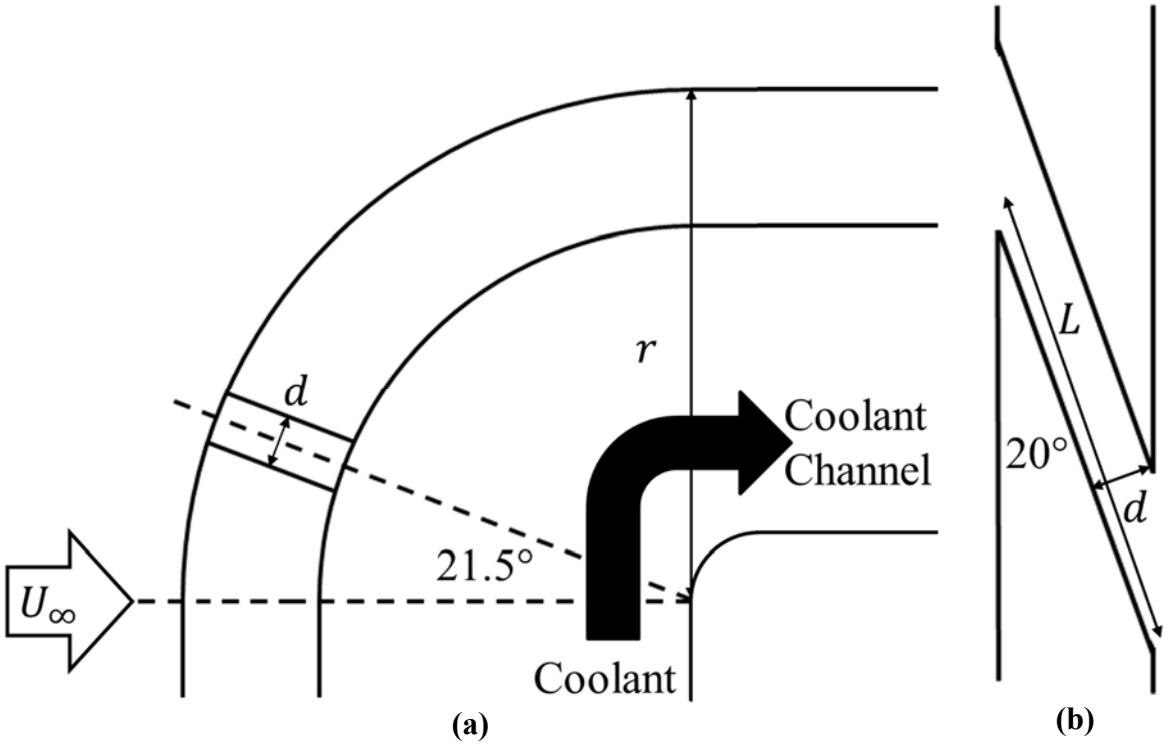

Figure 3-23: FCR one-row showerhead model schematics: (a) side view and (b) coolant hole top view (from Ashby [2]**)**

The second test plate included a series of film cooling holes on the flat part of the plate that were designed to match the hole examined by Greiner et al. [16]. The shaped holes were streamwise-oriented, with α = 30 degrees to the surface and $\delta = \beta$ = 10 degrees. The pitch and hole length were also equivalent, at P/d = 4 and L/d = 5 for hole diameter d = 0.508 mm (0.020 inches). The plate has sixteen holes distributed evenly from the centerline, but only the center eight were used for these investigations. The unused holes were plugged with high temperature epoxy. Figure 3-24 shows the schematics of the film cooling hole and the cooling scheme.

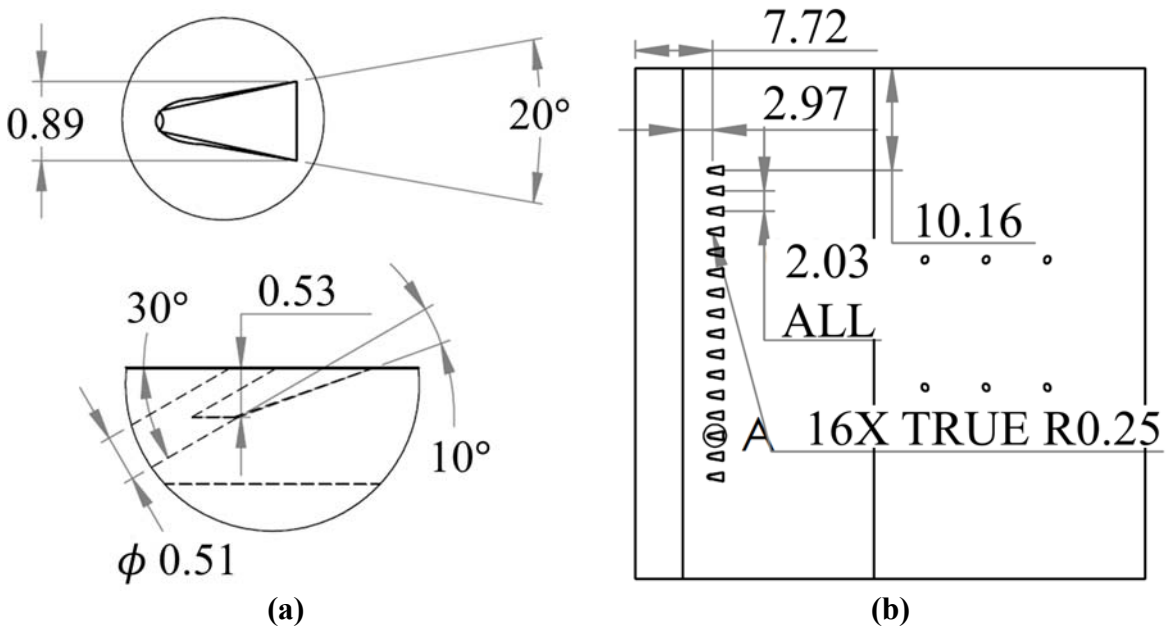

Figure 3-24: Schematics of (a) shaped hole and (b) shaped hole cooling scheme (from Ashby [2])

Both test plates were outfitted with a plethora of thermocouples, to record surface, backside, and internal channel temperatures. The surface thermocouples, used for calibrating the IR camera, were fed into holes in the test plate so that the beads at the end of the thermocouples could be welded as flush as possible to the surface of the plate. The backside thermocouples were set into shallow channels near the corresponding surface thermocouple so that the bead could be laser welded flush with the backside of the test plate. This backside thermocouple placement method was an attempt to improve the reliability and accuracy of backside thermocouple measurements, but encountered significant difficulties in application. Many of the backside thermocouples were damaged due to the tight conditions during laser welding. Even some of the surface thermocouple wires were damaged. As shown in Figure 3-25, the large number of thermocouples are placed within a relatively small space. The thermocouples were first anchored via tack welding at AFIT with nichrome strips to hold them in place for the laser welding process. Precision Joining Technologies (PJT) performed the laser welding. They recommend that if the

legs of the test plates could be detached, they would have better access to the welding area and would be able to avoid damaging the thermocouples in the future. Lastly, the internal channel thermocouples were placed on the cooling block insert, to measure the temperature of the coolant within the channel at multiple locations.

Figure 3-25: Underside of the first test plate

The surface and backside thermocouples locations were based on the placement developed by Ashby [2]. As shown in Figure 3-26, the thermocouples were concentrated within the region near the film cooling holes, where the IR camera was focused. Figure 3-27 illustrates the cross-section of the instrumentation scheme for the surface, backside, and internal channel thermocouples. Six thermocouples were placed in lateral pairs at x/d = 5, 10, and 20 with each pair nominally located along the centerline of a cooling hole. The pair at x/d = 5 aligned with the fourth hole outboard from the plate centerline, and the pairs at x/d = 10 and 20 were aligned with

the third hole outboard from the plate centerline. Finally, a seventh thermocouple was placed at $x/d = 25$ along the centerline of the plate.

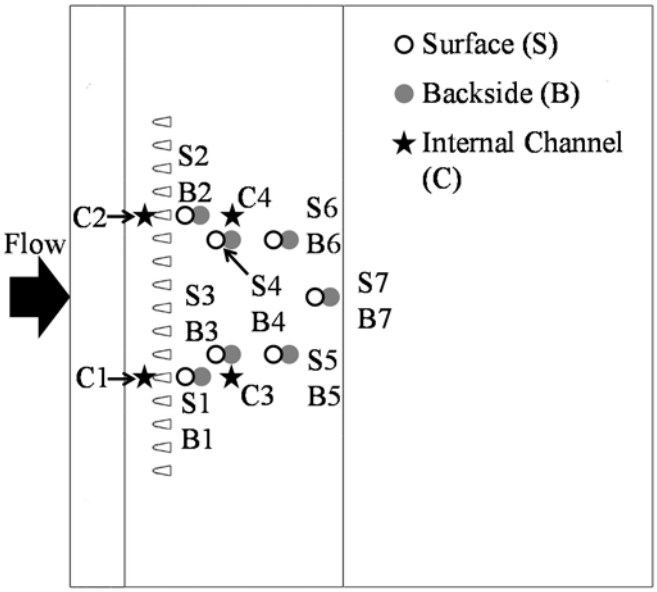

Figure 3-26: Thermocouple instrumentation scheme (modified from Ashby [2])

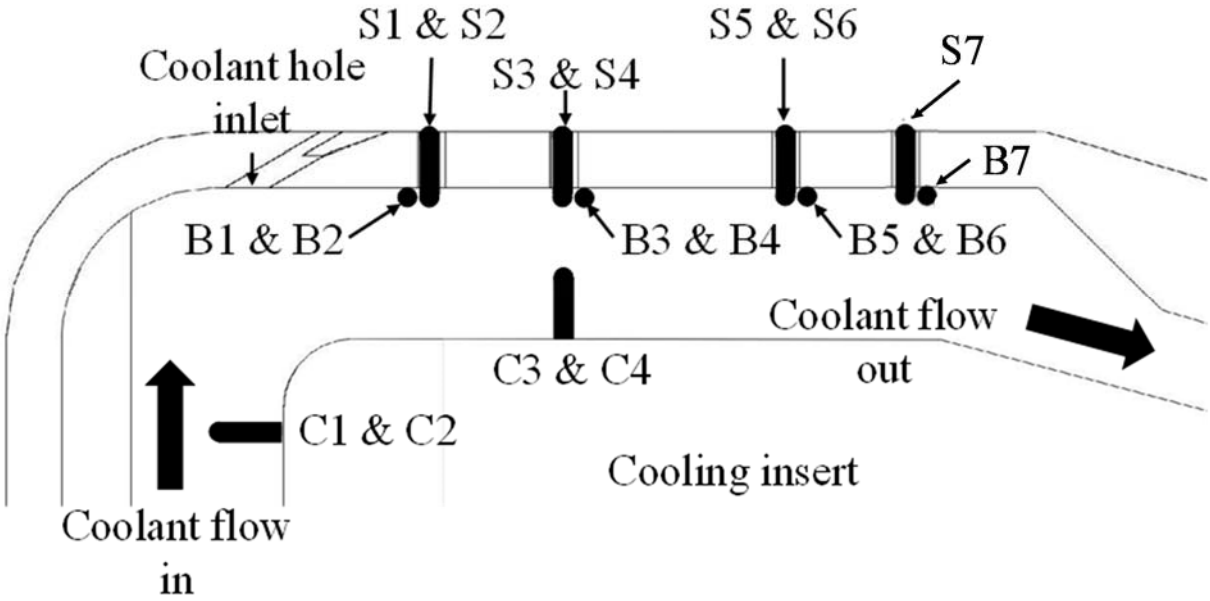

Figure 3-27: Cross-section of thermocouple locations (modified from Ashby [2])

3.2. Additional Equipment

The FCR makes use of several external pieces of equipment to gather data and control test conditions. Multiple new pieces of equipment were used for this investigation, in addition to those already present in the COAL Lab. This section provides a general overview of external equipment, information about the newly added equipment, and a more detailed look at the IR camera. Section 3.2.1 discusses the bulk of the COAL Lab equipment that supports the FCR. Section 3.2.2 outlines the PSP-specific test equipment. Finally, Section 3.2.3 discusses the IR camera and related equipment used for the IR thermography tests.

3.2.1. COAL Lab Equipment

Most of the external equipment used in this investigation was already in place. The AFIT labs share a compressed air system, fed by two Kaeser BSD-50 air compressors. This system could provide in excess of 1200 SLPM of air if necessary, but lower flow rates met all air flow requirements for both the freestream and film cooling gas. For coolant gases other than air, the film cooling was fed by compressed gas cylinders located in the tank farm. A Welch WOB-L 2585 vacuum pump provided suction for the coolant exhaust and boundary layer bleed flows. During high temperature testing, these gases, as well as the flow exiting the test section, were exhausted through a fume hood to the exterior of the building. The exhaust system is shared between multiple test rigs within the COAL Lab, so a series of dampers and flues were used to maximize suction through the fume hood above the FCR.

All relevant gas flows were controlled via mass flow controllers. The freestream flow was measured by a Fox Thermal Instruments, Inc. FT2 flow meter and controlled by a Eurotherm 2404 process controller in conjunction with a Badger Meter, Inc. Type 807 valve and Type 755 pneumatic actuator. A Brooks 5853i mass flow controller managed the propane flow for high

temperature tests. It is capable of handling up to 200 SLPM of propane, but tests never required more than 16 SLPM. The film coolant, boundary layer bleed, and spark ignitor flows were all controlled with various MKS mass flow controllers managed via an MKS Model 647C multi gas controller. The specific models of MKS controllers include MKS MC20 and Alta 1480 models, with maximum flow rates selected according to the expected levels of each particular flow.

A Mesa Labs Bios Definer 220 enabled calibration of the MKS flow controllers for flow rates between 0.3 and 30 SLPM. Two sweeps of calibration points were taken for each controller the first starting at 5% of the controller's flow capacity and increasing by 10% up to 95% and the second starting at 100% of flow capacity then decreasing by 10% down to 10%. A trend line was fit to the data with the measured flow rate as a function of the flow rate setpoint. A correction factor was then applied in the multi gas controller so that a setting of 0% truly gave zero flow and the slope of the trend line became one. The calibration points were then re-taken to verify the efficacy of the calculated corrections. These calibrations were expected to put the controllers within the flow accuracy reported by the manufacturer. The topic of uncertainty is discussed further in Section 3.4.1.

As described previously, temperature measurements were recorded using numerous thermocouples and an SC6700 infrared camera, described in more detail in Section 3.2.3. B-type thermocouple were used to measure the test section inlet temp and WSR core temp during high temperature tests, while K-types were used for all other applications. An ESP-32HD pressure scanner from Pressure Systems, Inc. and an accompanying DTC Initium controller were used to take the pressure measurements in the test section.

Temperature and freestream flow rate data were recorded using a LabView program developed by Lynch [19]. The program controlled the freestream flow rate and solenoids that could close any of the flow lines for the FCR.

3.2.2. PSP Equipment

For PSP testing, an optical window was composed of fused silica (quartz) for visible light transparency and designed to fit into the mount for the existing sapphire window plate. Other pieces of equipment, such as an excitation illumination source, PSP image acquisition and processing software, a CCD camera, and supporting optics and filters for the camera were all supplied by Innovative Scientific Solutions, Inc. (ISSI).

The CCD camera used was an Imperx Bobcat with 804 x 604 pixel resolution. The PSP tests taken early on in this study focused on the curved leading edge of the test plate, so a spatial calibration was necessary. This calibration was accomplished using a method developed by Ashby [2] using a printed grid adhered to the test plate. Since the distance between gridlines was known, it was possible to create a spatial map of each pixel location using an image of the test plate with the grid. Figure 3-28 shows the calibration images, one without the grid that has the pixel locations of the film coolant holes and the end of the leading edge marked, and one with the grid that has the intersections marked. The positions of the intersections were then offset by the location of the film cooling holes and normalized to generate pixel locations in terms of x/d and y/d.

a)

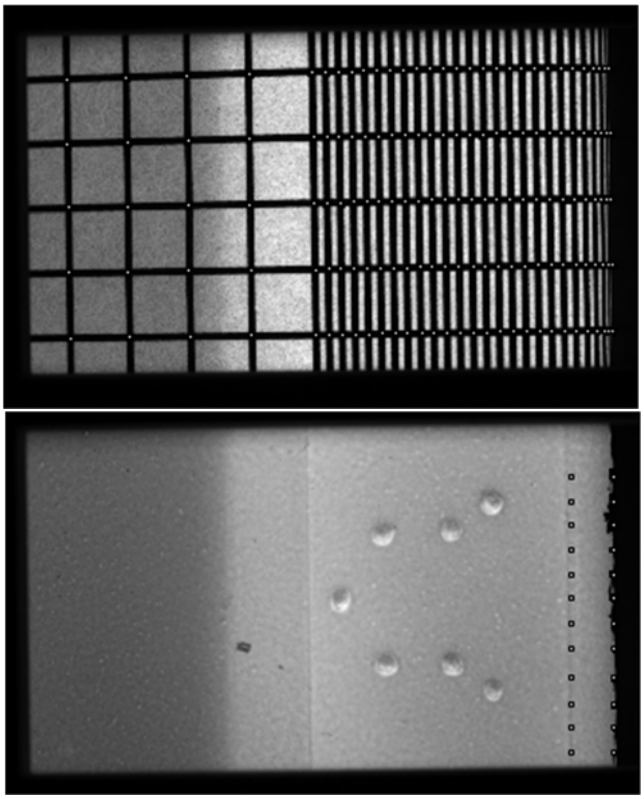

b)

Figure 3-28: PSP Spatial Calibration Pictures a) with grid intersections marked b) no grid with film cooling hole locations and end of leading edge marked

3.2.3. IR Camera

All thermal tests were taken using a FLIR SC-6700 infrared camera to record the surface temperature of the test plate at a high spatial resolution. The camera detects infrared radiation in the 3000-5000nm range. To properly interpret data from the camera, both a spatial and thermal calibration were necessary. Both of these calibrations were carried out via methods very similar to those described in detail by Ashby [2] and discussed here.

The thermal tests in this study focused on the test plate that had shaped holes on the flat portion of the test plate. For the spatial calibration, a value of pixels per inch was determined by counting the number of pixels between two points and dividing by the known distance between those points. The distance was normalized by the coolant hole diameter and expressed relative to

the coolant hole position. Lens distortion was deemed negligible, so this method does not take it into account.

Since the IR camera measures the emitted radiation intensity, a calibration is necessary to relate that intensity to the test plate surface temperature. The thermocouples on the surface of the test plate provide the measured temperature at multiple points on the surface. By varying the temperature in the test section, a range of surface temperatures spanning above and below the expected test conditions were recorded by the thermocouples and compared to corresponding images captured by the IR camera. Half of these points were taken in ascending order of temperatures, and the other half taken on the way back down, to attempt to account for hysteresis. Changing the freestream temperature in small, precise increments proves difficult with our equipment, so the ascending and descending points were not necessarily taken at the same exact freestream or surface temperatures. As shown in Eq. (2-21), radiative heat transfer displays fourth-order behavior, allowing the relationship between temperature and measured IR intensity to be characterized as:

$$T = a\mathcal{I}_{rad}^{1/4} + b \tag{3-5}$$

where $\mathcal{I}_{rad}$ is a count of photons striking the IR camera sensor and a and b are constants assigned by a curve fit. This process was performed at appropriate temperature ranges for near ambient and high temperature tests and repeated whenever any sort of adjustment or modification was made to the test section, such as swapping in a new IR window or disassembly/reassembly.

Early calibrations were taken separately from test data, with significant time allotted to achieving a steady state condition for each calibration point. However, this method took unacceptably long periods of time to complete, up to an entire day of constantly running and watching the FCR. It was found calibration points could be captured in tandem with experimental

data by taking quasi-steady points as the rig heated up to test conditions and cooled back down afterwards. The only additional effort necessary was to heat the rig past test conditions after all test points were taken, to ensure that the calibration included points at higher temperature than seen in the test data. This method produced calibration curves with equally good agreement as the former method, so the newer method was adopted. Examples of multiple calibration curves are shown in Figure 3-29. Note that for some of the curves, it was clear that one or two thermocouples departed from the pack. In these cases, those stray thermocouples were excluded from the curve fit. For example, in the top and bottom curves in Figure 3-29 (the first set of low and high temperature data, respectively), S5 and S6 (the rearmost thermocouples) were too close to the window boundary, and gave low count readings. The middle curve (for the second set of low temperature data) was taken after the other two, so the window placement was adjusted, removing this issue.

The slope of the calibration curve for the second set of low temperature data is a bit higher than for the first set of low temperature data. It is hypothesized that this shift is due to a minor change in the emissivity of the plate caused by oxidation of the paint during high temperature testing, which occurred between the two low temperature test sets. This change does not negate the ability to compare these two sets of data, since the calibration curves account for the difference. Note that the uncertainty of K-type thermocouples is reported as 0.75% by the manufacturer, which translates to 2.8K for low temperature tests and 6.45K for high temperature tests. The residuals of each curve were analyzed by taking the root mean square, to see how closely the curve falls to the actual data points. This analysis produces values of about 1.7K for the low temperature tests and 4.1K for the high temperature tests.

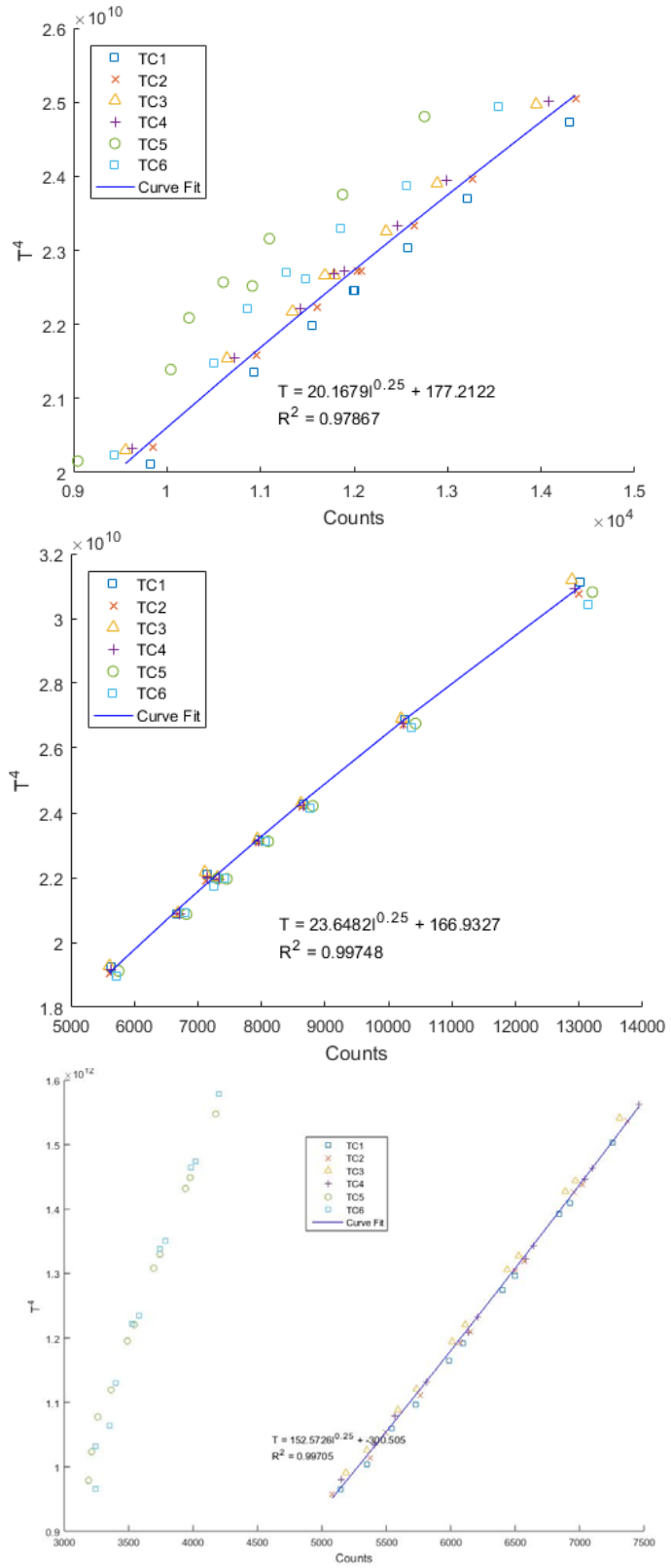

Figure 3-29: Representative IR calibration curves at low temperature (top and middle) and high temperature (bottom)

The test plate was coated with a temperature-resistant flat black paint to make the surface emissivity as uniform as possible. However, it was noted that the beads of the surface thermocouples radiated a bit differently from the rest of the test plate, due to their raised, bump-like nature. To circumvent this issue during calibration, the thermocouple recorded temperature was compared to an averaged area of the surface adjacent to the thermocouple, covering several pixels. This approximate region is shown in Figure 3-30 for a representative high temperature case. In the example shown, the thermocouples are clearly visible, with count levels of 3100, compared to about 3400-3600 counts in the immediately adjacent boxed region. For a typical low temperature calibration, this difference equates to about 4 K. The difference could impact the calibration because it is not certain whether the count difference is from an emissivity difference, the raised geometry of the thermocouples, or from an actual temperature difference between the thermocouples and the neighboring regions. Because the airfoil had a high conductivity, it was assumed that the temperature is relatively uniform and that the intensity difference must therefore be due to one of the first two possibilities.

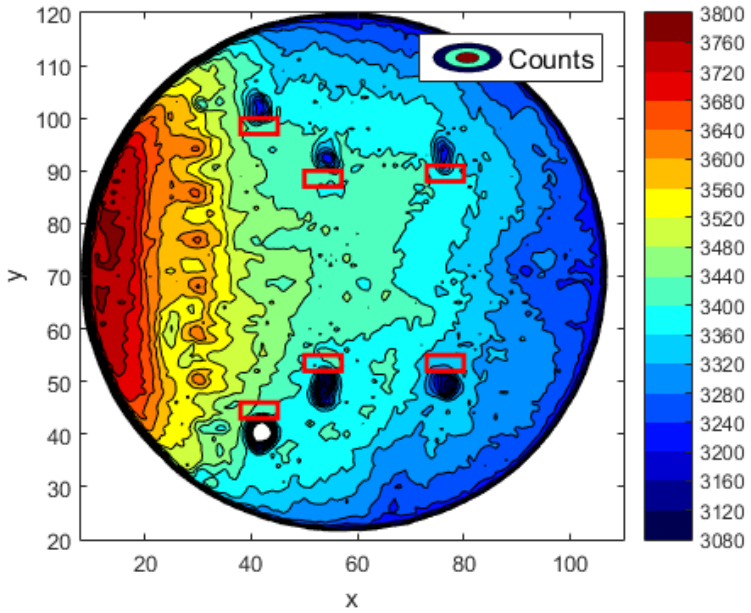

Figure 3-30: IR calibration intensity measurement region (from Ashby [2])

When the WSR was on for high temperature tests, a 3900 nm bandpass filter was applied to screen out any emissions from combustion products in the freestream flow. For these tests, the integration time was set to 0.01 milliseconds to prevent saturation of the IR camera. For near ambient testing, the filter was not necessary, as no combustion was occurring. Likewise, lower temperatures necessitated a longer integration time of 0.3-0.5 seconds to produce an amenable signal-to-noise ratio. Since the IR camera saturated at a counts value of 15000, the integration time was typically adjusted to achieve a count value of 10000-14000

3.3. **Test Setup and Data Reduction**

Some early tests in this investigation used PSP equipment to capture data. Most of the other tests used the IR camera to capture temperatures across the test plate surface. This section discusses the test setups and data processing used for these tests. Section 3.3.1 discusses the data acquisition systems that were shared across both types of tests, while Section 3.3.2 provides an overview of the PSP test setup. Finally, Section 3.3.3 describes the IR thermography test setup.

3.3.1. Shared Data Acquisition Systems

The PSP and IR tests focused on different types of data to produce their respective results, but they shared a number of key measurements that were used to monitor the test conditions of the experiments. This section discusses those measurements and how the collected data was used to calculate important flow parameters.

3.3.1.1. Key Temperatures and Flow Rates

Some of the important temperatures in the FCR included coolant and freestream gas temperatures and metal temperatures on the test plate. Coolant gas temperature was determined using the four thermocouples within the internal coolant channel consistent with Figure 3-26 and

Figure 3-27. These 0.51 mm diameter K type thermocouples were anchored to the cooling insert and bent to extend their tips approximately halfway into the space between the cooling insert and test plate. Unfortunately, one of the internal channel thermocouples, C3, did not provide consistent measurements, perhaps due to of damage. The value for T_c was determined as the average of internal channel thermocouples C1 and C2 (Figure 3-26 and Figure 3-27). This value was normally quite close to the value of internal channel thermocouple number 4, within about ~0.3K for low temp and ~1K for high temp, which is within the maximum error of the thermocouples (0.75% for K-types is ~2.8K for low temp and ~6.45K for high temp, according to the manufacturer). This variance was deemed acceptable.

Freestream gas temperature was measured by a 0.51 mm diameter K type thermocouple inserted partially into the test section just ahead of the test plate. At near-ambient conditions, these readings were similar to, but slightly lower than, the readings of the thermocouple at the FCR inlet. For example, the freestream would be at 420K when the FCR inlet read 430K. The temperature difference was greater during high temperature testing, with typical drop-offs from 1380K down to the freestream 1300K.

Test plate surface temperatures were measured using 0.508 mm diameter K type thermocouples laser welded flush to the test plate surface, as described in Figure 3-25 . The laser welding was performed by Precision Joining Technologies. Metal temperatures along the backside of the test plate surface (the surface adjacent to the internal coolant channel) were also determined using 0.508 mm diameter K type thermocouples. The backside thermocouples were placed immediately adjacent to wires for the surface thermocouples and anchored using Ni-Cr ribbons spot welded in place at AFIT. The surface thermocouple measurements were then used in the IR

calibration method described in Section 3.2.3. All these thermocouples measurements were collected via LabView and output in text files with headers.

The many mass flows were controlled and measured via the mass flow controllers described in Table 3-2. Due to a rolling calibration process and shifting mass flow needs based on test requirements, some flows utilized multiple mass flow controllers over the course of the investigation. Specifically, the coolant supply and boundary layer bleed had different flow controllers at different times during testing. The full scale range of each mass flow controller is expressed in Standard Liters Per Minute (SLPM) of nitrogen, except for the propane controller, which is expressed in SLPM of propane. The LabView software only recorded the freestream flow rate, so the other flow rates were recorded by hand from the appropriate control unit. The film coolant mass flow rate was determined as the difference between coolant gas supply and exhaust flow rates.

Table 3-2: Mass flow controllers

Flow Path	Controller Brand	Controller Model	Full Scale Flow Rate (SLPM)	Accuracy (% of reading)
Boundary Layer Bleed	MKS	1559A	200	+/- 1%
		MC20A	50	+/- 0.25%
Coolant Supply	MKS	MC20A	50	+/- 0.25%
		1559A	200	+/- 1%
		Alta 1480A	30	+/- 1%
Coolant Exhaust	MKS	Alta 1480A	30	+/- 1%
Propane	Brooks	5853i	200 (propane)	+/- 1%
Freestream	Fox Thermal Instruments, Inc.	FT2	3400	+/- 2% (high temp) +/- 3% (low temp)

3.3.1.2. Characteristic Parameters and Performance Metrics

In practice, the characteristic film cooling parameters for this investigation were calculated using modified forms of the equations provided in Section 2.1.2. These forms were still consistent with the definitions of the parameters; they simply enabled easier calculation for this particular experimental setup. Using a process described by Ashby [2], thermophysical properties for gases were estimated by linear interpolation using a table of properties over a large temperature span at a pressure of 101325 Pa. These properties were then applied in the equations discussed below.

The important parameters calculated in this way include the density ratio, blowing ratio, momentum flux ratio, advective capacity ratio, the Reynolds number, and the Prandtl number. These parameters were defined in Section 2.1.2, but they are presented here in terms of measured quantities and constants. Assuming equal pressure for the freestream and coolant gas flows reduced Eq. (2-11) for the density ratio to:

$$DR = \frac{\rho_c}{\rho_\infty} = \frac{P_c}{R_c T_c}\frac{R_\infty T_\infty}{P_\infty} = \frac{R_\infty T_\infty}{R_c T_c} \tag{3-6}$$

This definition of DR requires only temperatures and gas constants, both either measured or calculated as previously described. Likewise, blowing ratio was redefined in terms of mass flow rates and flow path areas

$$M = \frac{\rho_c U_c}{\rho_\infty U_\infty} = \frac{\dot{m}_c}{A_c}\frac{A_\infty}{\dot{m}_\infty} = \frac{\dot{m}_c}{\frac{\pi}{4} d^2 N_{holes}}\frac{H_\infty W_\infty}{\dot{m}_\infty} \tag{3-7}$$

where H_∞ and W_∞ represent the height and width of the freestream channel over the test plate, $\dot{m}$ represents a mass flow rate, and N_{holes} represents the number of film cooling holes. Since the flow path areas were constant for all tests, the blowing ratio was controlled by the ratio of mass flow rates. Momentum flux ratio and advective capacity ratio were then defined in terms of blowing ratio and density ratio.

$$I = \frac{M^2}{DR} \tag{3-8}$$

$$ACR = M\frac{c_{p,c}}{c_{p,\infty}} \tag{3-9}$$

where $c_{p,c}$ and $c_{p,\infty}$ are evaluated at T_c or T_∞ for the appropriate gas or gaseous mixture.

Prandtl number and Reynolds number were calculated for both the freestream and coolant gas flows. The thermophysical properties were calculated at T_c or T_∞ as needed. In addition, Reynolds number is redefined to make use of measured mass flow rates

$$Pr = \frac{\mu c_p}{k} \tag{3-10}$$

$$Re = \frac{\rho U x}{\mu} = \frac{\dot{m}}{A}\frac{x}{\mu} \tag{3-11}$$

The value of *x* was the airfoil leading edge diameter, D, for the freestream Reynolds number. For the coolant Reynolds number, *x* was the cooling hole diameter, d.

3.3.2. PSP Setup

The PSP testing method required different equipment and data processing methods than IR testing. This section provides a broad view of both the data collection and processing halves of the PSP portion of this investigation. Equipment required strictly for PSP testing included an Imperx Bobcat CCD camera, a laptop with the related acquisition and post-processing software, and a pair of 400 nm LED illumination sources provided by ISSI. The PSP equipment was positioned upon an 80/20 bar mounting structure, as shown in Figure 3-31.

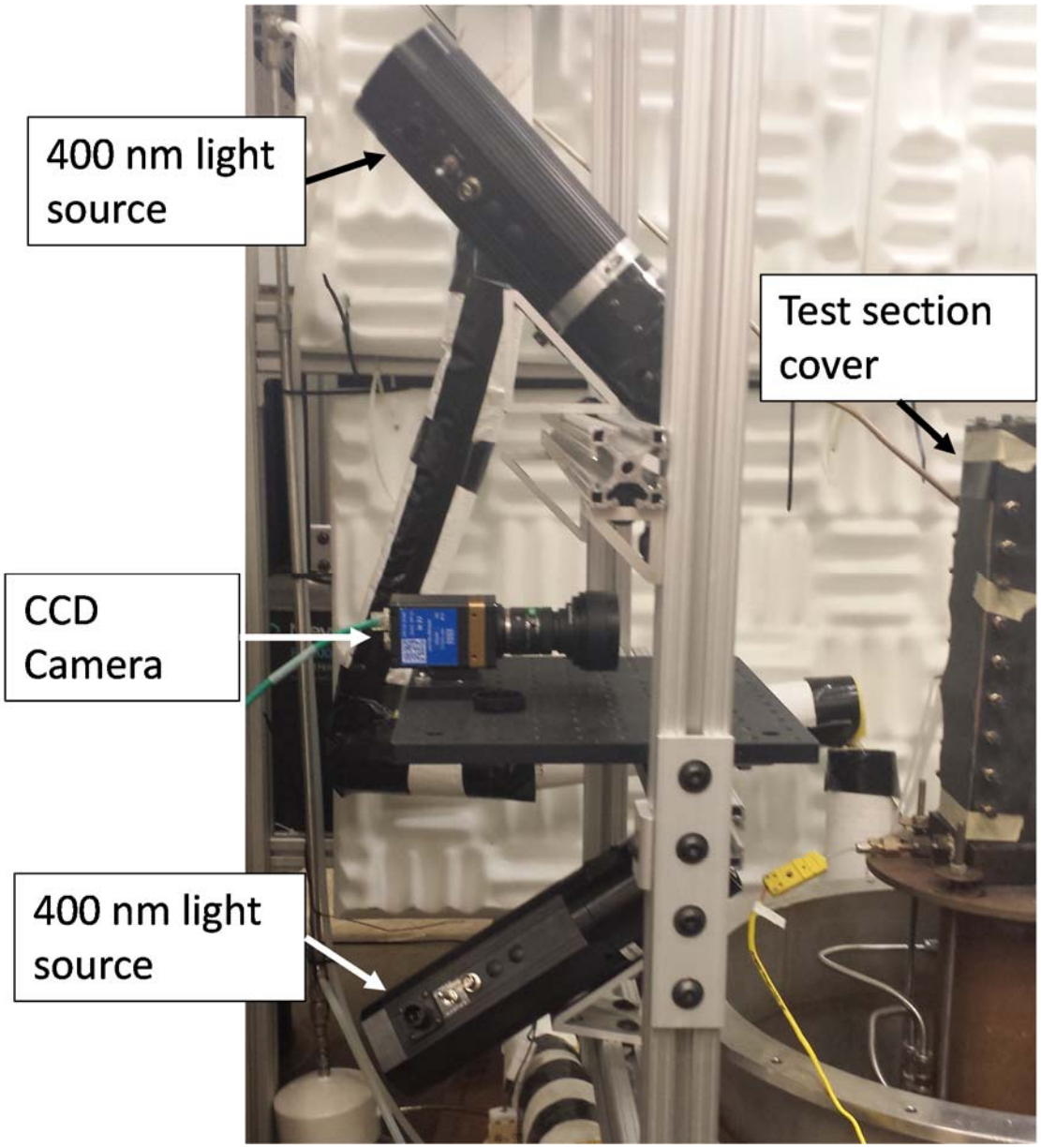

Figure 3-31: PSP test setup

A test section cover was employed to protect the test plate from light exposure in between tests, because the pressure-sensitive paint can photodegrade under ambient light. A 35 mm lens was used with an optical filter to minimize the amount of 400 nm excitation light picked up by the CCD camera. A rectangular quartz window allowed the CCD camera to view a larger region of the test plate than is normally visible through the sapphire windows used during IR testing. The

longer window also enabled the 400 nm excitation light to be shined upon the test plate at an oblique angle to minimize the amount of excitation light reflected into the camera.

Data were acquired through the ISSI ProAcquire program installed on the aforementioned laptop. Once the appropriate test and reference images were acquired, they were processed into pressure fields using the ISSI OMS ProImage program, also installed on the aforementioned laptop. An in-house MATLAB program, created by Ashby [2], was then capable of processing these pressure fields into adiabatic effectiveness distributions, via calculations described in Section 2.5.3.

3.3.3. IR Thermography Setup

For the thermal tests, a sliding mount was constructed to hold the IR camera, allowing it to be placed closer to the rig than in previous investigations. This modification, shown in Figure 3-32, was made in an effort to increase the spatial resolution of the camera. However, the focusing limits of the lens and heat considerations at high temperature prevented the modifications from having a measureable improvement. After primary testing was completed, a series of lens spacer rings for the IR camera were tested, which allowed the camera to be placed within 30 centimeters of the test section and still focus on the test piece. At that distance, the resolution could be improved from the usual 4-5 pixels per hole diameter to about 15 pixels per hole diameter. This placement merits further inquiry, although it would necessitate a heat shield for the camera during high temperature testing. A Boekel Industries, Inc. laboratory jack was used alongside various bracers to minimize the vibration produced by the incorporated cooling system of the IR camera.

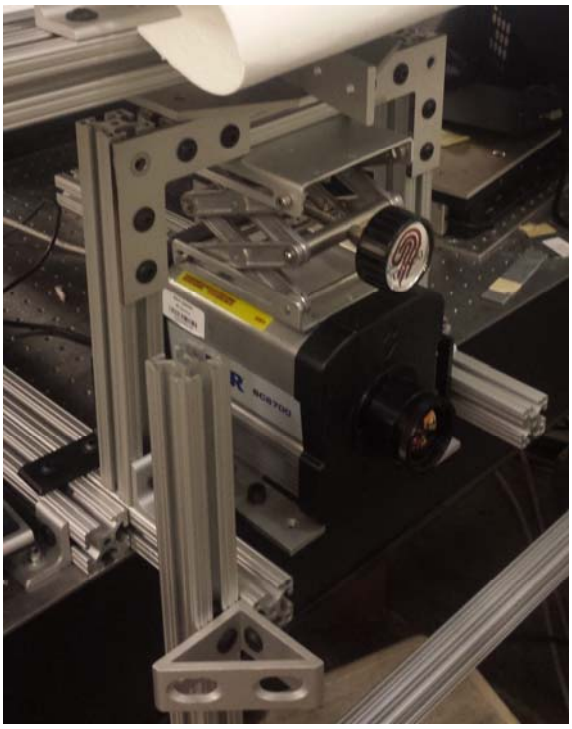

Figure 3-32: IR camera in sliding mount

Data was acquired from the IR camera via the FLIR ExaminIR program. The images taken by the camera were exported as matrices of intensity values and averaged over the two-second recording time. LabView values for relevant thermocouple temperatures and freestream flow were then averaged over five data points collected in tandem with the IR recording. Finally, the mass flow rates from the MKS controllers for the propane, boundary layer bleed, coolant supply, and coolant exhaust were placed into a data file. These pieces of data were then processed via an in-house MATLAB program adapted from Ashby [2] to generate distributions of overall effectiveness. Finally, graphs of specific *x/d* and *y/d* positions within these ϕ distributions were generated with an in-house MATLAB program developed for this investigation.

3.4. Experimental Uncertainty

For this investigation, experimental uncertainty was determined to help quantify the accuracy of the film cooling effectiveness calculated from experimental data. Uncertainty can stem

from measurement precision and repeatability. Section 3.4.1 briefly discusses the concepts of measurement uncertainty and applies them to representative low and high temperature data. Section 3.4.2 discusses the repeatability of overall effectiveness measurements in the FCR at low temperature.

3.4.1. Measurement Uncertainty

The constant odds, root-sum-square method described by Moffat [49] was used to assess the uncertainty that the precision of experimental measurements created in this investigation.

$$\delta Z = \left[\sum_{i=1}^{N}\left(\frac{\partial Z}{\partial X_i}\delta X_i\right)^2\right]^{\frac{1}{2}} \tag{3-12}$$

where Z is the parameter of interest; X is a variable of the parameter, Z; and δ represents the uncertainty of the variable or parameter of interest.

In this investigation, the focus was placed on the impact of temperature measurement uncertainties on the uncertainty of the calculated overall film cooling effectiveness. This uncertainty was assessed at representative near engine and near ambient temperature conditions by using the manufacturer-reported accuracy of the various measurement devices. Table 3-3 summarizes the raw measurements used for this analysis at low and high temperature. On-site mass flow controller calibrations brought them within the uncertainty values published by the manufacturer. The accuracy of the surface temperature measurement was modified to include the residuals from the calibration curve fit, discussed in Section 3.2.3. This correction should account for any uncertainties introduced during the calibration process from temperature sampling location, window fogging, potential hysteresis, etc.

Table 3-3: Uncertainty Analysis Representative Values

Measurement	Low Temperature	High Temperature	Uncertainty
$\dot{m}_{\infty}$ (kg/min)	0.4	0.8	+/- 1%
$\dot{m}_{BLB}$ (kg/min)	0.027	0.025	+/- 1%
$\dot{m}_{c,in}$ (kg/min)	0.0036	0.0083	+/- 1%
$\dot{m}_{c,out}$ (kg/min)	0.0018	0.0042	+/- 1%
T_{∞} (K)	420	1300	+/- 0.75%
T_c (K)	370	840	+/- 0.75%
T_s (K)	390	1025	+/- 1.19% (cold), 1.15% (hot)

From these representative conditions, the approximate uncertainty was computed for the parameters shown in Table 3-4. Note that *DR*, *I*, and Re_{∞} uncertainties were computed using applied equations in Section 3.3.1, rather than their definition equations from Chapter 2. The uncertainty is notably lower for *DR* and Re_{∞} than for the other parameters because there are only two measurements involved in calculating each of them. In contrast, *M* is affected by four measurements: the freestream, boundary layer, coolant in, and coolant out mass flows. Since most of the uncertainty values provided by manufacturers are listed as a percent of the measurement, the uncertainty does not change much between low and high temperature. The major exception is ϕ, because it is affected by the surface temperature measurement, which has more uncertainty at low temperature due to the relative magnitude of the calibration curve residuals. The uncertainty of the surface temperature measurement plays such an important role in the overall effectiveness uncertainty because T_s is subtracted from a value of similar magnitude in the numerator of Eq. (2-2). The freestream temperature uncertainty also plays a large role, because it appears in both the numerator and denominator of the overall effectiveness.

Table 3-4: Uncertainty in important non-dimensionalized parameters

	Low Temperate			High Temperature		
Parameter	**Value**	**Uncertainty**	**Percentage**	**Value**	**Uncertainty**	**Percentage**
M	1.68	0.042	2.48	1.84	0.046	2.49
DR	1.72	0.013	0.75	1.57	0.012	0.75
I	1.64	0.082	5.02	2.16	0.109	5.04
ACR	1.52	0.038	2.51	1.73	0.039	2.28
Re_∞	4726.9	47.7	1.01	4554.9	44.6	0.98
ϕ	0.60	0.101	16.91	0.60	0.028	4.72

3.4.2. Repeatability Measurements at Low Temperature

To assess the repeatability of overall effectiveness measurements, some of the data points described in Section 4.3.1 were taken a second time 11 days after the initial testing. The second set of tests sought to match all of the test parameters from the first set as closely as possible. Table 3-5 shows the test points and the variations in the base parameters between the two days. Points 1a-8a were taken on 06 Jan 2017, while Points 1b-8b were taken on 17 Jan 2017. The coolant mass flows were nearly perfectly matched between the test points, reflecting the level of control that the FCR has over the coolant mass flow. Most of the other parameters regularly see around a 2% change between the two testing days.

Table 3-5: Repeatability comparison points

Point #	Coolant	M	ER	DR	I	ACR	Re_∞	T_c (K)	$\dot{m}_{c,in}$ (kg/min)
1a	CO_2	1.89	3	1.72	2.07	1.71	4455	376.3	7.37×10^{-3}
1b	CO_2	1.89	3	1.70	2.10	1.72	4451	378.0	7.37×10^{-3}
	% Change	0.09	0.00	-1.13	1.32	0.22	-0.1	0.5	0
2a	CO_2	0.94	7	1.70	0.52	0.85	4469	376.0	7.37×10^{-3}
2b	CO_2	0.96	7	1.66	0.56	0.88	4383	383.7	7.37×10^{-3}
	% Change	1.96	0.00	-2.48	6.59	2.71	-1.9	2.1	0
3a	CO_2	1.92	1	1.68	2.20	1.75	4375	383.1	3.69×10^{-3}
3b	CO_2	1.91	1	1.71	2.13	1.73	4399	372.4	3.69×10^{-3}
	% Change	-0.54	0.00	1.90	-2.93	-1.48	0.5	-2.8	0
4a	CO_2	0.96	3	1.70	0.54	0.87	4400	376.6	3.69×10^{-3}
4b	CO_2	0.93	3	1.72	0.51	0.84	4505	371.9	3.69×10^{-3}
	% Change	-2.33	0.00	1.32	-5.85	-2.74	2.4	-1.2	0
5a	CO_2	0.48	7	1.70	0.13	0.43	4413	375.3	3.69×10^{-3}
5b	CO_2	0.46	7	1.72	0.12	0.42	4542	372.0	3.69×10^{-3}
	% Change	-2.84	0.00	1.10	-6.62	-3.13	2.9	-0.9	0
6a	CO_2	1.85	0	1.70	2.02	1.68	4538	374.6	1.84×10^{-3}
6b	CO_2	1.89	0	1.71	2.08	1.71	4459	373.5	1.84×10^{-3}
	% Change	1.77	0.00	0.50	3.06	1.67	-1.7	-0.3	0
7a	CO_2	0.94	1	1.70	0.52	0.85	4456	374.0	1.84×10^{-3}
7b	CO_2	0.95	1	1.71	0.53	0.86	4406	374.3	1.84×10^{-3}
	% Change	1.13	0.00	0.58	1.68	1.12	-1.1	0.1	0
8a	CO_2	0.48	3	1.71	0.13	0.43	4401	373.4	1.84×10^{-3}
8b	CO_2	0.48	3	1.71	0.14	0.44	4368	375.2	1.84×10^{-3}
	% Change	00.75	00.0	-0.03	10.52	0.86	-0.7	0.5	0

The IR data for these points were processed to produce area-averaged overall film cooling effectiveness values ($\bar{\bar{\phi}}$) by averaging the overall effectiveness over an area ten hole diameters long and one span wide centered on one of the two center film cooling holes. This area is the same region used to collect span-averaged values, as discussed in Section 4.2.1. Since these two sets of data were gathered on different days, they used different IR calibrations, produced in the manner described in Section 3.2.3. Figure 3-33 shows the $\bar{\bar{\phi}}$ values for each of the points from Table 3-5, with lines between corresponding points. Between 06 Jan 2017 and 17 Jan 2017 the $\bar{\bar{\phi}}$ values

dropped by an average of 0.095. As discussed in the previous section, this difference was still within the measurement uncertainty for the overall effectiveness for the low temperature regime. If the difference is not due to the measurement uncertainty discussed previously, one potential source is the IR calibration. If the in-situ IR calibration process did not account for external variables as effectively as was assumed, it could impact the results.

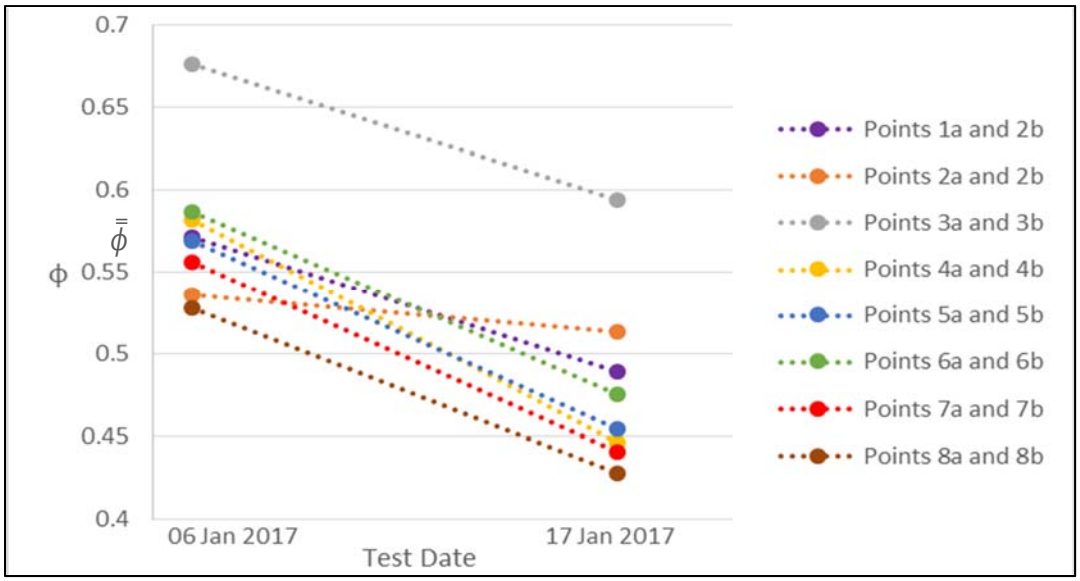

Figure 3-33: Low temperature repeatability data

Figure 3-34 shows a comparison of the IR calibration curves for the two sets of data. The curves are very close at lower temperatures, but they gradually separate. The maximum discrepancy between the two curves at a given intensity readings is 2.38 K. Based on the surface thermocouples, the surface was generally within the range of 8000-10000 counts, where the calibration curves were within 1 K of each other. Ostensibly, these differences should not be a problem; they should be beneficial, accounting for variations in the test conditions between the two days. Future investigations could help determine if the IR calibration process contributes to the observed repeatability issues.

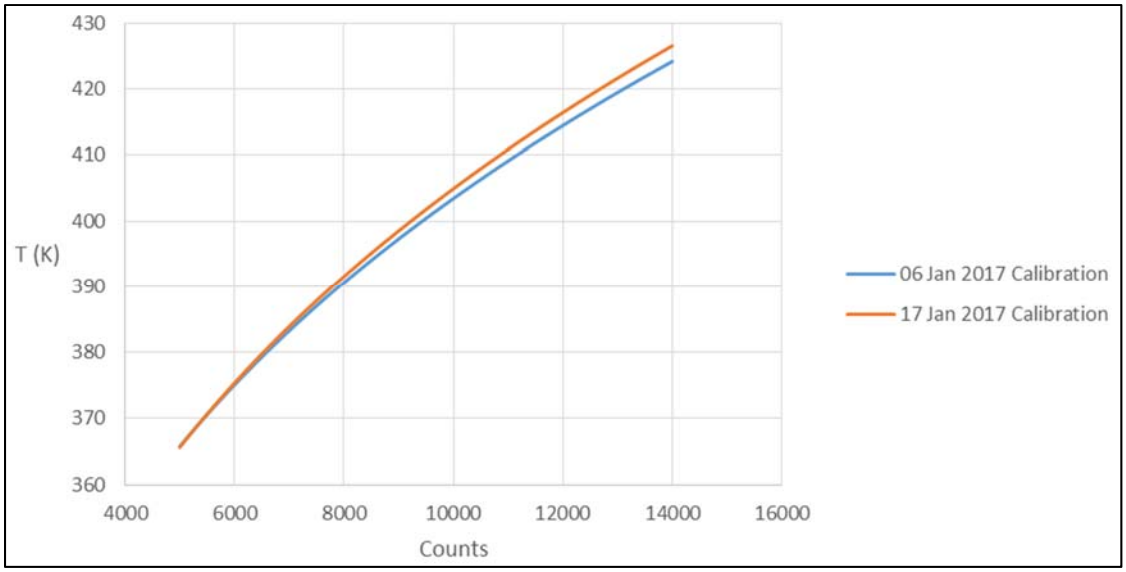

Figure 3-34: Comparison of repeatability calibration curves

Another potential explanation would be an unaccounted variable affecting the overall effectiveness on the surface. As will be discussed in the results, the FCR might experience conduction from the test plate out to the room, leading to lower surface temperatures at all cases. If this hypothesis is correct, temperature changes in the lab could affect the conduction from the rig. Additionally, since the above tests were taken with CO_2 (which is stored outside) the coolant would be colder upon entering the lab on colder days and might maintain that low temperature to the vicinity of the rig. However, thermocouple readings in the room show that there was less than 1 K difference in the lab ambient temperature between the two days. Furthermore, the temperature of the coolant prior to entering the rig does not show any clear correlation with the universal decrease in overall effectiveness on the second day. Future investigations could help clarify if atmospheric or ambient lab temperatures affect the FCR test results. Future work could also seek to quantify the repeatability of tests taken on the same testing day, since such variations were not analyzed in this investigation.

4. Results and Discussion

As outlined before, the objectives of this investigation included comparing the FCR to the LEFCT and comparing low temperature IR tests to high temperature IR tests. Sections 4.1 and 4.2 expound on each of those points, respectively. In the course of comparing low and high temperature IR data, an unusual trend was discovered, wherein a higher coolant temperature seemed to produce a higher overall cooling effectiveness. Section 4.3 discusses additional low temperature experiments that confirm this observed trend.

4.1. PSP and Thermal Investigation of the Test Plate Leading Edge

The first set of experiments performed for this investigation sought to compare measurements from the FCR to measurements from the LEFCT located in AFRL RC-21, with the aid of Second Lieutenant Carol Bryant. A set of data collected on the LEFCT by a previous AFIT student, First Lieutenant Connor Wiese, had a freestream Reynolds number that was low enough (around 10,000) that the FCR was deemed capable of roughly matching the flow conditions. After a comparison of the rig geometries, PSP tests were performed in the FCR with the goal of matching the flow conditions achieved by Lt Wiese. By doing so, the experimental adiabatic effectiveness measurements of both rigs could be compared. If the results were similar, it would suggest that the rigs are sufficiently matched in terms of geometry and flow field to compare future test results against each other. Thermal tests were also planned, but the high conductivity of the airfoil and other affects prevented the desired experiments, as discussed below.

4.1.1. Facility Impact

When seeking to compare the results between the LEFCT and FCR, it is important to note the geometry differences. Most notably, the FCR is approximately one-tenth the scale of the

LEFCT. As previously mentioned, the FCR uses a half-airfoil, whereas the LEFCT has a full airfoil set in the middle of the wind tunnel. The boundary layer bleed on the FCR is used to remove the boundary layer approaching the plate, ostensibly generating an equivalent flow field to the LEFCT. One other difference in the geometry is the area ratio. The area ratio is the ratio of the flow area of the tunnel before the test piece to the minimum flow area, which occurs at the maximum test piece width. The LEFCT has an area ratio of 0.78, whereas the FCR's is about 0.58. That is to say, the airfoil takes up a larger proportion of the test section path in the FCR than in the LEFCT. This greater flow constriction would be expected to result in a higher freestream velocity over the plate, in accordance with continuity. A pair of two-dimensional CFD models were constructed to explore the impact of this change. Both models used the LEFCT geometry, scale, and flow rates from relevant studies by Connor Weise, but with either the LEFCT or FCR compression ratios for comparison. The simulations used the RANS model, with an SST k-omega turbulence model, which does not use wall functions. For all points, y+ < 5. Grid convergence was assessed using the residuals and a surface monitor to determine that the flow over the area of interest reached steady state. Figure 4-1 shows the velocity distributions near the hole positions generated by these models.

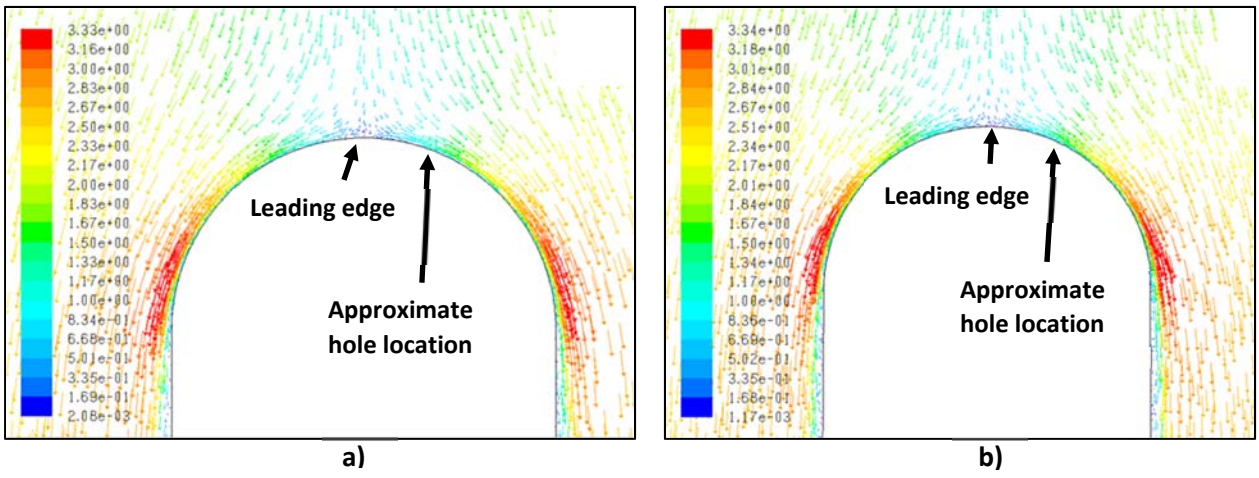

Figure 4-1: Two-dimensional CFD analysis of freestream velocity over the test plate surface for a) LEFCT area ratio b) FCR area ratio

The velocity of the flow was sampled at 1.03 millimeters above the surface at the position of the film cooling holes, which was observed to be just outside the boundary layer of the flow. The velocity varies from 1.32 meters per second at the LEFCT area ratio to 1.34 at the FCR area ratio. Such a small percentage change (1.5%) was deemed to be within acceptable error to run the desired tests.

4.1.2. PSP Results

PSP tests were performed using the experimental setup described in Section 3.3.2, with the goal of matching a set of LEFCT data points collected by Lt Connor Wiese and shown in Table 4-1: LEFCT PSP Test Points. These points were taken near the lower bound of the LEFCT's achievable Reynolds number range, with the goal of reaching conditions that the FCR could match. The test plate had a single cooling hole, with coolant fed in plenum fashion.

Table 4-1: LEFCT PSP Test Points

Point #	Coolant	M	DR	I	Re_∞
1	Argon	0.63	1.42	0.28	9953
2	Argon	1.04	1.42	0.76	9940
3	CO_2	0.57	1.56	0.21	9910
4	CO_2	0.99	1.56	0.63	9902
5	N_2	0.72	0.99	0.52	10105
6	N_2	1.24	0.99	1.55	10072
7	N_2	1.26	0.99	1.60	10098

Some examples of the adiabatic effectiveness profiles generated during these tests are shown in Figure 4-2. These images are oriented with the freestream flowing from left to right. Note the clear outlines of the jet. The tests in the FCR were performed with the goal of assessing if both rigs would produce similar adiabatic effectiveness distributions at matched conditions.

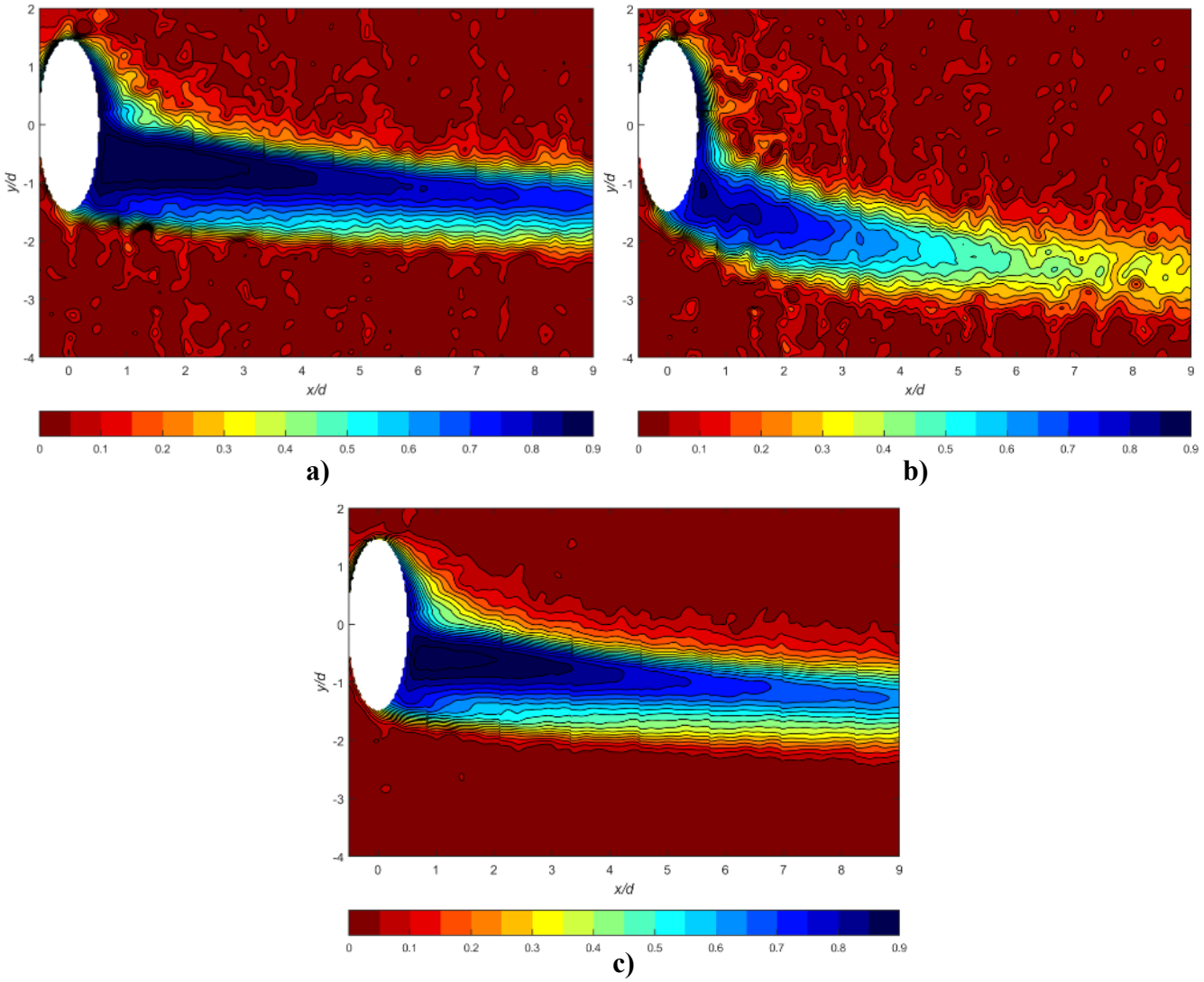

Figure 4-2: LEFCT adiabatic effectiveness distributions at LEFCT points a) 1, b) 3, and c) 5 (provided by Connor Wiese)

Table 4-2 shows the PSP data points that were taken. The highlighted data points were designed to match the LEFCT data points. Unfortunately, this was the first set of data to be taken during this investigation. A series of errors in the calculation code resulted in faulty conversion between kg/min and SLPM units, resulting in slightly higher freestream Reynolds numbers than the target 10,000 and incorrect coolant mass flows. In addition, the amount of coolant mass flow required was initially calculated for a single hole, then multiplied to feed the eight holes on the test

plate. However, this multiplicative factor was erroneously applied twice in the process. These errors led to much higher blowing ratios than desired.

Table 4-2: PSP Data Points

Point #	Coolant	M goal	M actual	DR	I	Re_∞
1	Argon	0.63	2.07	1.42	3.00	12737
2	Argon	1.04	3.45	1.42	8.40	12704
3	CO_2	0.57	2.15	1.56	2.97	12648
4	CO_2	0.99	3.69	1.56	8.74	12738
5	CO_2	1.5	5.71	1.56	20.89	12459
6	CO_2	2	7.57	1.56	36.69	12539
7	CO_2	2	7.47	1.65	33.79	12706
8	CO_2	2.5	9.25	1.56	54.90	12817
9	N_2	0.5	1.19	0.99	1.42	12561
10	N_2	0.72	1.68	0.99	2.86	12803
11	N_2	1	2.36	0.99	5.62	12636
12	N_2	1.24	2.91	0.99	8.55	12696
13	N_2	1.26	2.95	0.99	8.80	12718

Figure 4-3 shows pressure profiles at the leading edge for various points with different momentum ratios and coolant gases for comparison. These pressure profiles display the distribution of the partial pressure of oxygen across the test plate surface, thereby revealing the coolant distribution across the surface as well. Points 8 and 10 were especially chosen because they possess the highest and lowest *I* values, respectively. Note that the freestream flows from right to left in these images, and that the post-processing software did not allow for easy modification of the pressure scale dimensions, so the scales are not identical between pictures. As expected, many of the coolant holes show signs of jet separation, as evidenced by shortened or absent regions of reduced O_2 partial pressure along the test plate surface. For many of the coolant jets on Point 8, they separate so completely and immediately that their effect on the surface is barely visible. Additionally, two jets produce noticeably longer profiles than the other jets. The

coolant mass flow rate for Point 8 was in excess of 20 SLPM, so it is possible that the coolant was beginning to flow non-uniformly at such a high mass flow, as discussed in Section 3.1.

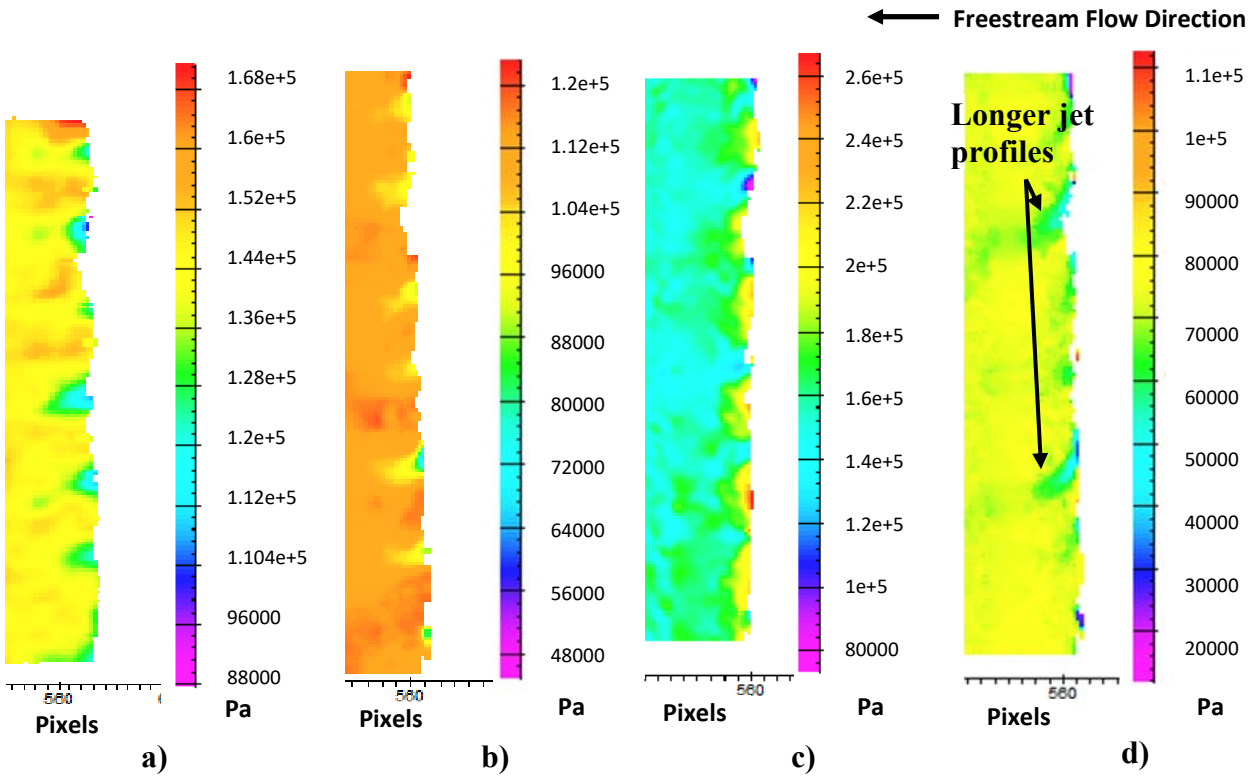

Figure 4-3: Pressure profiles for a) Point 1 (Argon, I = 3), b) Point 4 (CO_2, I = 8.74), c) Point 10 (N_2, I = 2.86), d) Point 8 (CO_2, I = 54.9)

Due to time constraints and the inapplicability of this data for comparison with the LEFCT data, this material was not processed further. However, these experiments did highlight that the FCR is capable of reaching freestream Reynolds numbers within the testing capabilities of the LEFCT and can match typical LEFCT density ratios. Within the data gathered by the FCR, the CO_2 points show consistently lower O_2 partial pressures, which indicates better performance. This result is most likely due to the higher density ratio of the CO_2 cases. Likewise, lower *I* values displayed less jet separation, which is expected.

4.1.3. Leading Edge Thermal Phenomena

A few thermal investigations were made on the leading edge plate. The initial plan was to repeat the same series of points as shown above in Table 4-1. The plan was to compare the overall effectiveness distributions with the adiabatic effectiveness distributions determined by the PSP tests and similar IR measurements made with the LEFCT by Lt Carol Bryant. Table 4-3 shows the test matrix for the LEFCT IR tests.

Table 4-3: LEFCT IR Tests Points

Point #	Coolant	M	DR	I	Re_∞
1	Argon	0.63	1.42	0.28	10128
2	Argon	1.04	1.42	0.76	10145
3	CO_2	0.57	1.56	0.21	9816
4	CO_2	0.96	1.56	0.59	9930
5	N_2	0.73	0.99	0.54	9481
6	N_2	1.25	0.99	1.57	9423
7	N_2	1.26	0.99	1.59	9552

Figure 4-4 shows the overall effectiveness distributions corresponding to the LEFCT PSP images from Figure 4-2. These tests were taken with the exact same test piece as the PSP tests, with a single cooling hole fed in plenum fashion. The path of the coolant jet is quite discernible on the surface of the Corian test plate, at a Biot number of 1.40. The effects of the test plate conductivity and internal cooling are clearly seen in the almost uniform temperature distribution across the surface.

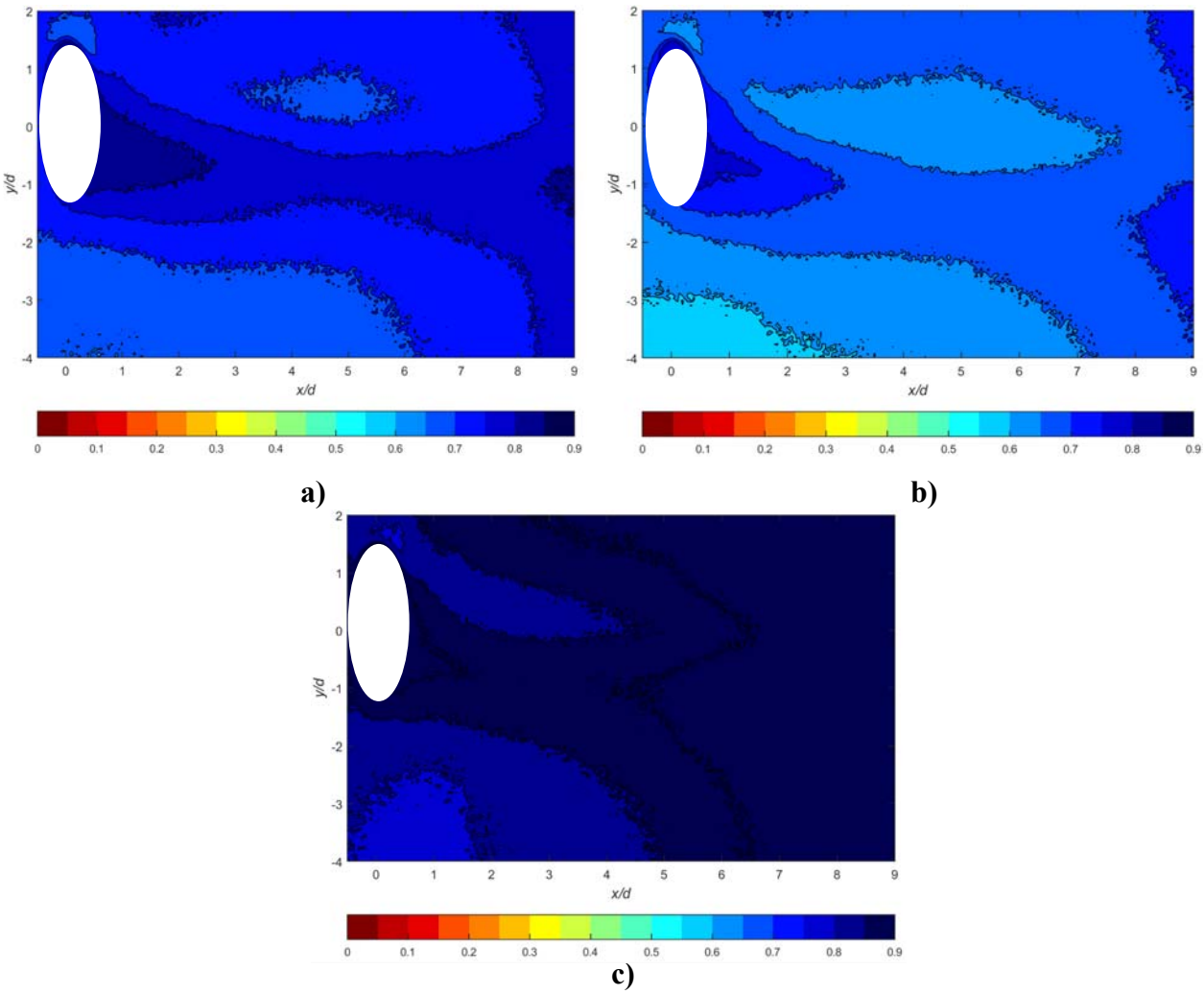

Figure 4-4: LEFCT overall effectiveness distributions at Point a) 1, b) 3, c) 5 (provided by Carol Bryant)

When these test conditions were attempted in the FCR, the coolant had no visible impact due to the high conductivity of the Hastelloy test plate, at an approximate Biot number of 0.14. A series of cases were run, simply to find temperature differences that could generate useful data. Table 4-4 shows a test matrix of those points. Note that all values are estimated, because full data collection was not performed during these simple shakedown tests.

Table 4-4: Estimated leading edge IR points

Point #	Coolant	M	ER	DR	I	Re_∞
1	Air	1	1	0.81	1.23	9950
2	Air	1	2	0.81	1.23	9950
3	Air	1	3	0.81	1.23	9950
4	Air	1	4	0.81	1.23	9950
5	Air	1	5	0.81	1.23	9950
6	Air	1.5	5	0.81	2.78	9950
7	Air	0.5	5	0.81	0.31	9950

These tests were taken with heated air "coolant" at about 370K and ambient freestream conditions to achieve a larger temperature difference. They were also run without the front plate to avoid any possible window effects, which were still under investigation at that time. During the course of these ad hoc tests, some interesting phenomena were observed, as illustrated by the raw IR images in Figure 4-5.

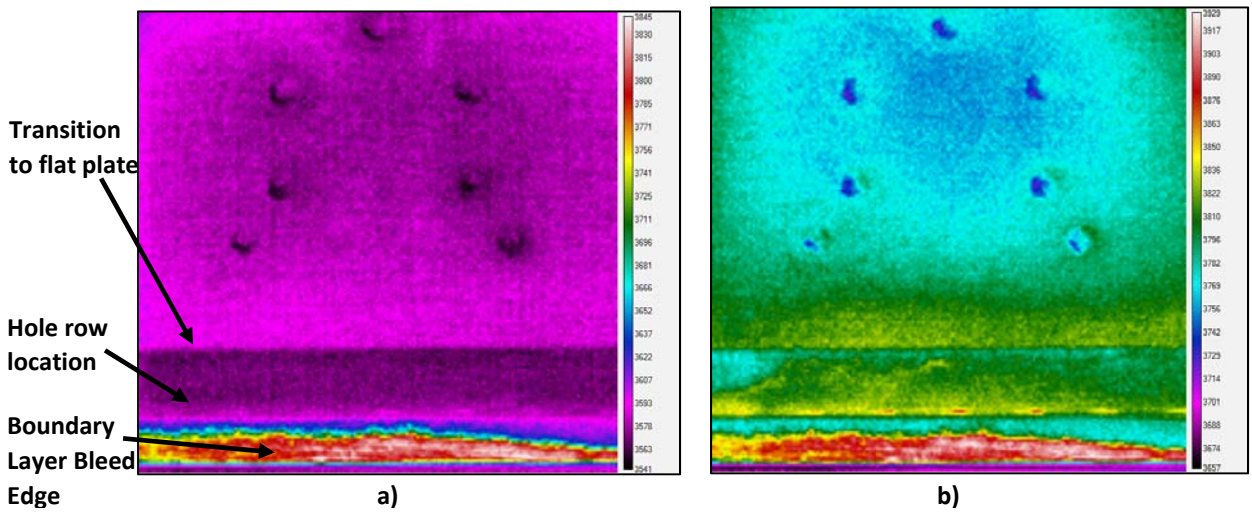

Figure 4-5: Leading edge test plate at ambient freestream a) T_c = 370K, M = 1, ER = 1 b) T_c = 370K, M = 1, ER = 4

Firstly, the transition between the leading edge and the flat plate was observed to be quite sharp. A more gradual transition was expected. Even with the coolant temperature at approximately 370K with an ambient freestream, the holes along the front surface are not even

visible at the lowest coolant flow rate. Increasing the coolant flow rate led to an odd distribution. The data seems to suggest that the coolant impinges on the inside of the flat portion of the plate just past the transition. Although fascinating, questions about the leading edge phenomena were tabled for later investigation. It is currently hypothesized the discontinuity between the leading edge and the flat portion of the test plate could be related to the sharp machining seam generated by the CNC machining process used to manufacture the plates.

4.2. Near Ambient and Near Engine Thermal Matching Tests

This part of the investigation used the shaped hole airfoil, with the goal of matching *M*, *DR*, and freestream *Re* at multiple test conditions between low and high temperatures. As discussed in Chapter 2, these parameters are commonly used to compare film cooling experiments. However, despite using identical geometries and test equipment, the *Bi* changed between low and high temperatures. The cause and impact of this change is discussed in Section 4.2.3. The data from both low and high temperature tests are presented and discussed below, followed by a comparison of results from the two temperature regimes.

4.2.1. Low Temperature

The first set of IR thermography data was extensive. Air, argon, and CO_2 were all employed as coolant gases during various tests in this data set, as shown in Table 4-5. The points within each highlighted band were fed with the same total coolant flow, but with different coolant exhaust mass flows to vary the blowing ratio, as discussed in Section 3.1.3. This method made it easier to maintain a relatively steady coolant temperature over the points within each band. The Prandtl numbers are not listed in the table, because they are nearly constant over these small temperature changes. The *Pr* of air at both the coolant and freestream temperatures was about 0.70, while the *Pr* values for the argon and CO_2 coolant were 0.68 and 0.74, respectively.

Table 4-5: Low Temperature Data points, Set 1

Point #	Coolant	M goal	M actual	ER	DR	I	ACR	Re_∞	T_c (K)	$\dot{m}_{c,in}$ (kg/min)
1	Air	2	1.93	3	1.17	3.18	1.92	4415	358.4	7.46×10^{-3}
2	Air	1	0.99	7	1.17	0.84	0.98	4303	358.3	7.46×10^{-3}
3	Air	0.5	0.48	15	1.17	0.20	0.48	4421	362.8	7.46×10^{-3}
4	Air	1	0.97	3	1.15	0.81	0.96	4411	363.3	3.72×10^{-3}
5	Air	0.5	0.49	7	1.15	0.21	0.49	4348	363.6	3.72×10^{-3}
6	Air	2	1.97	0	1.14	3.40	1.96	4325	367.0	1.87×10^{-3}
7	Air	1	0.97	1	1.14	0.82	0.96	4411	367.6	1.87×10^{-3}
8	Air	0.5	0.49	3	1.14	0.21	0.49	4317	368.0	1.87×10^{-3}
9	Air	1	0.94	0	1.14	0.77	0.93	4533	369.3	9.33×10^{-4}
10	Argon	8	7.47	0	1.59	35.14	3.83	4400	364.2	7.21×10^{-3}
11	Argon	2	1.91	3	1.59	2.30	0.98	4303	364.9	7.21×10^{-3}
12	Argon	1	0.98	7	1.59	0.61	0.50	4179	365.4	7.21×10^{-3}
13	Argon	0.5	0.48	15	1.59	0.14	0.24	4298	365.8	7.21×10^{-3}
14	Argon	2	1.88	1	1.58	2.23	0.96	4379	367.7	3.60×10^{-3}
15	Argon	1	0.95	3	1.58	0.57	0.49	4321	368.5	3.60×10^{-3}
16	Argon	0.5	0.46	7	1.58	0.13	0.24	4452	369.2	3.60×10^{-3}
17	Argon	2	1.82	0	1.57	2.12	0.93	4509	370.8	1.80×10^{-3}
18	CO_2	2	1.88	3	1.76	2.01	1.68	4470	362.6	7.37×10^{-3}
19	CO_2	1	0.94	7	1.76	0.50	0.84	4464	362.8	7.37×10^{-3}
20	CO_2	0.5	0.48	15	1.76	0.13	0.43	4419	364.5	7.37×10^{-3}
21	CO_2	2	1.99	1	1.75	2.26	1.78	4232	363.9	3.69×10^{-3}
22	CO_2	1	0.93	3	1.75	0.50	0.84	4506	364.4	3.69×10^{-3}
23	CO_2	0.5	0.48	7	1.75	0.13	0.43	4417	364.7	3.69×10^{-3}
24	CO_2	2	1.89	0	1.73	2.06	1.70	4456	367.6	1.84×10^{-3}
25	CO_2	1	0.95	1	1.73	0.52	0.85	4449	368.4	1.84×10^{-3}
26	CO_2	0.5	0.48	3	1.73	0.13	0.43	4373	368.6	1.84×10^{-3}
27	CO_2	1	0.96	0	1.72	0.54	0.87	4364	370.1	9.21×10^{-4}

Figure 4-6 shows examples of air and CO_2 overall effectiveness distributions at similar conditions. Note the generally higher effectiveness values in the CO_2 case. To more easily compare the information represented in those images, values of ϕ were collected along the centerline of the lower of the two central coolant holes, as shown in Figure 4-7.

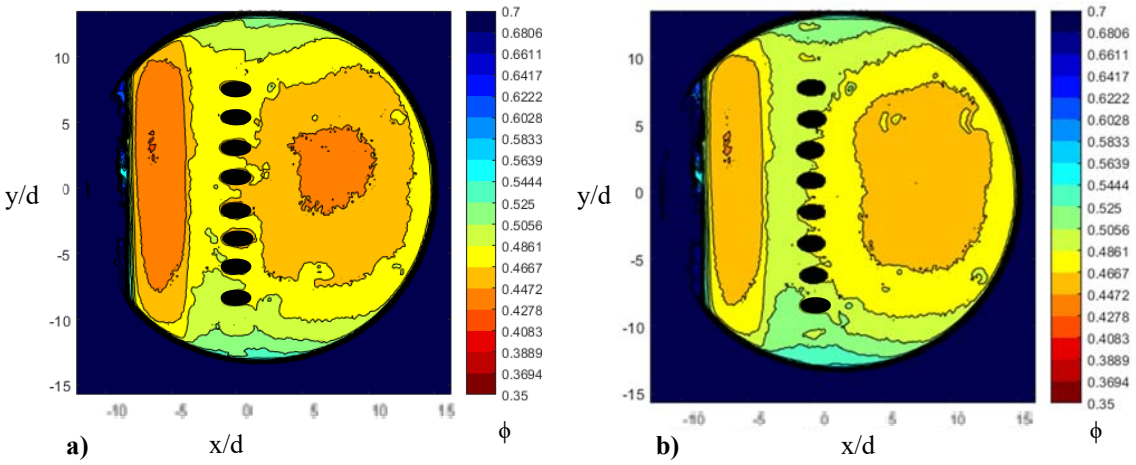

Figure 4-6: Overall effectiveness distributions for set 1 Points a) 11 and b) 18

Span-averaged values were also taken from y/d = -2 to y/d = 2, which is equivalent to one pitch, centered on the same line as the centerline values. As seen in Figure 4-7, the span-averaged and centerline values are almost identical, except for the region close to the coolant hole. The span-averaged values present a smoother curve, they will be used to discuss overall effectiveness from this point forward.

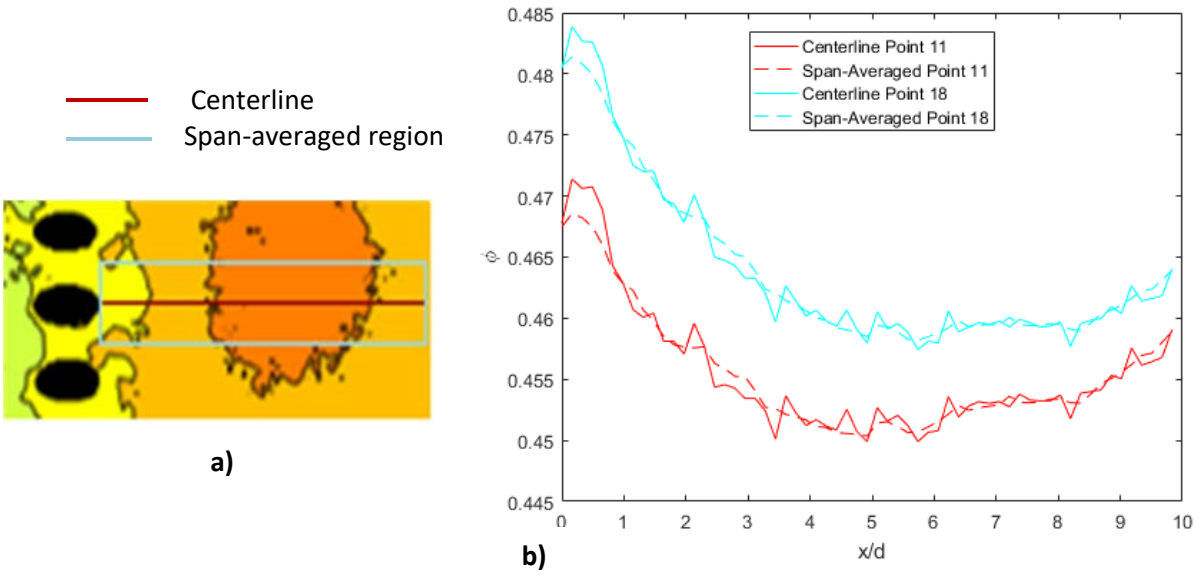

Figure 4-7: Comparison of centerline and span-averaged values

Span-averaged overall effectiveness values for all of the data points in Set 1 are shown in Figure 4-8. Note that for these graphs the solid, dashed, and dotted lines are used for nominal M values of 2, 1, and 0.5 respectively. Likewise, points on each graph with matching total coolant mass flows have the same color. For air, Points 1 and 6 both produce lower overall effectiveness values than Points 2 and 7. The only difference between these points is the higher blowing ratio at Points 1 and 6, suggesting that those jets experienced separation at the higher I corresponding to a blowing ratio of 2. Neither argon nor CO_2 show evidence of separation, with the exception of the extremely high blowing ratio (M = 8) at Point 10. Disregarding separated cases, the overall effectiveness tends to rise with blowing ratio, again with some unexplained exceptions at Points 16 and 20.

Almost all cases display higher effectiveness near the coolant hole, as expected. The effectiveness then drops off towards the middle of the plate, before arcing back up towards the end of the measurement region. The pattern could be induced by some minor amount of reflection from the window, despite the precautions described in Chapter 3. A reflection would artificially raise the IR counts in the center of the window.

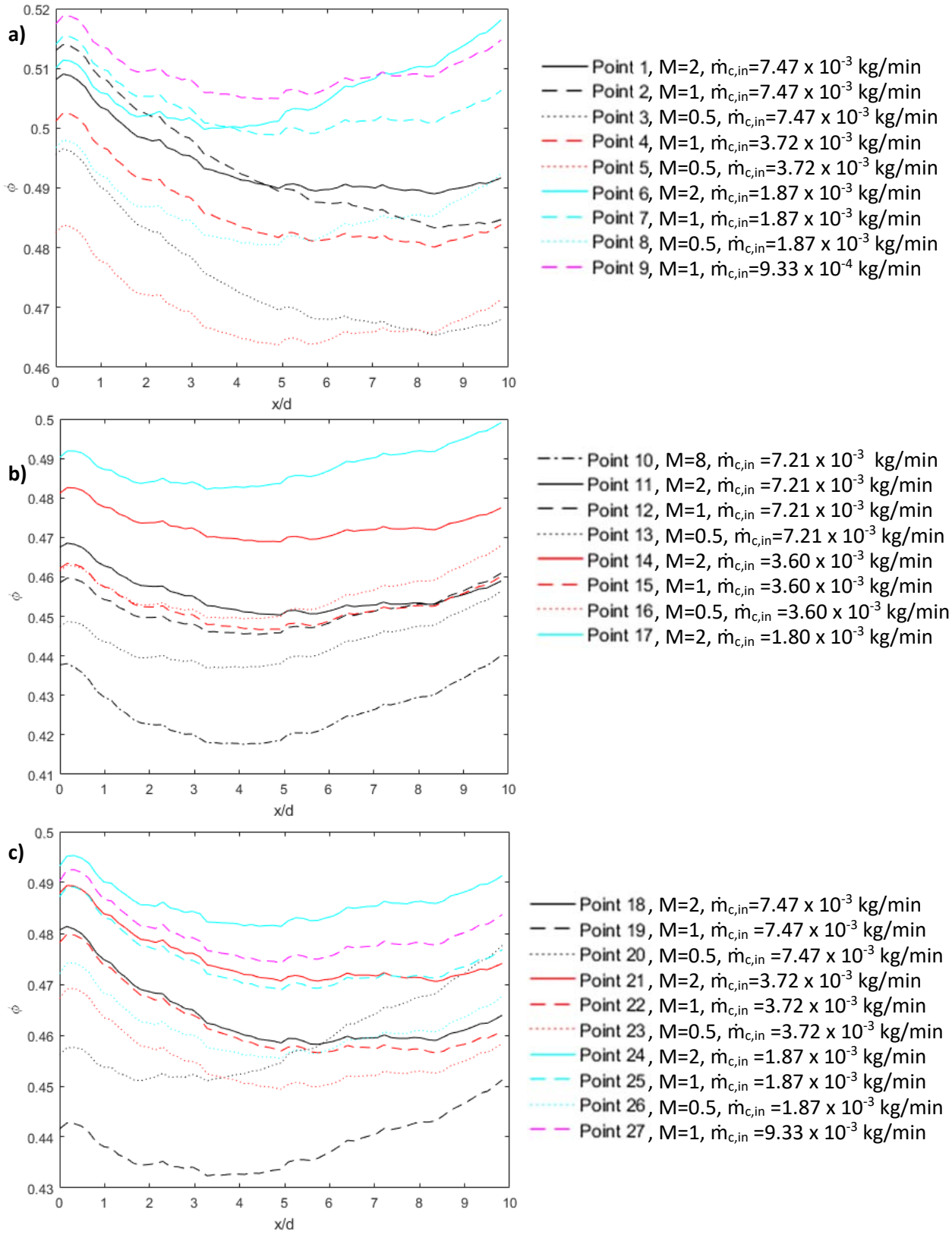

Figure 4-8: Low temperature points in set 1 for a) air, b) argon, c) CO_2

Another noticeable trend visible in Figure 4-8 is that the measured overall effectiveness increases as the total coolant mass flow decreases. For example, out of the CO_2 data points, Point 24 has the highest overall effectiveness of all the M = 2 cases, despite having the lowest total coolant mass flow. Likewise, at $M = 1$ on the CO_2 plot, Points 27, 25, 22, and 19 rank in that order for highest to lowest effectiveness, which is exactly opposite of their total coolant mass flows. The only exception to this general trend of effectiveness to coolant mass flow is the placement of Points 1-3 for air. This trend is unexpected, as a higher internal coolant mass flow should lead to more internal convection, which should cool the test plate more than a lower mass flow case. Table 4-5 shows that the coolant temperature decreases at higher coolant mass flows, as described in Section 3.1.3. Although a lower coolant temperature would be expected to increase the amount of cooling (and does actually reduce the surface temperature), the cooling scheme does not reduce the surface temperature proportionally to the coolant temperature, leading to a lower overall effectiveness by Eq. 2-2. Later experiments sought to examine this effect, as discussed in Section 4.3.2.

Comparing points with different coolant species also reveals some interesting information. Figure 4-9 shows the set 1 points at the three most prevalent total coolant mass flows. In general, the CO_2 points tend to have a higher overall effectiveness than the comparable argon points, due to CO_2's much higher *ACR* values. Also, the higher *ACR* of the air points produces consistently higher overall effectiveness values than the CO_2 points at the same *M*, even though the air points have a much lower *DR* and higher *I*.

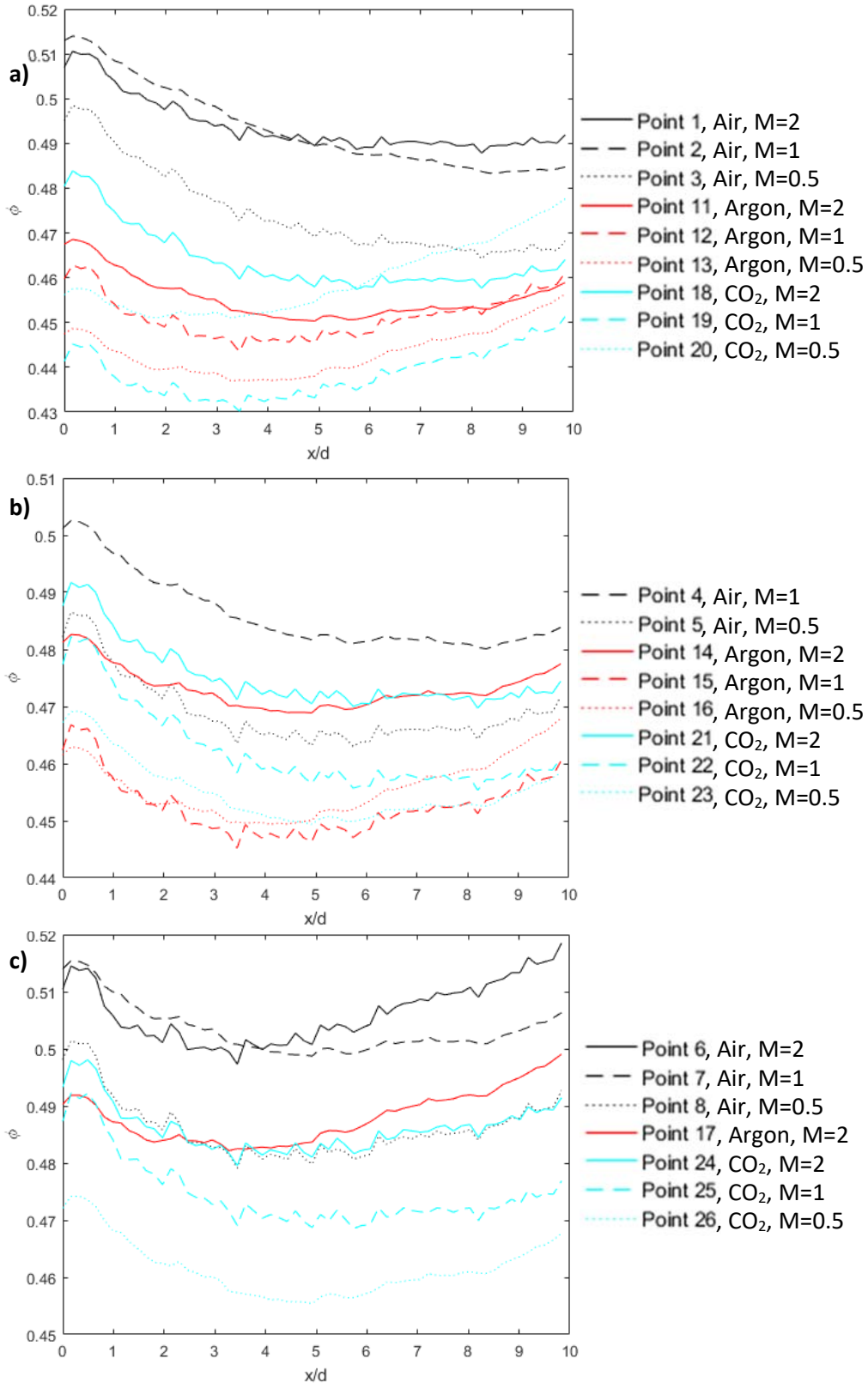

Figure 4-9: Low temperature set 1 points at total coolant mass flow a) 7.3 x 10^{-3} kg/min, b) 3.6 x 10^{-3} kg/min c) 1.8 x 10^{-3} kg/min

In general, the overall effectiveness was not very sensitive to changes in the listed parameters. All of the overall effectiveness measurements lie between 0.43 and 0.52, which is technically within the calculated uncertainty at these low temperatures. Thusly, conclusions drawn from the data must be considered in that light. However, many of the trends discussed above also appeared in the high temperature data, discussed in the next section.

4.2.2. High Temperature

Once the low temperature tests were completed, high temperature tests were performed with similar blowing ratios, density ratios, and freestream Reynolds numbers as the low temperature data. These data points are shown in Table 4-6. Once again, the shaded points are grouped by coolant mass flow. As discussed in Chapter 3, the coolant temperature is heavily affected by the coolant mass flow during high temperature tests, as is shown in the table. Again, *Pr* is not listed because it is approximately 0.70 for air, even at this temperature range.

Table 4-6: High Temperature Data Points

Point #	Coolant	M goal	M actual	ER	DR	I	ACR	Re_∞	T_c (K)	$\dot{m}_{c,in}$ (kg/min)
1	Air	2	2.00	1	1.55	2.57	1.87	4646	839.0	8.30×10^{-3}
2	Air	1	0.99	3	1.55	0.63	0.93	4681	840.4	8.30×10^{-3}
3	Air	0.5	0.50	7	1.55	0.16	0.47	4644	841.4	8.30×10^{-3}
4	Air	2	1.97	0	1.48	2.61	1.86	4711	876.3	4.15×10^{-3}
5	Air	1	1.00	1	1.48	0.67	0.94	4659	880.7	4.15×10^{-3}
6	Air	0.5	0.49	3	1.47	0.16	0.46	4725	882.9	4.15×10^{-3}
7	Air	1	0.98	0	1.45	0.66	0.93	4755	899.1	2.08×10^{-3}
8	Air	0.5	0.49	1	1.44	0.17	0.47	4696	902.7	2.08×10^{-3}
9	Air	2	2.00	3	1.68	2.38	1.85	4642	775.4	1.66×10^{-2}
10	Air	1	1.00	7	1.67	0.60	0.92	4647	777.6	1.66×10^{-2}
11	Air	0.5	0.50	15	1.67	0.15	0.46	4628	779.7	1.66×10^{-2}

Figure 4-10 shows example overall effectiveness distributions for Point 1 and Point 9, the $M = 2$ points from the two highest coolant mass flows. Note the large amount of conduction visible in the images. The surface temperature is nearly uniform across the span at $x/d = 0$. It is also apparent that the lower coolant mass flow case (Point 1) produced higher values of overall effectiveness. The arcing feature near the bottom of the picture is a light smudge on the IR window. The location chosen to gather the span-averaged values were adjusted to the upper middle coolant hole to avoid the smudged region.

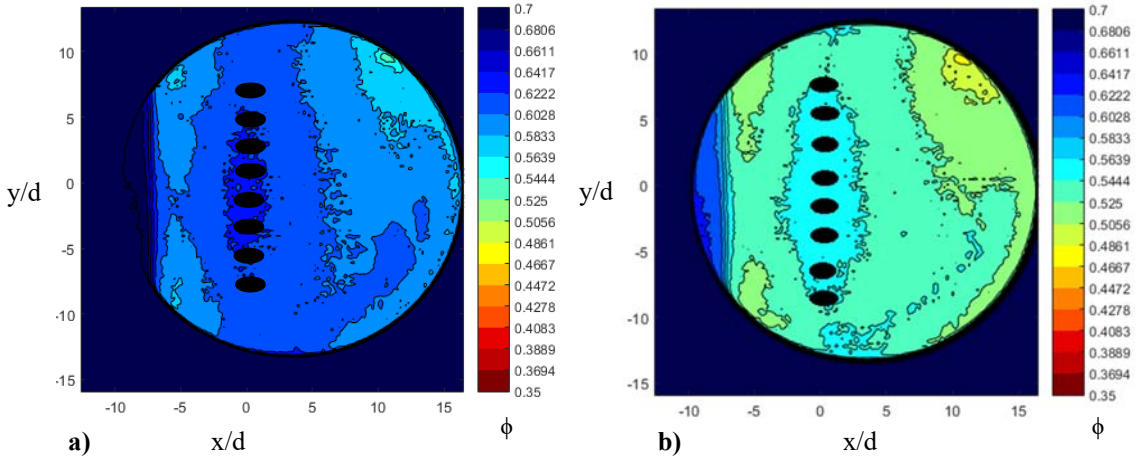

Figure 4-10: High temperature IR images at a) Point 1, b) Point 9

The high temperature data points are sorted by total coolant mass flow in Figure 4-10. The overall effectiveness once again rises at lower total coolant mass flows. Point 1 is the sole exception to the trend, with a very high overall effectiveness of approximately 0.62. There is not a readily apparent explanation as to why. The data mostly follows the trend of higher effectiveness with higher blowing ratio, although Point 4 is an exception. Point 4 also has the highest I value of any of the high temperature points.

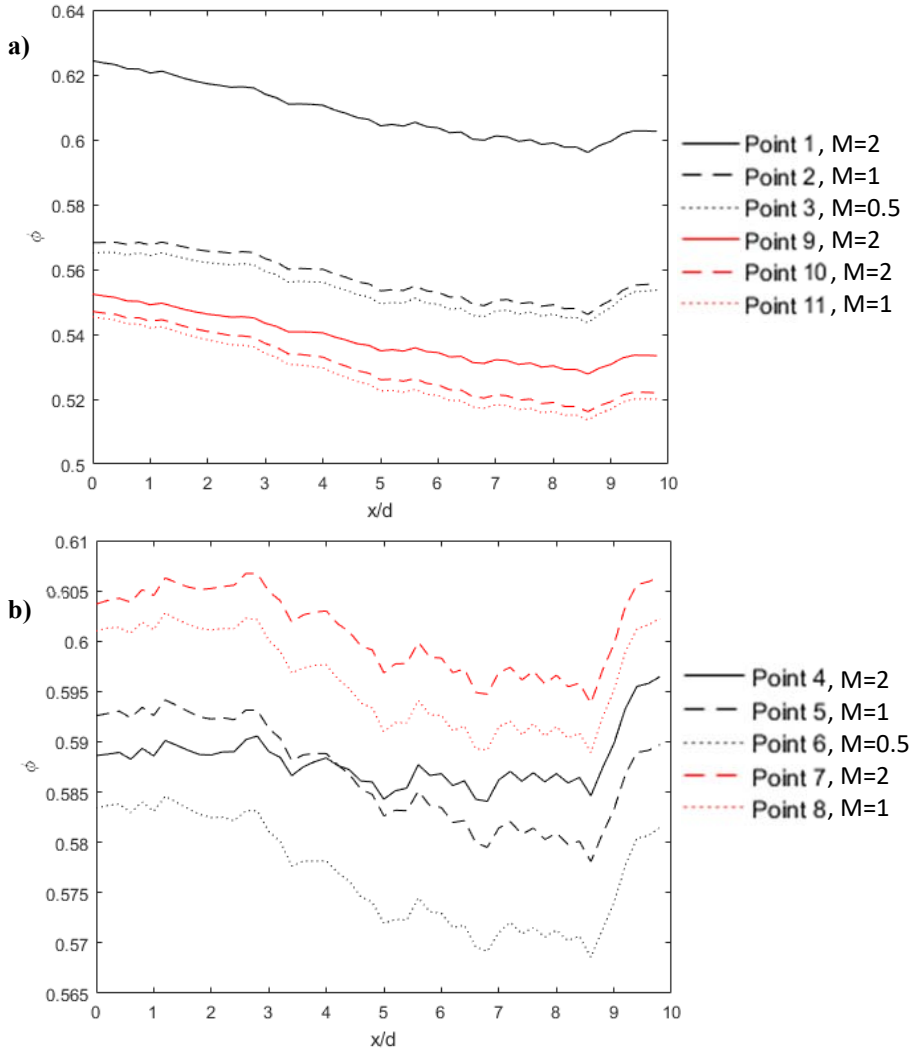

Figure 4-11: High temperature points at a) 1.66 x 10^{-2} and 8.30 x 10^{-3} kg/min, b) 4.15 x 10^{-3} and 2.08 x $^{10-3}$ kg/min

All of the points start out higher near the coolant hole and gradually decrease, until they start to rise back up at about $x/d = 8.5$. Window effects are a likely explanation for this phenomena, as that point is close to the edge of the IR window. As with the low temperature data, most of the high temperature points lie within uncertainty of each other, complicating a definite interpretation of the data.

4.2.3. Temperature Regime Comparison

The most striking comparison to be made between the high and low temperature data is the increased lateral conduction in the high temperature cases. Figure 4-12 shows two sample IR images that illustrate this point. The low temperature case (a) displays sharper overall effectiveness contours than (b). The thermal conductivity of the Hastelloy plate changes from approximately 11.6 $\frac{W}{m*K}$ at low temperature to 24.3 $\frac{W}{m*K}$ at high temperature, representing a 2.1 times increase. Meanwhile, the thermal conductivity of air only changes from about 0.03 to roughly 0.055 $\frac{W}{m*K}$, which is only 1.83 times larger. If it is assumed that the Nusselt number remains relatively constant thanks to the similar Reynolds and Prandtl numbers, the conductivity changes indicate that the Biot number at high temperature was approximately 0.89 times the low temperature Biot number, via Eqs. (2-7) and (2-8).

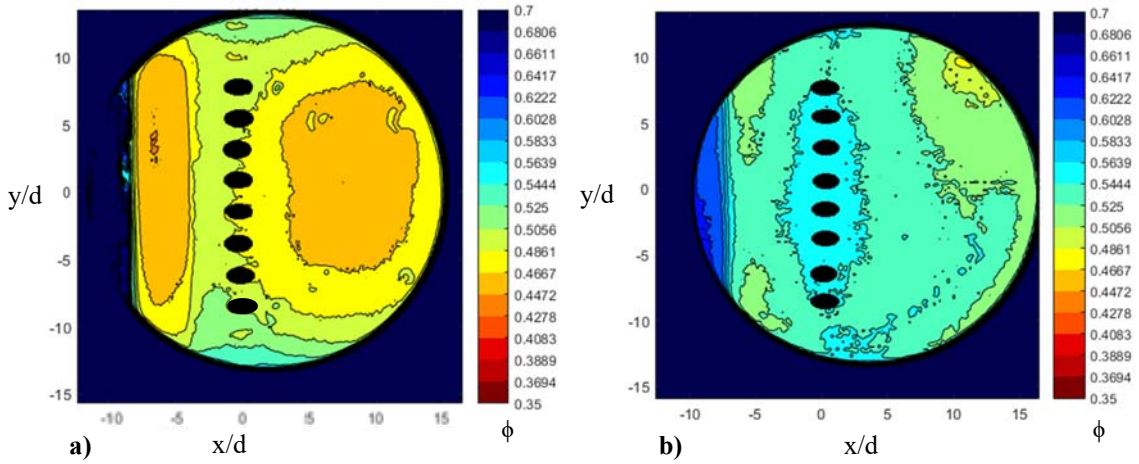

Figure 4-12: ϕ distributions at M = 2, ER = 3, DR = 1.7, with matched freestream Re = 4120 a) CO2 at 420K freestream b) Air at 1300K freestream

The lower Biot number also contributes to a higher overall film cooling effectiveness, via Eq. (2-10). By the same equation, the difference in the coolant Reynolds number could contribute to a different convection coefficient ratio, also changing the overall effectiveness. Also, the ACR

value for the high temperature cases is higher than the corresponding low temperature CO_2 case. Whatever the cause, Figure 4-13 shows that the high temperature points displayed higher overall effectiveness than their equivalent low temperature points. Furthermore, the figure illustrates that both temperature regimes experienced the aforementioned trends of overall effectiveness with coolant mass flow, suggesting that the observed trends are repeatable phenomena. It is difficult to determine how much of the observed difference may be due to the shift in test conditions from testing on different days, using different calibrations, etc. Based on the repeatability investigation in Section 3.4.2, it is possible that some of the change is due to currently unknown variables.

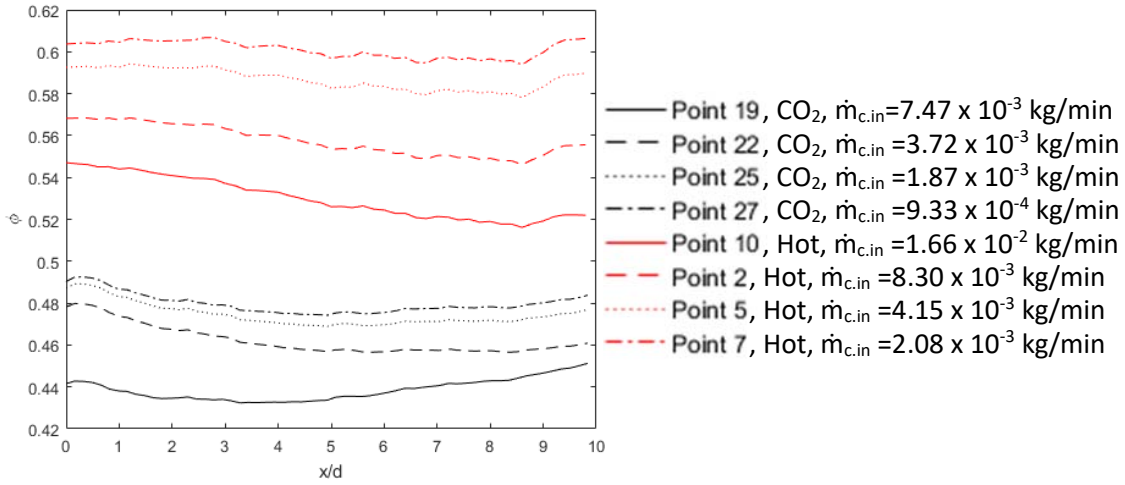

Figure 4-13: Comparison of high temperature air and low temperature CO_2 at M = 1

For both the low and high temperature data, the coolant temperature dropped as the coolant mass flow increased. Therefore, it was not clear whether the observed trends showed the influence of coolant mass flow or coolant temperature on the overall effectiveness. Further investigation was required, as discussed in the next section.

4.3. Near Ambient Coolant Temperature Impact Investigation

A new set of low temperature tests was performed, with the goal of disentangling the effects of coolant mass flow and coolant temperature discussed in the previous section. The data points for this new test series are shown in Table 4-7. The CO_2 points from the first set of low temperature data were deemed to be the most reasonable option for comparison, as they experienced less separation than air and spanned a broader range of conditions than was capable with argon. The test points sought to match the original Set 1 points as closely as possible. The equipment set up was identical. The freestream temperature, freestream flow rate, and coolant flow rates were matched as closely as possible. A clean sapphire window was used, to avoid any potential impact from combustion buildup gathered during the high temperature tests. The only change was that the coolant was heated using the in-line heater, instead of cooled with the chiller. This shift led to coolant temperatures anywhere from 5K-15K higher for a given coolant mass flow.

Table 4-7: Low Temperature Data Points, Set 2

Point #	Coolant	M goal	M actual	ER	DR	I	ACR	Re_∞	T_c (K)	$\dot{m}_{c,in}$ (kg/min)
1	CO_2	2	1.89	3	1.72	2.07	1.71	4455	376.3	7.37×10^{-3}
2	CO_2	1	0.94	7	1.70	0.52	0.85	4469	376	7.37×10^{-3}
3	CO_2	0.5	0.46	15	1.69	0.12	0.41	4613	379.5	7.37×10^{-3}
4	CO_2	2	1.92	1	1.68	2.20	1.75	4375	383.1	3.69×10^{-3}
5	CO_2	1	0.96	3	1.70	0.54	0.87	4400	376.6	3.69×10^{-3}
6	CO_2	0.5	0.48	7	1.70	0.13	0.43	4413	375.3	3.69×10^{-3}
7	CO_2	2	1.85	0	1.70	2.02	1.68	4538	374.6	1.84×10^{-3}
8	CO_2	1	0.94	1	1.70	0.52	0.85	4456	374	1.84×10^{-3}
9	CO_2	0.5	0.48	3	1.71	0.13	0.43	4401	373.4	1.84×10^{-3}

Interestingly, using the heater generally led to a more stable coolant temperature (and thus *DR*) than using the chiller. This was thanks to the ability to hand-tune the heater during testing, to try and limit coolant temperature variation. Points 3 and 4 are exceptions, where the coolant temperature crept up unnoticed and continued due to thermal buildup even when the heater was

turned down. Section 4.3.1 will discuss the data from this set on its own. Section 4.3.2 will compare this data to the low temperature data points from Set 1. The following subsections will discuss trends within the set of data on its own, and then compare it to the data from the previous tests.

4.3.1. Increased T_c Test Data

The data from this set was clustered similarly to the comparable CO_2 points from the first set of low temperature data. However, the overall effectiveness did not correlate to the total coolant mass flow. At blowing ratios of one and two in Figure 4-14, the middle flow rate, 3.6910^{-3} kg/min, performs the best, followed by the lower flow rate and then the higher. However, at $M = 0.5$, the high flow rate case was on par with the middle mass flow, and the low flow rate case was the lowest.

The effect of coolant temperature within this data set is most visible at Point 4 in Figure 4-14b. The coolant temperature crept up to 383.1K, due to the nonlinearity of the coolant heater control dial. In keeping with the previously mentioned trends, the higher coolant temperature produced a high overall effectiveness of nearly 0.62. For most of the points, the coolant temperature is within 2-3K of the average, which appears to limit its impact on the change in overall effectiveness between points. For example, Points 7 and 8 are at 374K, the lowest coolant temperatures at $M = 2$ and 1 respectively, yet the overall effectiveness values they each produce are in between points with slightly higher coolant temperatures, around 376K. The next section will compare these data points to the data in Set 1.

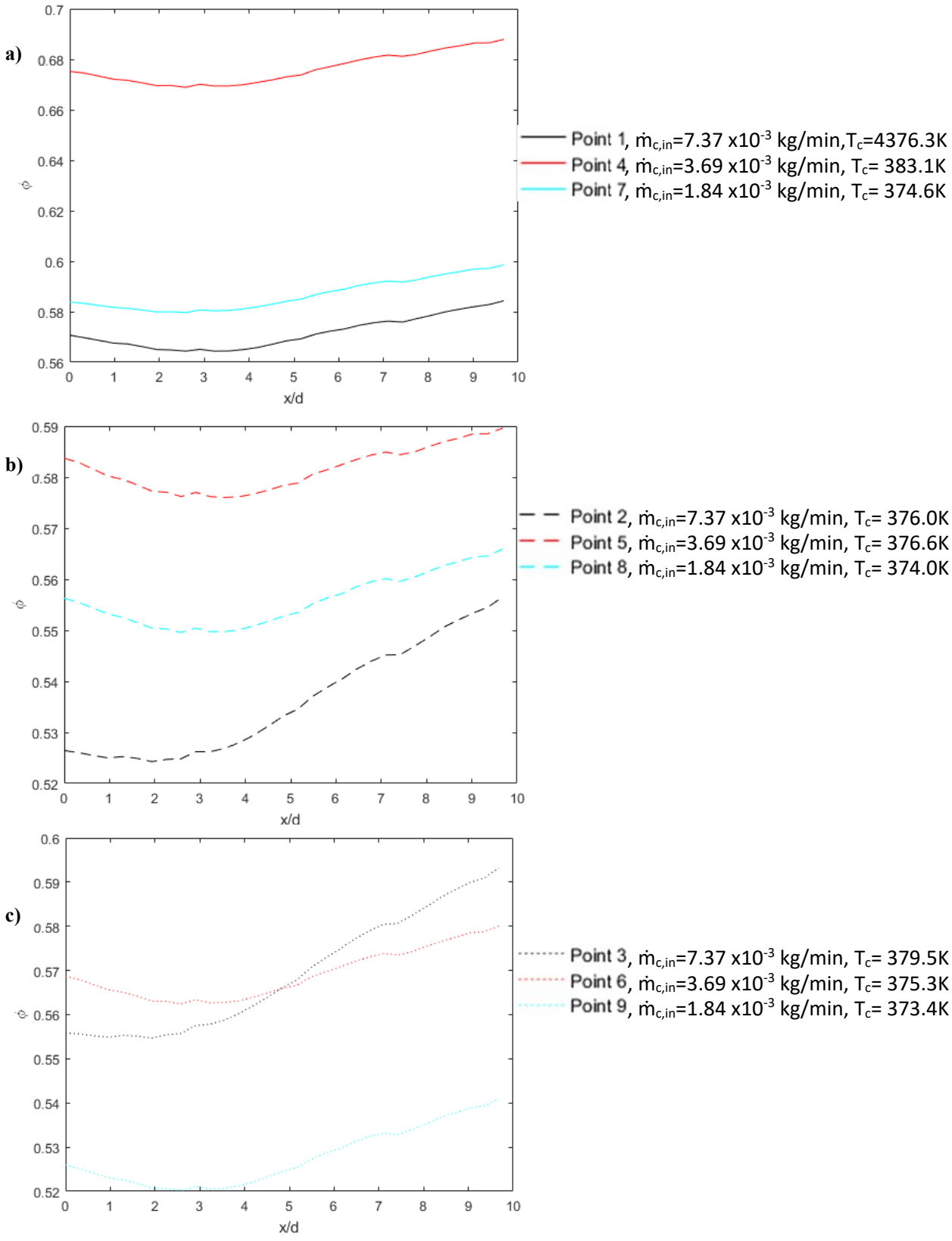

Figure 4-14: Low temperature Set 2 points at a) $M = 2$, b) $M = 1$, c) $M = 0.5$

4.3.2. Comparison between Sets

Comparison between the first and second sets of low temperature data shows that the cases with the higher coolant temperature consistently display better overall effectiveness. On average, the higher coolant temperature cases have an overall effectiveness that is 0.09 higher than the equivalent low coolant temperature case. The effect is more noticeable at the higher coolant mass flows, where the difference in T_c was larger, around 15 K. Conversely, at the lowest coolant flow rate, the difference in overall effectiveness was closer to 0.05, since the coolant temperatures were only about 5 K apart. The *ACR* values were slightly higher for Set 2 points, but they were still within 0.01-0.02 of each other. In Figure 4-15a, both data sets experience an unexpected increase in the overall effectiveness at M = 0.5, while the other flow rates show the expected trend of higher effectiveness with higher M. As discussed in Section 2.3.3, the internal flow can generate turbulence within the coolant holes, causing the jet to separate inside the hole. The analysis of the internal Reynolds numbers in Section 3.1.3.1 showed that there is a possibility of transitional flow in the region behind the holes, suggesting that internal flow effects might explain that particular phenomena. Further investigation is needed to confirm if this hypothesis is accurate. Either way, the fact that the pattern repeats in both data sets suggests that the flow fields for the coolant and freestream are well matched between the two sets.

In Figure 4-15b, it looks as though both sets would have given the same close-set pattern, if Point 4 of Set 2 had not experienced that spike in coolant temperature. At the lowest mass flow, the blowing ratio appears to have a larger impact on the overall effectiveness for the Set 2 points than it did on Set 1. Most of the points from both sets of data show the effectiveness increasing slightly towards the end of the measurement region. However, the higher coolant temperature points do not exhibit the bump in overall effectiveness near the coolant hole that can be observed

in the points from Set 1. The trends visible here seem to suggest that higher coolant temperature leads to a higher overall effectiveness. However, it is important to remember that all of these points technically lie within uncertainty from each other, with the exception of Point 4 from Set 2. Also, these two datasets were taken on different days, with different IR calibrations. Figure 4-16 shows the calibration curves for both datasets side-by-side. Note that the Set 1 calibration curve reads notably higher counts for a given temperature. The difference is partially due to the change in integration time on the IR camera (0.25008 ms for Set 1, 0.3008 ms for Set 2). The corrected Set 1 calibration curve shows an approximation of what the calibration curve would have looked like if Set 1 had been taken with an integration time of 0.3008 ms, assuming constant radiation intensity. Even with that correction, Set 1 registers roughly 2000 more counts at a given temperature than Set 2. Numerous factors could account for the remaining difference. For example, the test section was disassembled and reassembled in between the two sets, so Set 1 might have experienced more reflected radiation from the surroundings than Set 2, if the window was at an angle relative to the camera, or if IR sources in the room had been moved. Additionally, high temperature tests were run in between these two sets, so the high temperatures could have changed the emissivity of the heat-resistant paint on the airfoil surface. The emissivity would still be even across the surface, but if the emissivity dropped it would explain why Set 2 registered fewer counts at higher temperatures. The goal of the in-situ calibration process is to correct for these sort of changes on a day-to-day basis, so the differences in the calibration curves between Set 1 and Set 2 are not necessarily surprising or detrimental. However, it would be beneficial for future studies to investigate the efficacy of the calibration process more thoroughly.

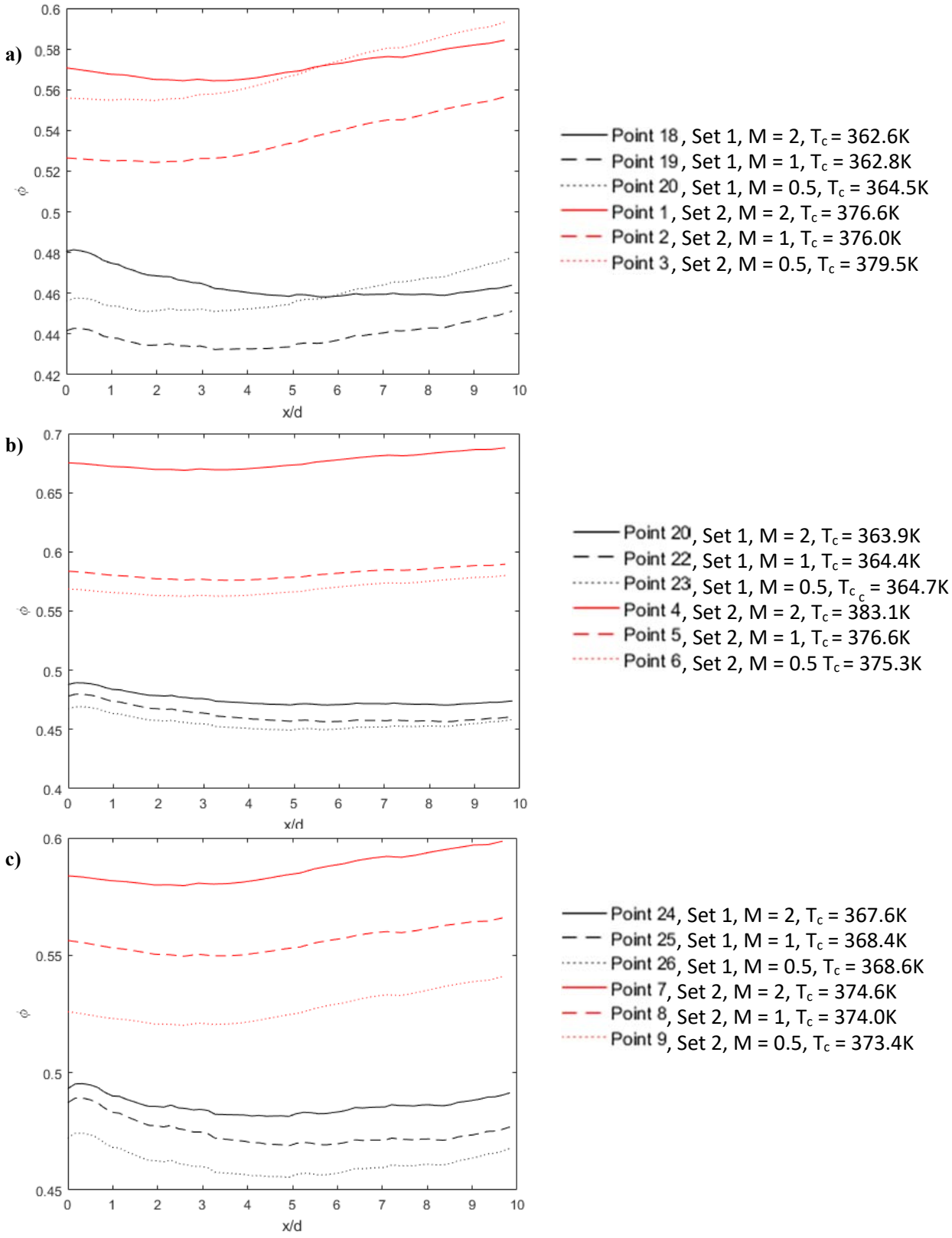

Figure 4-15: Low temperature comparison with CO_2 at a total coolant flow rate of a) 7.3E-03 kg/min, b) 3.6E-03 kg/min c) 1.8E-03 kg/min

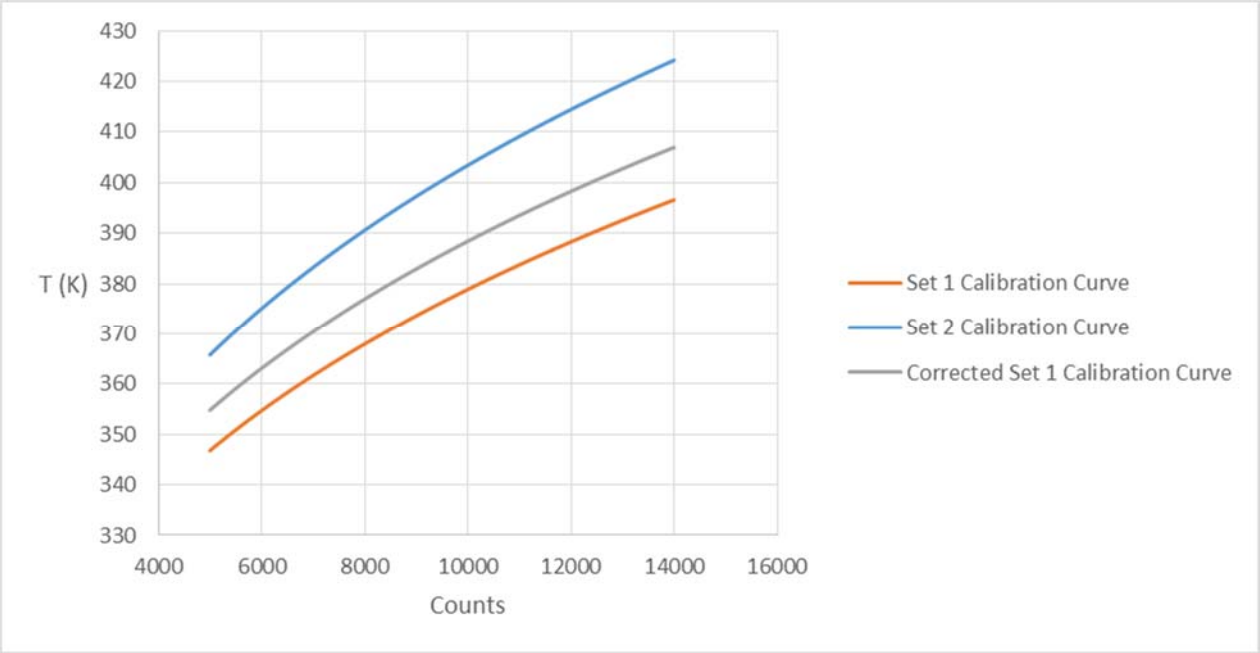

Figure 4-16: Comparison of Set 1 and Set 2 calibration curves

5. Conclusions

The experiments performed for this thesis were still in a relatively new line of inquiry for the AFIT FCR. They provided valuable information about the operating capabilities of the rig. The conclusions presented below discuss the ramifications of the experimental results, as well as possible avenues for future work to follow. The rig modifications made throughout the course of this investigation are also assessed and possible future modifications are discussed.

5.1. Leading Edge Phenomena and LEFCT Comparisons

A number of different methods were used to compare the FCR to the LEFCT. A 2D CFD simulation was crafted to quantify the effect of the differing area ratios between the two facilities, using FLUENT. A series of PSP tests were then run on the leading edge test plate airfoil, in an attempt to match the nondimensionalized flow parameters Re_∞, DR, M, I, and ACR with PSP tests performed by Lt Wiese on the LEFCT and compare the results. Finally, multiple tests were run with the IR camera viewing the leading edge of the FCR test plate.

The rudimentary 2D CFD simulations generated for this investigation compared the flow fields for two cases, one with an area ratio representative of the LEFCT (0.78) and one with an area ratio representative of the FCR (0.58). The simulations showed that this change in the area ratio only increases the freestream velocity just above the coolant holes from 1.32 m/s to 1.34 m/s (1.5%), which is within acceptable limits for comparing the two facilities.

Although the gathered PSP data did not exactly hit the desired test points, it did provide some insight into the viability of the PSP test procedure. The points also demonstrated the effect of high momentum flux ratios, with observable separation of the coolant jets at high I values. Lower I values showed much more uniform coolant distribution.

The IR images of the leading edge test plate revealed previously uninvestigated characteristics of the FCR test plates. The near-constant temperature distribution across the leading edge could be simply explained by the low Biot number of the airfoil. The effect of the apparent impingement scenario of the coolant on the interior of the test plate is also visible. The drastic transition observed between the leading edge and the flat plate was puzzling. It could potentially be explained by an external flow effect, if the seam is sharp enough to disrupt the flow over the airfoil.

5.2. **Matching Low and High Temperature Tests**

IR tests were performed to capture temperature distributions on the shaped hole test plate at both low and high temperatures. Those temperature distributions were then processed into overall effectiveness distributions over the test plate. At low temperatures (420 K freestream) air, argon, and CO_2 coolant gases were used to provide a range of *DR* and *ACR* values. The coolant chiller was used to achieve coolant temperatures in the range 358-370 K. The high temperature (1300 K freestream) tests used air as the coolant gas. The high temperature tests roughly matched Re_∞, *M*, and *ER* with the low temperature points, and roughly matched *DR* and *ACR* when able due to gas property variation between the temperature regimes.

Comparison of the low and high temperature tests collected for this investigation show that the Biot number was not perfectly matched, despite identical test equipment. The thermodynamic properties of air and the thermal conductivity of the test plate simply do not change at the same rate, leading to a high temperature Biot number that was approximately 0.89 times the low temperature Biot number. Additionally, the *ACR* of the high temperature points is somewhat higher than the *ACR* of CO_2 at the corresponding points. The impact of these parameters is evident in the results, with overall effectiveness values about 0.1 greater at higher temperatures, despite similar

blowing ratios, density ratios, and freestream Reynolds numbers. In the low temperature data, overall effectiveness tended to increase with *ACR*. In fact, the higher *ACR* of air at Points 1-9 led to overall effectiveness 0.01 greater than the corresponding CO_2 points, despite CO_2's higher *DR*. In general, points with higher *M* values produced better overall effectiveness values than points with lower *M* at identical total coolant mass flows, which the exception of the $M = 2$ air points, which experienced separation. However, most of the low temperature data points are all within uncertainty of each other, due to the large uncertainty at low temperatures. The *M* trends are also apparent at high temperature, where the lower uncertainty allows more confidence in the usefulness of the results.

5.3. **Coolant Mass Flow and Temperature Impact**

To evaluate the observed trends with coolant mass flow and temperature, a second set of low temperature data was recorded using CO_2 as the coolant gas. The new set used the coolant heater to achieve higher T_c values than the CO_2 points in the first set, while matching all other parameters as closely as possible. Re_∞, *M*, *I* and *ER* were closely matched, while *DR* and *ACR* were matched as closely as possible considering the slight changes from the change in T_c.

Comparison of the two sets of low temperature data suggests that the surface temperature of the test plate does not decrease proportionally with the coolant temperature. Comparison of two sets of CO_2 points taken with matched freestream conditions, blowing ratios, and coolant flow rates showed that for a coolant temperature increase of ~15K, the overall effectiveness increased by ~0.09. A smaller coolant temperature increase of ~5K produced a correspondingly smaller increase in overall effectiveness of ~0.05. The most likely explanation of these observations is that the temperature of the test plate is not governed solely by the freestream and coolant. The heat from the test section is most likely conducting out into the room.

The comparison between the two sets of CO_2 points also revealed that at flow rates of 7.37 x 10^{-3} kg/min, CO_2 experienced a repeatable phenomenon wherein the M = 0.5 case actually outperformed the M = 1 case at the same flow rate, almost on par with the M = 2 case. Other general trends with coolant mass flow rate were also similar between the two sets. The recurrence of these trends suggest that the internal and external flow fields were successfully matched between Set 1 and Set 2.

The *ACR* values of the Set 2 points were slightly higher than the Set 1 values, but only by 0.01-0.02 depending on the point. Although technically beneficial, such a small change probably cannot completely account for the observed differences in overall effectiveness. Both sets showed similar trends of increasing overall effectiveness with increasing M at most points. The impact of *ER* was difficult to disentangle from the impact of T_c, but typically the highest *ER* points reported the lowest overall cooling effectiveness.

5.4. FCR Modifications and Future Improvements

A number of modifications to the rig were made and assessed during this investigation. This section discusses those modifications and mentions possible future modifications. The first addition was the new coolant feed design, which succeeded in generating symmetrical flow through the cooling channel plenum, which is a vast improvement over the previous design. With the baffle plate installed, the new design also displayed smoother flow distribution up to a higher mass flow ratio as well.

The new boundary layer bleed design provided large amounts of temperature data to help understand the process by which the coolant seems to pick up an inordinate amount of heat as it passes through the test block. In comparison with previous data collected by Ashby [2], the

boundary layer bleed seemed to produce coolant temperatures 50 K lower than the previous design.

Multiple test window options were also evaluated during the course of this investigation. It was found that angling the rig slightly reduced the reflection to the IR camera. Using no window affected the flow field through the rig, and thus is not recommended. Likewise, attempting to angle the window itself using the current front plate design introduced some leakage, but did reduce the reflection. The bare sapphire and anti-reflection coated silicon windows performed similarly to one another. Additionally, a cleaning method for the sapphire IR windows was developed, using felt dowel heads and simple polishing compound. This method proved effective in removing combustion build-up from the window. Cerium oxide polish is recommended for future cleaning efforts, as it is a common and relatively inexpensive glass polishing compound and will not scratch the sapphire windows.

A high-temperature heater tape was utilized for some testing. Its usefulness was limited by a lack of temperature control. Also, high-temperature insulation is required to use the tape effectively. However, the amount of heat the tape can provide is considerable, so if its shortcomings are managed, the tape could potentially increase the operable range of the FCR. Further investigation into the use of the heater tape is recommended.

Various methods of improving the IR camera resolution were also investigated, including moving the camera closer to the rig and employing lens spacer rings. It was determined that a combined spacer ring distance of 1.9 centimeters would allow the camera to focus on the test plate while positioned within 30.5 centimeters of the test section, increasing the resolution from 4-5 pixels per hole diameter to about 15 pixels per hole diameter. A new mounting platform that close to the rig is feasible, but the camera would need a heat shield to protect it from excessive

temperatures during high temperature testing. Additionally, the potential lens distortion generated by using such a wide field of view was not investigated and should be considered if this method of increasing the IR camera resolution is put into practice.

One method for matching the Biot number would be to use a separate, higher-conductivity test plate at the low temperature condition, so that the thermal conductivities of the air and test plate change proportionally across the temperature change between high and low temperature test conditions. The downside of this method would be the additional step of swapping out the test plate between low and high temperature tests. It also introduces possible sources of error, like manufacturing or assembly discrepancies. However, it is the most viable method available, to the knowledge of this author. Invar, Nichrome, and other nickel alloys possess thermal conductivities in the range of 12-15 W/(m*K), which would be viable for low temperature tests that more closely match the Biot number at high temperature. Changing the thickness of the low temperature plate would also change the Biot number, but would necessarily alter the geometry of the test plate, which would prevent matching between the two tests.

For future PSP studies, it is suggested that effort be made to increase the spatial resolution of the images. Some methods to do so include using a 75mm lens (rather than the 35mm lens used in this study), experimenting with spacer rings between the lens and the CCD Camera, and angling the mount for the camera and lights in such a way that the camera is more directly perpendicular to the cooling holes.

Additionally, future work could help characterize the flow inside of the coolant channel. Currently, the flow pattern is not known, although it is assumed that at higher flow rates the coolant impinges near the intersection of the leading edge and flat region before travelling normally through the channel. The effect of the thermocouple wires within the coolant channel

cavity is also unknown. CFD modeling could potentially broaden our understanding of flow within the coolant channel. A CFD-based Nusselt number correlation for coolant Reynolds and Prandtl numbers would vastly improve the ability to match these important parameters. The flow pattern in the test section could be assessed via flow visualization by feeding seed particles through the B-type thermocouple port at the entrance to the test section and viewing the flow through transparent side walls. Assessing the coolant channel flow patterns experimentally would be more difficult, due to the lack of optical access and small size of the flow pathway.

References

[1] J. Mattingly and H. von Ohain, Elements of Propulsion: Gas Turbines and Rockets, AIAA, 2006.

[2] R. W. Ashby, "Scaling Film Cooling Performance from Ambient to Near Engine Temperatures," in *M. S. thesis, Air Force Institute of Technology, Wright-Patterson AFB, OH.*, 2017.

[3] D. G. Bogard and K. A. Thole, "Gas Turbine Film Cooling," *Journal of Propulsion and Power,* vol. 22, no. 2, pp. 249-270, 2006.

[4] J. Han, S. Dutta and S. Ekkad, Gas Turbine Heat Transfer and Cooling Technology, Boca Raton, Florida: CRC Press, 2012.

[5] T. F. Fric and A. Roshko, "Vortical Structure in the Wake of a Transverse Jet," *Journal of Fluid Mechanics,* vol. 279(1), pp. pp. 1-47, 1994.

[6] S. A. Lawson, D. L. Straub, S. Beer, K. H. Casleton and T. Sidwell, "Direct Measurements of Overall Effectiveness and Heat Flux on a Film Cooled Test Article at High Temperatures and Pressures," *ASME Paper No. GT2013-94685.,* 2013.

[7] M. K. Eberly and K. A. Thole, "Time-Resolved Film-Cooling Flows at High and Low Density Ratios," *Journal of Turbomachinery, 136(6), 061003.,* 2014.

[8] R. P. Williams, T. E. Dyson, D. G. Bogard and S. D. Bradshaw, "Sensitivity of the Overall Effectiveness to Film Cooling and Internal Cooling on a Turbine Vane Suction Side," *Journal of Turbomachinery,* vol. 136, no. 3, pp. 031006-1-031006-7, 2014.

[9] J. Albert, D. Bogard and F. Cunha, "Adiabatic and overall effectiveness for a film cooled blade," in *In ASME Turbo Expo 2004: Power for Land, Sea, and Air, GT2004-53998. American Society of Mechanical Engineers*, 2004.

[10] F. P. Incropera, D. P. Dewitt, T. L. Bergman and A. S. Lavine, Fundamentals of Heat and Mass Transfer, 6th Ed., Hoboken, NJ: Wiley & Sons, Inc., 2007.

[11] M. Martiny, A. Schulz and S. Wittig, "Mathematical Model Describing the Coupled Heat Transfer in Effusion Cooled Combustor Walls," in *ASME Paper No. 97-GT-329*, Orlando, FL, 1997.

[12] J. L. Rutledge, M. D. Polanka and D. G. Bogard, "The Delta Phi Method of Evaluating Overall Film Cooling Performance," *Journal of Turbomachinery 138.7 (2016): 071006.*.

[13] J. E. Dees, D. G. Bogard, G. A. Ledezma, G. M. Laskowski and A. K. Tolpadi, "Experimental Measurements and Computational Predictions for an Internally Cooled Simulated Turbine Vane With 90 Degree Rib Turbulators," *Journal of Turbomachinery,* vol. 134, no. 11, pp. 061005-1-061005-9, 2012.

[14] J. B. Esgar, "Turbine Cooling-Its Limitations and Its Future in High Temperature Turbines," NASA TM X-52801, Cleveland, 1970.

[15] D. P. Narzary, K. C. Liu, A. P. Rallabandi and J. C. Han, "Influence of Coolant Density on Turbine Blade Film-Cooling Using Pressure Sensitive Paint Technique," *Journal of Turbomachinery,* vol. 134(5), pp. pp. 031006-1-10, 2012.

[16] N. J. Greiner, M. D. Polanka and J. L. Rutledge, "Scaling of Film Cooling Performance From Ambient to Engine Temperatures," *Journal of Turbomachinery,,* vol. 137(7), pp. pp. 071007-1-11., 2015.

[17] J. L. Rutledge and M. D. Polanka, "CFD Evaluations of Unconventional Film Cooling Scaling Parameters on a Simulated Turbine Blade Leading Edge," in *ASME Turbo Expo 2014: Turbine Technical Conference and Exposition. American Society of Mechanical Engineers*, 2014.

[18] C. J. Wiese, J. L. Rutledge, M. D. Polanka and R. W. Ashby, "Film Coolant Property Variation in Scaling Gas Turbine Cooling Effectiveness," *AIAA Paper No. 2016-0904,* 2016.

[19] A. J. Lynch, "Overall Effectiveness Measurements at Engine Temperatures with Reactive Film Cooling and Surface Curvature," in *M. S. thesis, Air Force Institute of Technology, Wright-Patterson AFB, OH*, 2015.

[20] M. Ghorab, "Film cooling effectiveness and net heat flux reduction of advanced cooling schemes using thermochromic liquid crystal," *Applied Thermal Engineering,* vol. 31(1), pp. pp.77-92., 2011.

[21] S. Baldauf, M. Scheurlen, A. Schulz and S. Wittig, "Correlation of Film-Cooling Effectiveness From Thermographic Measurements at Enginelike Conditions," *Journal of Turbomachinery,* vol. 124(4), pp. pp. 686-698, 2002.

[22] M. K. Harrington, M. A. McWaters, D. G. Bogard, C. A. Lemmon and K. A. Thole., "Full-coverage film cooling with short normal injection holes," in *ASME Turbo Expo 2001: Power for Land, Sea, and Air. American Society of Mechanical Engineers*, 2001.

[23] J. F. Muska, R. W. Fish and M. Suo, "Film cooling effectiveness for injection from multirow holes," *Journal of Engineering for Power,* vol. 101, p. 101, 1979.

[24] R. S. Bunker, "A Review of Shaped Hole Turbine Film-Cooling Technology," *Journal of Heat Transfer,* vol. 127(4), pp. pp. 441-453, 2005.

[25] J. Dittmar, A. Schulz and S. Wittig, "Assessment of Various Film-Cooling Configurations Including Shaped and Compound Angle Holes Based on Large-Scale Experiments," *Journal of Turbomachinery,* vol. 125(1), pp. pp. 57-64, 2003.

[26] C. Saumweber, A. Schulz and S. Wittig, "Free-Stream Turbulence Effects on Film Cooling With Shaped Holes," *Journal of Turbomachinery,* vol. 125(1), pp. pp. 65-73, 2003.

[27] H. Reiss and A. Boelcs, "‘‘Experimental Study of Showerhead Cooling on a Cylinder Comparing Several Configurations Using Cylindrical and Shaped Holes," in *IGTI Turbo Expo Paper 99-GT-123.*, Indianapolis, 1999.

[28] R. S. Bunker, "Film Cooling Effectiveness Due to Discrete Holes Within a Transverse Surface Slot," *ASME Paper No. GT2002-30178.,* 2002.

[29] T. F. Fric and R. P. Campbell, "Method of Improving the Cooling Effectiveness of a Gaseous Coolant Stream Which Flows Through a Substrate, and Related Articles of Manufacture," *US Patent No. 6,383,602.,* 2002.

[30] M. Gritsch, A. Schulz and S. Wittig, "Adiabatic Wall Effectiveness Measurements of Film-Cooling Holes With Expanded Exits," *Journal of Turbomachinery,* vol. 120(3), pp. pp. 549-556, 1998.

[31] J. B. Anderson, E. K. Wilkes, J. W. McClintic and D. G. Bogard, "Effects of Freestream Mach Number, Reynolds Number, and Boundary Layer Thickness on Film Cooling Effectiveness of Shaped Holes," in *ASME Turbo Expo 2016: Turbomachinery Technical Conference and Exposition*, 2016.

[32] K. A. Thole, M. Gritsch, A. Schulz and S. Wittig, "Effect of a Crossflow at the Entrance to a Film-Cooling Hole," *Journal of Fluids Engineering,* vol. 119(3), pp. pp. 533-540, 1997.

[33] J. E. Dees, D. G. Bogard, G. A. Ledezma, G. M. Laskowski and A. K. Tolpadi, "Experimental measurements and computational predictions for an internally cooled simulated turbine vane," *Journal of Turbomachinery,* Vols. 134,, no. no. 6, p. 061003, 2012.

[34] A. K. Sinha, D. G. Bogard and M. E. Crawford, "Film-Cooling Effectiveness Downstream of a Single Row of Holes With Variable Density Ratio," *Journal of Turbomachinery,* vol. 113(3), pp. pp. 442-449, 1991.

[35] S. V. Ekkad, J. C. Han and H. Du, "Detailed Film Cooling Measurements on a Cylindrical Leading Edge Model: Effect of Free-Stream Turbulence and Coolant Density," *Journal of Turbomachinery,* vol. 120(4), pp. pp. 799-807., 1998.

[36] S. V. Ekkad, S. Ou and R. B. Rivir, "A Transient Infrared Thermography Method for Simultaneous Film Cooling Effectiveness and Heat Transfer Coefficient Measurements From a Single Test," *Journal of Turbomachinery,* vol. 126(4), pp. pp. 597-603, 2004.

[37] J. E. Albert and D. G. Bogard, "Measurements of Adiabatic Film and Overall Cooling Effectiveness on a Turbine Vane Pressure Side With a Trench," *Journal of Turbomachinery,* vol. 135, no. 9, pp. 051007-1-051007-11, 2013.

[38] L. M. Wright, Z. Gao, T. A. Varvel and J. C. Han, "Assessment of Steady State PSP, TSP, and IR Measurement Techniques for Flat Plate Film Cooling," *ASME Paper No. HT2005-72363.,* 2005.

[39] P. C. Sweeney and J. F. Rhodes, "An Infrared Technique for Evaluating Turbine Airfoil Cooling Designs," *Journal of Turbomachinery,* vol. 122, no. 1, pp. 170-177, 2000.

[40] N. J. Greiner, M. D. Polanka, J. L. Rutledge and A. T. Shewhart, "Effect of Variable Properties and Radiation on Convective Heat Transfer Measurements at Engine Conditions," *ASME Paper No. GT2014-25701.,* 2014.

[41] R. J. Goldstein and H. H. Cho, "A Review of Mass Transfer Measurements Using Naphthalene Sublimation," *Experimental Thermal and Fluid Science,,* vol. 10, pp. pp. 416-434, 1995.

[42] W. B. Nicoll and J. H. Whitelaw, "The Effectiveness of the Uniform Density, Two-Dimensional Wall Jet," *International Journal of Heat and Mass Transfer,* vol. 10, pp. pp. 623-639, 1967.

[43] J. Crafton, S. Fonov, R. Forlines and S. Palluconi, "Development of Pressure-Sensitive Paint Systems for Low Speed Flows and Large Wind Tunnels," *AIAA Paper No. 2013-0482.,* 2013.

[44] J. C. Han and A. P. Rallabandi, "Turbine Blade Film Cooling Using PSP Techniqu," *Frontiers in Heat and Mass Transfer,* vol. 1(1), pp. pp. 1-21., 2010.

[45] A. T. Shewhart, "Minimization of the Effects of Secondary Reactions on Turbine Film Cooling in a Fuel Rich Environment," in *M. S. thesis, Air Force Institute of Technology, Wright-Patterson AFB, OH.*, 2014.

[46] J. E. Nenniger, A. Kridiotis, J. Chomiak, J. P. Longwell and S. A. F., "Characterization of a Toroidal Well Stirred Reactor," *Twentieth Symposium on Combustion,* vol. 20(1), pp. pp. 473-479, 1985.

[47] S. D. Stouffer, R. Pawlik, G. Justinger, J. Heyne, J. Zelina and D. Ballal, "Combustion Performance and Emissions Characteristics for a Well-Stirred Reactor for Low Volatility Hydrocarbon Fuels," *AIAA Paper No. 2007-5663.,* 2007.

[48] H. Schlichting and K. Gersten, Boundary-Layer Theory, Springer, 2016.

[49] R. J. Moffat, "Describing the Uncertainties in Experimental Results," *Experimental Thermal and Fluid Science,* vol. 1, no. 1, pp. 3-17, 1988.

[50] The White House, "National Security Strategy," 2015.

[51] B. T. Bohan and M. D. Polanka, "Analysis of Flow Migration in an Ultra-Compact Combustor," *Journal of Engineering for Gas Turbines and Power,* vol. 135, no. 5, pp. 1-11, 2013.

[52] S. B. Pope, Turbulent Flows, Cambridge: Cambridge University Press, 2000.

[53] M. P. Boyce, Gas Turbine Engineering Handbook, 4th ed., Butterworh-Heinemann, 2011.

[54] B. T. Bohan, "Analysis of Flow Migration in an Ultra-Compact Combustor," Air Force Institute of Technology, Wright-Patterson Air Force Base, Ohio, 2011.

[55] F. M. White, Viscous Fluid Flow, 3rd ed., McGraw-Hill, 2005.

[56] W. M. Kays, M. E. Crawford and B. Weigand, Convective Heat and Mass Transfer, 4th ed., New Delhi: McGraw Hill Education, 2012.

[57] M. D. Polanka, ""Detailed Film Cooling Effectiveness and Three Component Velocity Field Measurements on a First Stage Turbine Vane Subject to High Freestream Turbulence," The University of Texas at Austin, Austin, TX, 1999.

[58] M. L. Nathan, T. E. Dyson, D. G. Bogard and S. D. Bradshaw, "Adiabatic and Overall Effectiveness for the Showerhead Film Cooling of a Turbine Vane," *Journal of Turbomachinery,* vol. 136, no. 3, pp. 031005-1-031005-9, 2014.

[59] H. D. Ammari, N. Hay and D. Lampard, "The Effect of Density Ratio on the Heat Transfer Coefficient From a Film-Cooled Flat Plate," *Journal of Turbomachinery,* vol. 112(3), pp. pp. 444-450, 1990.

[60] J. E. Dees, D. G. Bogard, G. A. Ledezma and G. M. Laskowski, "Overall and Adiabatic Effectiveness Values on a Scaled Up, Simulated Gas Turbine Vane: Part I—Experimental Measurements," in *ASME 2011 Turbo Expo: Turbine Technical Conference*, 2011.

[61] P. H. Chen, M. S. Hung and P. P. Ding, "Film Cooling Performance on Curved Walls With Compound Angle Hole Configuration," *Ann. N.Y. Acad. Sci.,* vol. 934, p. pp. 353–360, 2001.

[62] N. J. Greiner, M. D. Polanka, J. L. Rutledge and J. R. Robertson, "Effect of Variable Properties Within a Boundary Layer With Large Freestream-to-Wall Temperature Differences," *Journal of Engineering for Gas Turbines and Power,* vol. 136(5), pp. pp. 052604-1-9, 2014.

[63] R. Krewinkel, J. Farber, U. Orth, D. Frank, M. Lauer, C. Pilgrim, A. Y. Gonzalez, J. Feist, R. Saggese, S. Bertheir and S. Araguas-Rodriguez, "Validation of Surface Temperature Measurements on a Combustor Liner Under Full-Load Conditions Using a Novel Thermal History Paint," *Journal of Engineering for Gas Turbines and Power 139.4 (2017): 041508..*

REPORT DOCUMENTATION PAGE

Form Approved
OMB No. 0704-0188

1. REPORT DATE *(DD-MM-YYYY)*	**2. REPORT TYPE**	**3. DATES COVERED** *(From - To)*
23-03-2017	Master's Thesis	Aug 2016 – Mar 2017

4. TITLE AND SUBTITLE
Relating Film Cooling Performance Between Ambient and Near Engine Temperatures

5a. CONTRACT NUMBER

5b. GRANT NUMBER

5c. PROGRAM ELEMENT NUMBER

6. AUTHOR(S)

Vorgert, Christopher J, 2Lt

5d. PROJECT NUMBER

5e. TASK NUMBER

5f. WORK UNIT NUMBER

7. PERFORMING ORGANIZATION NAME(S) AND ADDRESS(ES)

Air Force Institute of Technology
Graduate School of Engineering and Management (AFIT/EN)
2950 Hobson Way
Wright-Patterson AFB OH 45433-7765

8. PERFORMING ORGANIZATION REPORT

AFIT-ENY-MS-17-M-298

9. SPONSORING / MONITORING AGENCY NAME(S) AND ADDRESS(ES)

Dr. Chiping Li, Program Manager
Air Force Office of Scientific Research
875 N. Randolph, Ste. 325
Arlington, VA 22203

10. SPONSOR/MONITOR'S ACRONYM(S)
AFOSR/RTE

11. SPONSOR/MONITOR'S REPORT NUMBER(S)

12. DISTRIBUTION / AVAILABILITY STATEMENT
DISTRIBUTION STATEMENT A: APPROVED FOR PUBLIC RELEASE; DISTRIBUTION UNLIMITED

13. SUPPLEMENTARY NOTES
This work is declared work of the U.S. Government and is not subject to copyright protection in the United States.

14. ABSTRACT

This thesis explores multiple topics, including the relative importance of nondimensional parameters that relate film cooling performance within different temperature regimes and the effects of internal coolant flow and coolant temperature on overall film cooling effectiveness. A Hastelloy model representative of a turbine blade was utilized for IR tests. Near engine temperatures were produced via premixed propane and air combustion in a Well-Stirred Reactor (WSR) with air supplied as the film coolant gas. Near ambient conditions used heated air for freestream flow and carbon dioxide, argon, or air as film coolant gases. It was found that even with multiple matched parameters, the high temperature cases achieved higher overall effectiveness values. The results suggest that the temperature difference between the coolant and freestream is also important, as is the internal mass flow. Test results showed that cooling effectiveness increased with hotter coolant, which is counterintuitive. Numerous improvements to the rig were also implemented.

15. SUBJECT TERMS
Film Cooling

16. SECURITY CLASSIFICATION OF:			**17. LIMITATION OF ABSTRACT**	**18. NUMBER OF PAGES**	**19a. NAME OF RESPONSIBLE PERSON**
a. REPORT	**b. ABSTRACT**	**c. THIS PAGE**			Polanka, Marc D., USAF ADVISOR
U	U	U	UU	168	**19b. TELEPHONE NUMBER** *(include area code)* (937)785-3636, ext 4714(marc.polanka@afit.edu)

Standard Form 298 (Rev. 8-98)
Prescribed by ANSI Std. Z39.18